Optimization of Growth Conditions of $GaAs_{1-x}Bi_x$ Alloys for Laser Applications

by

Vahid Bahrami Yekta
B.Sc., Amirkabir University of Technology, 2007
M.Sc., Amirkabir University of Technology, 2010

A Dissertation Submitted in Partial Fulfillment
of the Requirements for the Degree of

DOCTOR OF PHILOSOPHY

in the Department of Electrical and Computer Engineering

University of Victoria

Supervisory Committee

Optimization of Growth Conditions of $GaAs_{1-x}Bi_x$ Alloys for Laser Applications

by

Vahid Bahrami Yekta
B.Sc., Amirkabir University of Technology, 2007
M.Sc., Amirkabir University of Technology, 2010

Supervisory Committee

Thomas Tiedje, (Electrical and Computer Engineering Department)
Supervisor

Tao Lu, (Electrical and Computer Engineering Department)
Departmental Member

Rodney Herring, (Mechanical Engineering Department)
Outside Member

Abstract

Supervisory Committee
Thomas Tiedje, Electrical and Computer Engineering Department
Supervisor
Tao Lu, Electrical and Computer Engineering Department
Departmental Member
Rodney Herring, Mechanical Engineering Department
Outside Member

GaAsBi is a relatively unexplored alloy with interesting features such as a large bandgap reduction for a given lattice mismatch with GaAs substrates and good photoluminescence which make it promising for long wavelength light detection and emission applications.

In this research, the molecular beam epitaxy (MBE) method was used to grow epi-layers and hetero-structures. A Vertical-external-cavity surface-emitting-laser (VECSEL) was grown as a part of collaboration with Tampere University in Finland. The process of laser growth promoted the writer’s skills in the growth of hetero-structures and led into an investigation of the effect of growth conditions on GaAsBi optical properties with important results. For instance, when the substrate temperature during growth was reduced from 400°C to 300°C and all other growth conditions were fixed, the Bi concentration in the deposited films increased from 1% to 5% and the photoluminescence (PL) intensity decreased by more than a factor of 1000. This is an indication of the importance of growth temperature in GaAsBi crystal quality.

n+/p junctions were grown for the deep level transient spectroscopy (DLTS) experiments in collaboration with Simon Fraser University. The DLTS measurements showed that lowering the GaAsBi growth temperature increases the deep level density by a factor of 10. These deep levels are the source of non-radiative recombination and decrease the PL intensity.

The structural properties of GaAsBi were investigated by high resolution x-ray diffraction and polarized PL and revealed long distance atomic arrangement (Cu-Pt ordering) in GaAsBi. The measurements showed that the ordering is more probable at

high growth temperature. This can be due to the larger mobility of the atoms on the surface at high growth temperatures that allows them to find the ordered low energy sites.

Table of Contents

List of Tables

List of Figures

Acknowledgments

The first and the most I like to thank my supervisor Dr. Thomas Tiedje for providing me with such a great opportunity to research with MBE, XRD and all other high tech equipment and I learnt incredible amount of things about physics and methods of exerting an organized research from him. I was such a privileged graduate student who could take apart the equipment or choose his favorite projects. Dr. Tiedje’s suggestive way of management taught me numerous things about freedom and parallel understanding, something that I was yearning to come across and because of it I travelled kilometers from my home country.

I like to thank my great professors in the UVIC, Dr. Rogerio de Sousa and Dr. Rodney Herring who taught me physics of quantum mechanics and electron diffraction that are inseparable prerequisites for material research.

My mentor and senior students in the Lab Ryan Lewis and Mostafa Masnadi-Shirazi have my gratitude for their help in providing me with invaluable training about using equipment. Especially Ryan who taught me how to use the MBE which only God knows how difficult it was with the language barrier.

At last but not least, I need to thank my parents and my brother for providing me with money and love all the time. Their respect for science and researchers always ensured me that I had chosen the right way of living.

1. Introduction

Semiconductors play all types of roles in our everyday life. From supercomputers to a small wrist watch, all electronic technology depends on semiconductors. The success of the semiconductor industry is a direct result of the access to the elements in five periodic table columns and the ability to manipulate them at the atomic scale by means of ultra-pure methods like molecular beam epitaxy (MBE).

Historically, there has been an enormous effort in the semiconductor field to find new compounds and improve the efficiency of available semiconductors. The semiconductor field can be divided into two main domains based on applications: electronics and optoelectronics. The electronic domain is dominated by silicon technology. Although silicon is currently used for integrated optics devices [1] it does not have a direct bandgap so it is not an efficient light emitter. Top-end microprocessor manufacturers are looking for hybrid III-V-Si chips.

The most important compounds in optical light emitting applications can be argued to be GaAs and InP (and their alloys) at least until the present day. As well as being a direct bandgap semiconductor, GaAs has an electron mobility as high as 8500 cm^2/VS [2] which is important for high speed transistors (HBT) and terahertz devices [3]. GaAs forms alloys with most group III (Al, In) and group V (N, P, Sb) elements. Since bandgap is a function of the alloy composition, alloying GaAs makes it possible to achieve emission over a wide range of wavelengths for different applications. GaAs alloys have the zincblende crystal structure so they can be grown epitaxially on GaAs substrate or even other GaAs alloys while the bandgap is controlled by the composition. This gives us the means to make bandgap-engineered high quality heterostructures that are essential for optoelectronic devices.

Most fiber optic communication systems are based on 1.3 and 1.55 µm wavelengths due to small dispersion and loss in optical fibers at these wavelengths [4]. GaAsP, GaAsSb and InGaAs are the most common GaAs alloys used for long wavelength lasers and detectors [4-5]. They have been well understood and researched over the past 50 years. The demand for more efficient long wavelength light sources has pushed us toward unconventional GaAs alloys formed by incorporating either very light or heavy elements into the lattice. These alloys tend to be more difficult to grow and their band structures are more difficult to understand.

$GaAs_{1-x}N_x$ is an example of an unconventional GaAs alloys. Nitrogen is a small and highly electronegative atom. Incorporation of nitrogen into GaAs was expected to increase its bandgap since GaN has a large bandgap of 3.2 eV but instead it caused a huge bandgap reduction in GaAs. Only 1% of nitrogen incorporation (x=0.01) reduces the GaAs bandgap by 0.2 eV [6]. This bandgap reduction was greater than the reduction by alloying with any other group V element in GaAs at the time. The GaAsN bandgap reduction is accompanied by serious material quality degradation i.e. photoluminescence (PL) intensity and mobility decrease strongly with an increase in nitrogen incorporation. The electron mobility decreases from 8500 cm^2/VS for GaAs to less than 10 cm^2/VS for $GaN_{0.01}As_{0.99}$ [7]. This degradation is due to N 2s states nears the bottom of the CB which scatter electrons and reduce mobility, also N-N next nearest neighbor dimers create localized states, which are strong scatterers. The small atomic size of nitrogen can be compensated with larger Indium atoms in InGaAsN but still incorporation of nitrogen atoms takes its toll and degrades the electronic properties at the required small bandgaps.

One way to improve material quality of the nitrides (GaAsN and InGaAsN) is to use a surfactant during MBE growth. Surfactant is a non-incorporating element on the substrate surface during growth, which modifies the surface structure and energy and helps the other elements to react better with each other and go to the correct sites in the growing lattice. Antimony and Bismuth are two examples of surfactants that are used during GaAs, GaAsN and InGaAsN growth [8,9]. Sb and specially Bi have large atomic size and they tend not to incorporate but rather segregate on the growing surface under standard growth conditions. Materials grown with a surfactant tend to have better PL and smoother surfaces and interfaces.

When GaAs is grown at a low substrate temperature the Bi surfactant atoms incorporated into the growing film and resulted in another unconventional alloy, GaAsBi.

Small incorporation of Bi into GaAs causes a huge bandgap reduction. GaBi is predicted to be a metal so GaAs bandgap reduction with Bi incorporation is more intuitive than the bandgap reduction associated with N.

GaAsBi and GAsN are two highly mismatched GaAs alloys. Bi and N interact with GaAs band structure in a similar way. It was found in GaAsN that the large size difference between nitrogen covalent radius (~70 pm) with GaAs host atoms (~120 pm) causes a strong perturbation in the host band structure. The nitrogen valence 2s orbital is close in energy to the GaAs conduction band minimum (CBM). The interaction between the 2s orbital and the CBM results in a downward motion of the GaAs conduction band and a big reduction of its bandgap. A similar resonant interaction happens in GaAsBi. The 6p valence orbital of Bi resides close to valence band maximum (VBM) of GaAs. The Bi orbital pushes the VBM upward and reduces the bandgap of GaAs when Bi is incorporated [10,11]. The energy of the spin-orbit split off (SO) band does not change much with Bi incorporation so the SO separation energy increases [12]. The increase in the separation of the SO band results from the very large spin-orbit interaction of electrons on Bi atoms. The strong SO interaction has significance for spintronic applications. Figure 1.1 shows a schematic of the GaAsN and GaAsBi band structures with localized Bi and N cluster states.

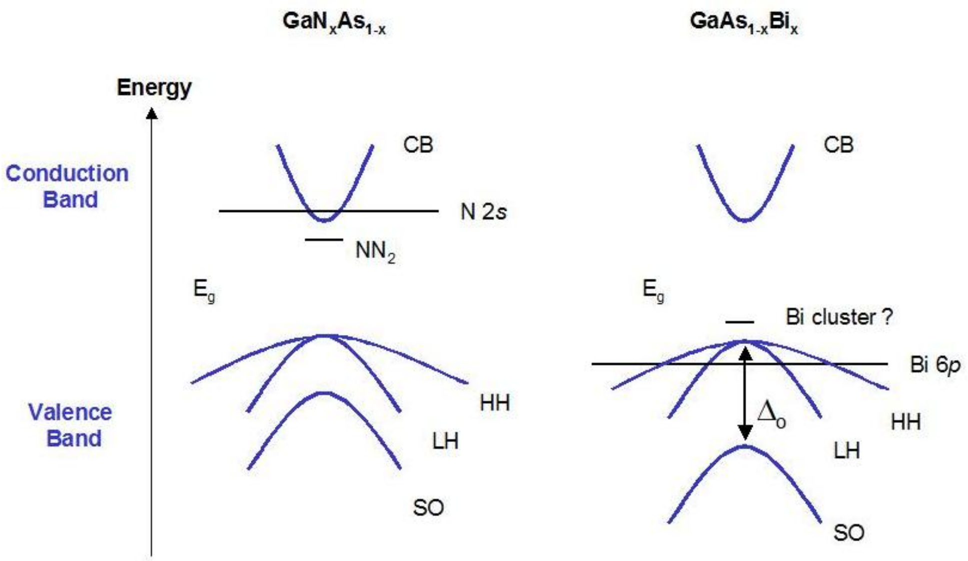

Figure 1-1: GaAs band structure affected by N 2s and Bi 6p orbitals. CB: conduction band, HH: heavy hole, LH: light hole, SO: split off band, Δ0: spin-orbit separation energy and NN2: N dimer cluster state. Figure was originally published in [16].

Some Bi atoms randomly form next nearest neighbors dimers and trimers during growth which according to theory can appear as localized acceptor states close to the VBM [13,14]. Acceptor levels associated with Bi clusters are believed to be responsible for the unwanted p-doping of nominally un-doped GaAsBi. The p-doping increases with Bi concentration and makes the un-doped GaAsBi very conductive at high Bi concentration [15].

GaAsN proved that there is still a lot that can be done on long wavelength emission materials. GaAsBi can be even a stronger opponent for other long wavelength alloys grown on GaAs substrates. Figure 1-2 compares the bandgap of four ternary GaAs alloys as a function of their lattice mismatch with GaAs substrates. GaAsBi surpasses all other GaAs alloys in making smaller bandgap material with low strain. In addition thick pseudomorphic strained GaAsBi layers can be grown because of its comparatively low growth temperature and the Bi surfactant effect that was discussed earlier. Low growth temperature is superior for growing thick layers with smaller bandgap but it also has serious drawbacks such as non-radiative defects. The density of these defects and their dependence on growth temperature is the main topic of discussion in chapters 4 and 5.

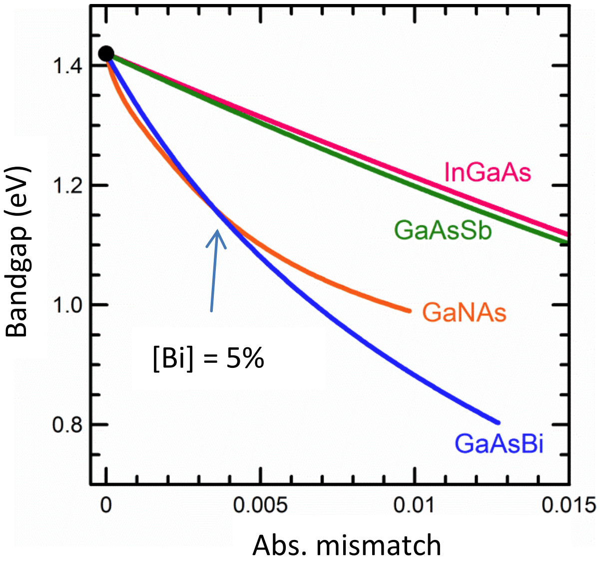

Figure 1-2: The bandgap of ternary GaAs alloys as a function of their lattice mismatch with GaAs substrates. GaAsBi surpasses all the alloys in bandgap reduction after 5% Bi incorporation. Data sources are as follows: GaNAs [17], GaAsBi [18], InGaAs [19] and GaAsSb [20]. The figure was originally printed by R. Lewis et al. [21].

The equipment and experimental setups that are used during the growth of GaAsBi (in-situ apparatus) and the equipment used to characterize the grown layer and devices (ex-situ apparatus) are explained in chapter 2. Chapter 3 is dedicated to the main goal of all the research that I did, “growing a GaAsBi laser”. The failure in the laser project provoked me to investigate non-radiative defects in GaAsBi (Chapter 4 and 5). One side project, Cu-Pt ordering in GaAsBi, was done during the PhD period. It is explained respectively in chapters 6. A short summary concludes the PhD thesis.

2. Experimental methods

2.1. Crystal growth by molecular beam epitaxy

Molecular beam epitaxy (MBE) is a method for growing high quality crystalline semiconductor layers for optical devices or research purposes. High quality means very pure with precise control on thicknesses and compositions and a low concentration of structural defects.

Figure 2.1 shows a simple schematic of the University of Victoria MBE system. It is a VG-V80H MBE system which consists of three distinct sections: growth, preparation chambers and load lock that are separated from each other by gate valves. All these chambers are pumped 24/7 by ultra-high vacuum (UHV) pumps. The gate valves in between the chambers are only opened occasionally to transfer a substrate to another chamber. Epitaxial growth is only possible if the epi layer is grown on an existing single crystal substrate. The substrate is GaAs or InP single side polished, (001)-oriented 2”, wafers with a thickness of 350 µm and ±0.5º maximum axial tilt. The substrates are clamped on molybdenum holders and then loaded into the MBE load lock section. As a first step in preparation for the epitaxial growth, the substrate is heated to 460ºC in the MBE preparation chamber and all the moisture is removed from the holder/substrate. Then the substrate is moved inside vacuum to the growth chamber. The substrate has an oxide layer on its surface due to the exposure to air prior to loading. The surface oxide is removed before growth by heating the substrate to 610ºC in the growth chamber for 10 minutes while the surface is exposed to an arsenic flux. The oxide removal process results in 40 nm deep pits on the surface caused by explosive evaporation of Ga_2O [22]. The substrate surface can be smoothed again by growing a 0.5 µm GaAs buffer layer at 580ºC.

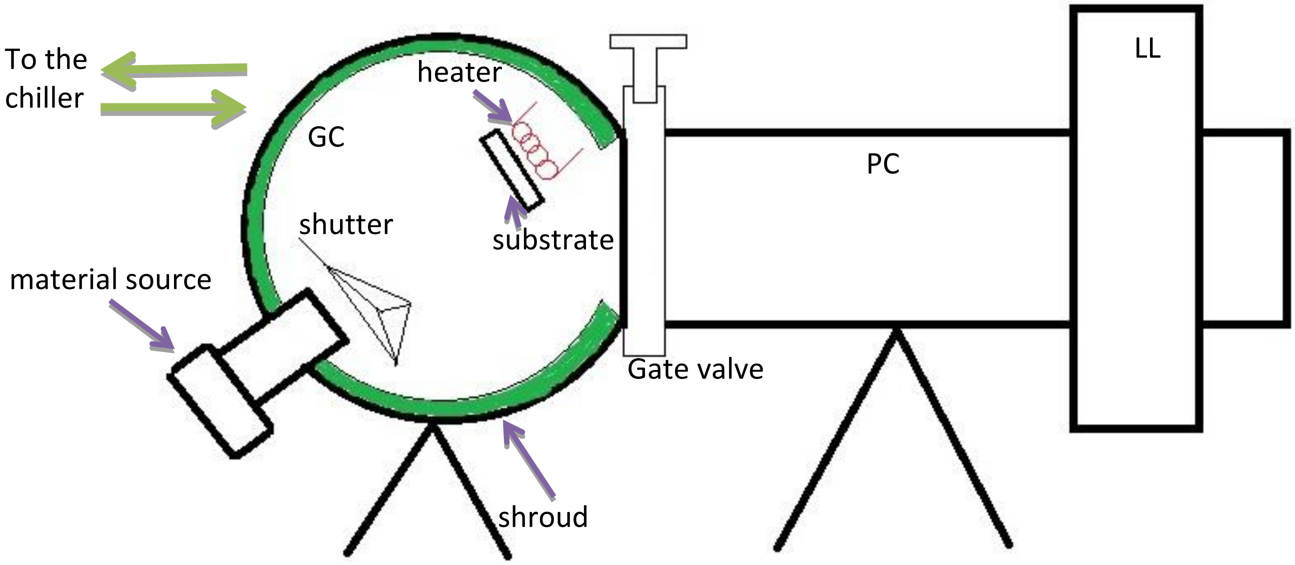

Figure 2-1: Schematic of the UVic MBE system. GC: growth chamber, PC: preparation chamber, LL: load lock.

The UVic MBE is equipped with seven material sources. Ga, In, Al, Bi and Si sources are conventional Knudsen cells with shutters in front of their output. The arsenic cell is a valved two zone thermal cracker source. An external gas injection CBr_4 system is used as the p-doping source which is described later in chapter 7. The material sources are attached to the growth chamber spherical body and the substrate is located at the focal point of the cells. The MBE growth chamber base pressure is 10^{-10} Torr. The pressure may rise to 10^{-7}-10^{-8} Torr during growth but still it is so low that the mean free path of atoms is some kilometers. With such a large mean free path the flux of the evaporated material from the cells only depends on the cell temperature and impurities such as oxygen and water are unlikely to incorporate due to their low concentration and low sticking coefficient.

The material sources are evaporated by heaters inside the cells while their temperatures are read by thermocouple and controlled within ±1 degree accuracy. The beam of evaporated molecules (atoms) goes to the substrate surface. When the substrate is heated to the required growth temperature the molecular beams react on the substrate surface with each other and the epilayer film grows with the same crystal structure as the substrate. The growth rate is found by dividing the grown film thickness found by x-ray diffraction, by the growth time. The growth temperature is lowered to 300-400ºC to grow the bismide layer. The samples are rotated at a rate of 0.5 Hz during growth to ensure that the flux of all the sources is as uniform as possible on different parts of the substrate. The epilayer growth is discussed in more details in chapter 3 where the growth parameters of GaAsBi are completely described.

Heating the cells and substrate during growth can make the chamber very hot and increase the background pressure by outgassing from the walls therefore the inside of the vacuum chamber needs to be cooled. In addition a cold surface inside the vacuum chamber helps with pumping by cryo condensation and cryo adsorption. MBEs conventionally use an LN2 circulation to cool the shroud but the UVic MBE shroud is attached to a closed cycle chiller which is cooled with a dimethyl polysiloxane heat transfer fluid. A closed cycle chiller cools the fluid to -80ºC and pumps it into the shroud. The chiller cooling method has decreased the cost of our MBE growth process while the quality of the grown material is the same as with the LN2 method [23].

2.2. In situ monitoring setups

Research MBE systems typically have different tools installed to monitor the sample growth in-situ. The UVIC III-V MBE has one of the most complete set of in-situ measuring and monitoring tools.

- Measurement tools: residual gas analyzer (RGA) and retractable ion gauge.

- Monitoring setups: reflection high energy electron diffraction (RHEED) setup, diffuse reflection spectroscopy (DRS) for contactless optical temperature measurements and elastic light scattering (LS) for monitoring surface morphology.

2.2.1. Residual gas analyzer (RGA)

The RGA is a tool to measure the pressure of elements in a chamber as a function of their molecular mass. Our system has a Stanford Research Systems RGA that can analyze gases with molecular masses up to 200 u. A filament and Faraday cage turn the atoms/molecules into ions and they are accelerated inside a quadrupole mass filter with dc+ac magnetic field which allows only a certain mass to charge ratio to pass and be measured by the ion detector. The RGA is an essential tool to find leaks in the MBE chamber. The presence of masses 32 u (oxygen) and 40 u (Argon) is an indication of a leak. Helium is rare in the air so it can be used to pinpoint the location of the leak. Different parts of the chamber are exposed to helium flow until a rise in helium pressure is seen on the RGA scan which indicates the leak location.

2.2.2. Ion gauge

The ion gauge measures the pressure of all the gases combined in UHV and HV chambers. An electric field between a hot filament and a grid surrounding it accelerate electrons in all directions which ionize the gas molecules. Then the ions are attracted into a collector and cause a current that is proportional to the pressure and it is calibrated for nitrogen at 300K.

Our system has several ion gauges to measure pressure in the growth and preparation chambers. It also has a retractable ion gauge that can be placed in the sample position to measure beam equivalent pressure (BEP) of the material sources at the substrate location. The BEP has units of pressure (Torr or mbar). The measured BEPs of two material sources x and y can be changed into flux ratio by the following relation [24]:

$$\frac{F_x}{F_y} = \frac{BEP_x}{BEP_y}\frac{\eta_y}{\eta_x}\sqrt{\frac{T_x M_y}{T_y M_x}} \tag{2.1}$$

Where F_x and BEP_x are the flux (number of molecules/area/time) and BEP of source x. η_x, T_x and M_x are the relative ionization efficiency, absolute temperature and molecular mass of x respectively. One problem is the geometry dependence of this formula. The BEP measurement depends on the position of the ion gauge, with the respect to the plane of gas molecules exiting the effusion cell.

The most important flux ratio for this thesis is the As:Ga=1 atomic ratio which is determined experimentally by light scattering and RHEED methods. When the arsenic flux is just on the border of metallic gallium droplets formation, the arsenic atom density on the surface is equal to the gallium atom density and the valve setting is called 1:1 ratio. A complete explanation about finding the 1:1 ratio in our samples is provided in the light scattering setup section.

2.2.3. Diffuse reflection spectroscopy (DRS) setup

The substrate temperature during growth is an important parameter which can have a strong effect on the composition and defect density. An accurate measurement of growth temperature is critical for growing semiconductor alloys with reproducible properties. As in figure 2-1 the substrate/holder is heated radiatively by a heater placed inside the sample manipulator behind the substrate. The heater voltage is controlled by the grower and used to set the temperature. As a rule of thumb each 10V increase in heater voltage gives a rise of 100ºC to the substrate temperature. This approximation can be off by 30ºC depending on the cell temperatures which also heat the substrate radiatively, the substrate contact with the Pyrolytic Boron Nitride (PBN) holder and the shape of the substrate. A suspended thermocouple in between the heater and the back of the substrate also reads the temperature but the error is huge as there is only radiative contact between the thermocouple and the wafer. Making a physical contact between the substrate and a thermocouple is not possible due to difficulties with sample loading. The growth temperatures of GaAs alloys are often too low for a pyrometer and the sample is transparent in the IR. The problem with the substrate temperature measurements was solved by S. Johnson al. [25]. To have a good temperature reading an optical setup is used that can infer the substrate surface temperature from the diffuse reflected light which monitors the substrate bandgap continuously during growth.

The filament of a halogen lamp is imaged on the substrate through one of the growth chamber windows. The incident light has a 25º angle with the substrate normal. The long wavelength lamp light is transmitted through the wafer and scattered from the rough back surface of the wafer or the rough PBN plate behind the wafer. The scattered light coming out of the wafer has passed through the whole substrate thickness twice and its intensity is affected by the wavelength dependent absorption of the GaAs or InP substrate. We assume the epilayer thickness is negligible compared to the substrate. The diffuse scattered light from the normal direction of the substrate is collected with a lens and focussed into a large core (550 µm diameter) optical fiber cable and transferred to a spectrometer. The spectrometer disperses the fiber output on to an array of detectors that is connected to a computer. The absorption spectrum of the substrate (GaAs or InP) is inferred from the diffuse scattered light spectrum by a LabVIEW program. The heater and cell radiations introduce some background light that can be omitted by subtracting the lamp “on” and lamp “off” spectra. The LabVIEW program displays the absorption spectrum at time intervals assigned by the user. It also fits a simulation to the absorption edge of the spectrum and infers the substrate temperature from the wavelength in the absorption spectrum corresponding to the bandgap. The DRS method gives us the ability to measure the substrate temperature online with a sensitivity of ±2º. Further information can be found in the paper by Johnson et al. [25].

2.2.4. Reflection high energy electron diffraction (RHEED)

RHEED was one of the first in-situ methods used to understand surface evolution during crystal growth. Our RHEED setup has a high energy 15 keV electron gun. The emitted electrons hit the sample surface with a grazing angle (<3º) and are diffracted from the surface. The diffracted electrons are revealed on a phosphorous screen installed on an MBE window at the specular reflection. The normal component of the incident beam is small so it only penetrates one or two surface atomic monolayers. The resulting pattern of scattered electrons is a surface diffraction pattern.

The possible reflections in the diffraction pattern are the ones for which the incident and diffracted beams are related with a reciprocal lattice vector $\vec{G}$:

$$\overrightarrow{k_D} - \overrightarrow{k_I} = \vec{G} \tag{2.2}$$

Where $|\overrightarrow{k_I}|$ and $|\overrightarrow{k_D}|$are incident and diffracted wave vectors. If the diffraction is elastic $|\overrightarrow{k_I}| = |\overrightarrow{k_D}|$, the allowed diffraction vector maps out the Ewald sphere with the radius of the incident vector magnitude. If the relativistic correction is neglected then

$\left|\overrightarrow{k_I}\right| = \frac{1}{\hbar}\sqrt{2m_0E}$. This gives a magnitude of 629 nm^{-1} that is 60× larger than the GaAs reciprocal lattice unit. The large radius of the Ewald sphere with the small reflection angle facilitates the interpretation of the RHEED patterns. The reciprocal lattice of the surface is a set of two-dimensional rods along the z-direction perpendicular to the surface. The Ewald sphere is coincident with several rods in the 2D reciprocal lattice (figure 2-2). Each rod produces a reflection in the diffraction pattern at the intersection with the Ewald sphere where the diffraction condition is met. The diffraction points appear on Laue circles with the radius of L_n centered at H which is the projection of the beam parallel to the sample surface [26].

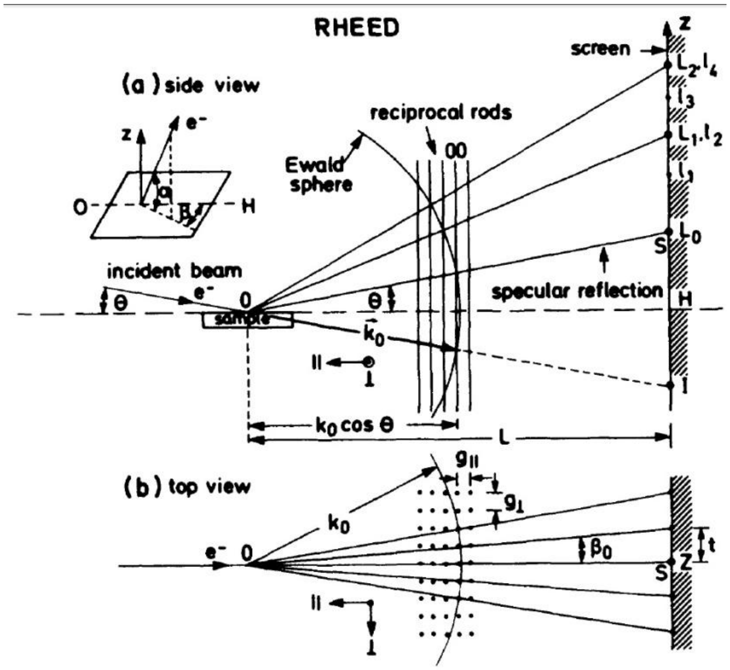

Figure 2-2: Ewald sphere intersects the 2-D reciprocal lattice of the surface. The figure was copied from [26].

A perfectly flat surface and a perfectly collimated electron beam give a spotty diffraction pattern but in a real growing crystal both the reciprocal rods and the Ewald sphere have finite thicknesses which results in elongated or streaky diffraction patterns. There is an energy variation among the electrons that causes the Ewald sphere thickness not to be zero. Also the surface consists of some growing islands and it goes from nucleating points to the formation of a successful monolayer which causes the reciprocal rods to broaden [27].

The crystal structure of the surface can be different from the bulk. The surface atoms reposition themselves in order to minimize the energy associated with dangling bonds and create a so-called "surface reconstruction". The surface periodicity can be different from the bulk. A wafer has two orthogonal in-plane directions of $[0\bar{1}1]$ and $[011]$. The periodicity of the bulk crystal in these two directions can be described as 1×1. If no surface reconstruction happens the surface structure is the same as the bulk. A reconstruction of 2×1 shows that the periodicity of the atoms on the surface is twice that of the bulk in the $[0\bar{1}1]$ direction.

Figure 2-3 shows an example of a surface reconstruction in RHEED. The best quality GaAs is grown at 580ºC with As_2:Ga(BEP)=6 which we will call standard growth conditions. The surface reconstruction for the standard GaAs growth is 2×4. This reconstruction is not completely understood at the atomic level and can be explained by three different atomic arrangements (figure 2-4). The RHEED pattern is sensitive to the V:III ratio and growth temperature. It helps to understand the surface chemistry at different growth conditions. Certain surface reconstructions are associated with bulk ordering and enhancement of the material quality. This will be explained thoroughly in chapter 6 when Cu-Pt ordering in GaAsBi is discussed.

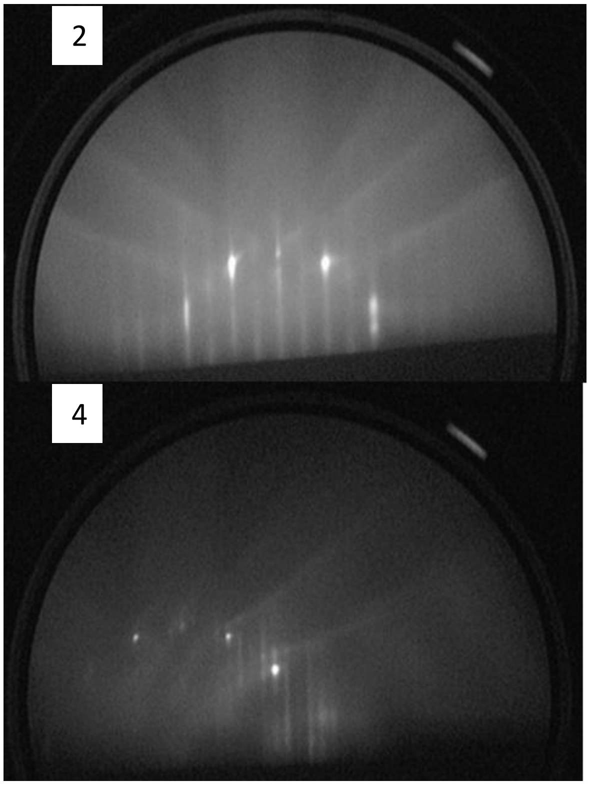

Figure 2-3: GaAs growth at standard conditions with 2×4 surface reconstruction.

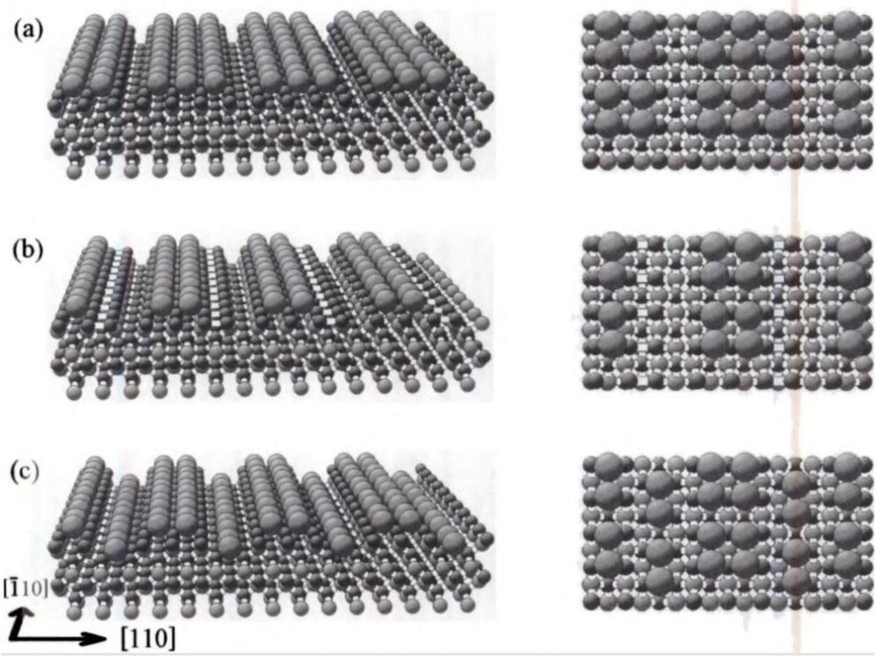

Figure 2-4: Suggested Arsenic dimer arrangements on the surface used to explain the 2×4 surface reconstruction. (a) a three dimer model (b) a two dimer model with second layer Ga in the missing dimer rows and (c) a two dimer model with a third layer arsenic dimer row. The image was copied from [26].

RHEED is highly sensitive to the surface structure therefore it can be used to monitor some of the most important processes of the crystal growth. An amorphous oxide layer on the surface causes a uniform haze on the RHEED screen. When the sample is heated up to remove oxide, oxygen atoms evaporate from the surface and leave pits and craters on the surface. The bulk geometry of the pits turns the RHEED pattern into bright spots that is a signature of oxide removal. When a buffer layer is grown and the pits are smoothed, the RHEED pattern turns into streaky lines.

The RHEED diffraction intensity oscillates during growth as each atomic monolayer is completed and joins the bulk crystal. The period of the oscillation is related to the growth rate of a single monolayer [26]. A camera with software to detect the light intensity can easily find the oscillation period and by inference the growth rate.

2.2.5. Light scattering (LS)

The surface morphology evolution is monitored during growth by elastic light scattering. A 488 nm Ar-ion laser beam is chopped at 2 kHz and focused on the sample surface with a spot size of ~5 mm (figure 2-5). Most of the incident light is reflected specularly and allowed to leave the chamber through a window at the specular angle. This reduces multiple scattering from the chamber walls that can make it impossible to detect the small scattering from the substrate surface. The small portion of the incident light that scatters from the sample surface is collected with a lens placed at a cell port. The collected light is spatially filtered with a diaphragm and imaged on a photo multiplier (PMT) whose output is measured by a lock-in amplifier. The lock-in signal is displayed on a computer by a LabVIEW program.

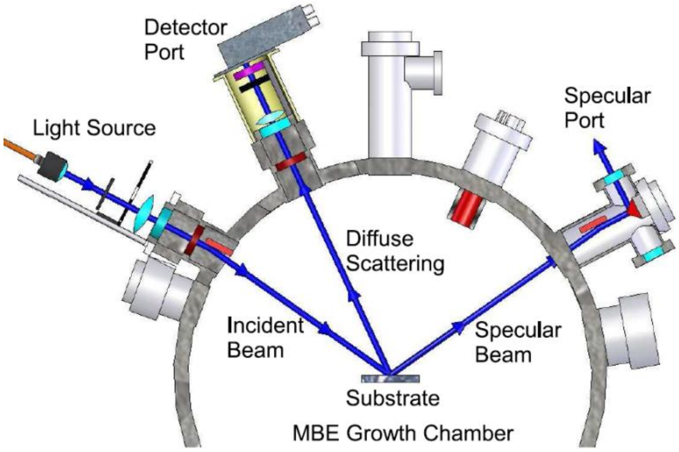

Figure 2-5: The light scattering setup of the UVic MBE. The picture was originally published in [28].

The scattered light intensity is directly proportional to the power spectrum of the sample topography. The spatial frequency of the scattering centres on the sample surface that are detected with the light scattering depends on the incident light frequency (λ) and the incident and scattering angles (θ_i, θ_s) [28]:

$$\vec{q} = \frac{2\pi}{\lambda}(sin\theta_i\hat{x} - sin\theta_s\hat{y}) \tag{2.3}$$

In our setup the incident angle is 25º or 55º from the sample normal depending on the holder rotation angle and the PMT is located at 73º so the spatial frequency is calculated to be 13.5 to 16.2 μm^{-1}, which are characteristic lengths of ($2\pi/q$) = 465 and 387 nm [28].

LS together with RHEED are used to monitor the oxide removal process. When the sample is hot enough (more than 590ºC), oxide evaporates which roughens the surface and causes the LS signal to increase. The sample is kept at more than 600ºC for 10 minutes after the LS stops increasing to make sure all the oxygen atoms are removed.

LS together with RHEED are used to determine As:Ga 1:1 flux ratio or stoichiometric condition. The As_2 pressure is gradually reduced by a micrometer controlled valve on the As_2 cracker cell (VEECO model number 500v-As Mark IV) to the point where the scattered light signal just begins to increase. If surface roughening occurs during this process the surface is smoothed by increasing the As_2 flux and the procedure repeated. The value of the valve setting just before the surface begins to roughen is taken as the stoichiometric V:III ratio on the surface or 1:1 ratio. The stoichiometric condition is measured independently for each growth run at its growth temperature and growth rate. The ratio is growth temperature dependent because the arsenic sticking coefficient is smaller at higher temperatures. The As_2:Ga BEP ratio was found by ion gauge flux measurement to be 2.4 and 3.3 for growth temperatures of 300 and 350°C respectively.

2.3. Ex-situ characterization

After growing the sample in the MBE with all the in-situ monitoring, the sample optical, structural and electrical properties can be investigated with ex-situ measurement techniques.

- Structural characterization: X-ray diffraction machine

- Optical characterization: Photoluminescence (PL), Reflectivity setups

- Electrical characterization: Hall-Van der Pauw setup and electron beam evaporator

- Low temperature measurement: Cryostat setup

2.3.1. High resolution x-ray diffraction

A crystal is a collection of atoms organized in a repeated 3D pattern. Diffraction of x-ray or any other wave with wavelength smaller than the crystal atomic distance from a set of atomic crystal planes gives the Fourier transform of the atom distribution in the direction normal to that set of planes. The reciprocal lattice is the collection of Fourier transform points for all crystal directions.

X-ray diffraction from a certain set of planes with Miller indices (*h*,*k*,*l*) follows the diffraction condition (equation 2.2) and elastic scattering $|\overrightarrow{k_I}| = |\overrightarrow{k_D}|$.

From geometry, the absolute value of the difference vector ($|\vec{G}| = 2\pi/d_{hkl}$) is related to the beam's wavelength and $sin(\theta)$, where θ is the angle between the incident and diffracted beams. This results in the well-known Bragg's law for diffraction in crystals:

$$n\lambda = 2d_{hkl}\sin(\theta) \tag{2.4}$$

Figure 2.6 shows an x-ray beam and its diffraction from a crystal. ω and 2θ are the x-ray source and detector angles with the sample surface respectively. For crystal planes parallel to the sample surface ω is equal to θ. The XRD scan that is used to determine epilayer thickness and composition is called a ω-2θ scan. In this type of scan the X-ray diffraction machine changes ω and 2θ in a range around the predicted Bragg condition and a peak happens when ω and 2θ satisfy the Bragg condition for a certain set of crystal planes. A pseudomorphic strained epilayer has the same in-plane lattice constant as the substrate, but a larger (or smaller) out-of-plane lattice constant, therefore the out-of-plane component of its diffraction angle in reciprocal space is smaller (or larger) than the substrate. An ω-2θ scan measures both the substrate and epilayer out-of-plane diffraction peaks and gives us the relative intensity and angle of the epilayer diffraction. These parameters can also be calculated from dynamic diffraction theory [29] and the thickness and composition can be inferred from the angle and shape of the diffraction peak corresponding to the epilayer.

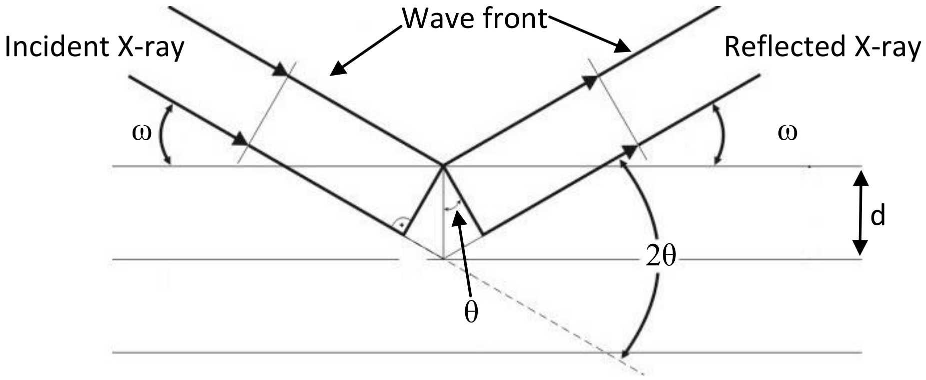

Figure 2-6: Diffraction of X-ray from atomic planes, assumed to be parallel to the sample surface. ω is normally the angle between the incident beam and the sample surface.

The UVIC lab is equipped with a Bruker D8 Discover high resolution x-ray diffraction machine. It generates x-rays by accelerating electrons at 40 kV potential toward a copper target in a vacuum tube. The x-ray goes through collimating and monochromating optics and a $k_{\alpha l}$ x-ray beam at 0.154051 nm wavelength hits the sample. The sample is loaded on a goniometer with a resolution of 0.0001° that can change any of the rotational and/or translational axes independently. The diffracted beam is detected either through a slit or a 3-bounce analyzer crystal with a best resolution of 16 arcsec.

GaAsBi has a larger lattice constant than GaAs so its ω-2θ scan has an XRD peak at smaller angles than the GaAs substrate. The dynamic diffraction equations for GaAsBi/GaAs are solved with commercial software (LEPTOS) in order to fit a simulation to the measurement. Pseudomorphic growth was assumed for the GaAsBi epilayers and the GaBi 6.33 A° lattice constant calculated theoretically and Poisson ratio 0.31 were entered into the software [30]. An x-ray calibration factor of 0.33 Bi%/100 arcsec was obtained from the x-ray simulations.

HR-XRD can also be used to determine relaxation in the epilayer. Figure 2.7 compares a strained unit cell to a relaxed one. The in-plane lattice constant of the relaxed unit cell is not equal to the substrate lattice constant so the diffraction of the relaxed film does not match in-plane or out-of-plane substrate diffraction. This can be observed experimentally if an area of the reciprocal space around an asymmetric reflection such as 224 is mapped (a RSM) by x-ray diffraction.

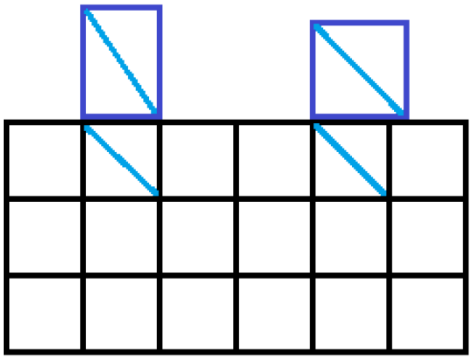

Figure 2-7: Illustration of fully strained (left) and fully relaxed (right) epilayer unit cells on the substrate.

2.3.2. Photoluminescence (PL)

Luminescence occurs when excited electrons and holes in a semiconductor recombine and emit photons with the bandgap energy. PL setup is an important tool to investigate electronic defects in semiconductors. Figure 2.8 shows a schematic of a PL setup. An excitation laser with photon energy larger than the sample bandgap generates electrons and holes. Our setup uses a 523 nm frequency-doubled diode-pumped YLF laser with 20 ns long pulses at an intensity of 10^4 W/cm^2 and 2 kHz repetition rate as the excitation source. The electron-hole pairs recombine after a certain lifetime and emit photons with a peak at the energy of the semiconductor bandgap. The emission spectrum of the sample is collected by an optical setup. The optical setup consists of two lenses and one optical filter. The sample is at the focal point of the collecting lens that collects the PL emission and collimates it toward the focusing lens. The focusing lens has the same f-number (explained below) as the spectrometer and it focuses light on a large area optical fiber that transfers the PL emission to a spectrometer. An optical filter filters the laser stray light and emission harmonics. The spectrometer disperses the PL on to a liquid nitrogen-cooled InGaAs array detector. The detected light spectrum is displayed on a computer screen. The room background light is also collected in a separate measurement with the exciting laser off and subtracted from the sample emission spectrum by the computer software.

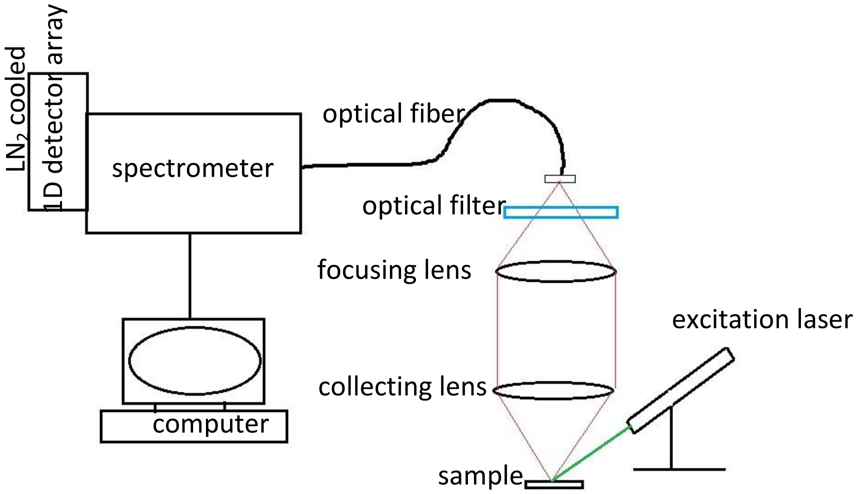

Figure 2-8: PL setup schematic.

The f-number is calculated from the focal length of a lens divided to its diameter. It is a gauge of the light collecting power of an optical component. The flux of the light that goes through an optical component is inversely proportional to f-number squared so smaller f-number means more light flux but worse aberration. Since the spectrometer f-number is fixed, it dictates the f-number of all other components in an optical setup. The numerical aperture is another measure of light collection: N.A. = 1/(2×f-number). The N.A. of the optical fiber is decided by the spectrometer f-number.

The other important consideration in a PL setup or any optical setup with a spectrometer is filtering the harmonics. A spectrometer grating disperses different wavelengths into different spatial positions based on the Bragg's law: $\mathrm{n}\lambda = 2\mathrm{d}\sin(\theta)$. All the $\mathrm{n}\lambda$ wavelengths can come out of the spectrometer with the same grating angle. A long pass optical filter is used to stop the harmonics of the stray lights from interfering with the sample emission. In our PL setup an 830nm cut off filter allows us to look at a harmonic free wavelength range from 830 to 1660nm.

2.3.3. Reflectivity

Our goal in this research was to grow a vertical-external-cavity surface-emitting laser (VECSEL) structure. The cavity of this type of laser consists of a distributed Bragg reflector (DBR) on one side and a concave mirror as the external reflector. The structure of the laser is explained explicitly in chapter 3. The distributed Bragg reflector mirror needs to have almost 100% reflectance in the lasing wavelength range. To test the DBR, its reflectance spectrum is measured by a reflectivity setup.

Figure 2.9 illustrates a reflectivity setup with both incident and reflected light normal to the sample surface. Two lenses focus a halogen lamp light into the monochromater slit. The lenses are chosen and placed with the f-number considerations as explained for the PL measurement. The single wavelength output beam of the monochromator is filtered, chopped and then focused by another lens on the sample. The reflected beam from the sample is directed by a beam splitter toward the detector that has a 90° angle with the sample. The detector is an extended bandgap InGaAs detector and its output is measured by a lockin amplifier. The Lock-in amplifier is connected to a computer that plots the spectrum with a LabView program.

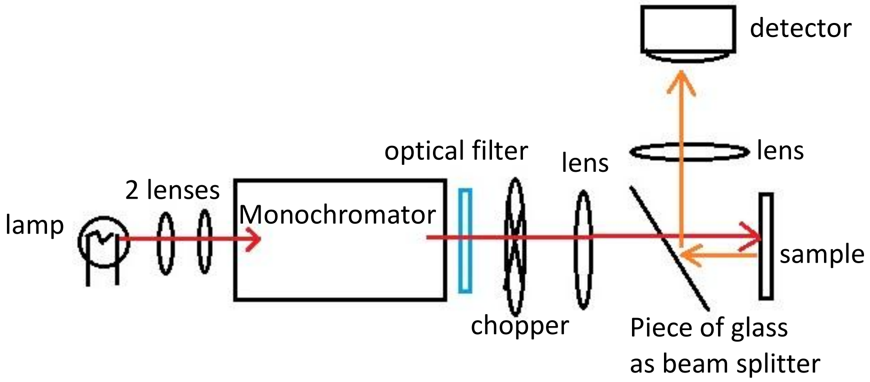

Figure 2-9: Reflectivity setup schematic.

The monochromater grating and other optical components have wavelength dependencies which affect the spectral shape. The transfer function of the whole optical setup must be found, then the final reflectance spectrum of the sample is obtained by dividing the measured spectrum by the transfer function.

The transfer function of the setup is determined using the reflectance of a gold mirror as a reference. The gold mirror reflectance is constant and 97% in the wavelength range of interest for our experiments (900-1500nm) [31]. The gold mirror must be placed exactly in the sample spot to have a completely calibrated spectrum.

2.3.4. Hall-van der Pauw setup and electron beam evaporator

Deep level transient spectroscopy (DLTS) was used to determine the defect density in GaAsBi grown with our MBE system. DLTS is carried out with either Schottky or pn junction samples. The carrier concentration has to be adjusted to certain values for the pn junction to be suitable for DLTS experiment. Carrier concentrations were measured by the van der Pauw method. This method is especially effective for epitaxial thin films. To perform van der Pauw measurements the sample had to be prepared properly.

A van der Pauw sample is cut in a 0.7×0.7 cm square and has 4 contacts at the 4 corners. The contacts should be small compare to the sample size and they should be Ohmic. The Ohmic contacts for pGaAs and nGaAs are Ti/Pt/Au and AuGe/Ni/Au respectively [32]. The contacts are deposited on the sample by an electron-beam-evaporator system. The electron-beam-evaporator has a filament that generates a beam of electrons at 6 kV potential and 600 mA current. The electron beam is directed by magnets on to a carbon or tungsten crucible full of the desired metal for the contact and evaporates the metal. A mask covers the sample and only allows the evaporated metal to be deposited at the 4 corners of the sample and the thickness of the deposition is monitored by a quartz gold crystal thickness monitor.

After contact evaporation, the sample is glued on to a holder that is either a glass slide or a copper plate. A piece of cigarette paper isolates the copper plate electrically from the sample. A 4 pin connector is glued to the holder and then silver epoxy is applied to connect 4 pieces of very thin wires in between the metal contacts on the sample and the pins of the connector. The final product of this preparation is shown in figure 2.10.

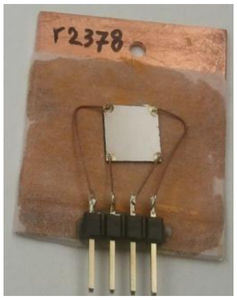

Figure 2-10: a van der Pauw sample.

A current source drives a certain current between two corners on one side of the square sample and a voltmeter measures the voltage on the other corners. The current source and voltmeter can be connected to the sample in four different configurations which result in four resistances,R_{12}, R_{34}, R_{14}, R_{23}, measured in between the sample four corners (figure 2.11). The sheet resistance (R_s) of the sample is calculated from van der Pauw's formulas [33]:

$$R_V = \frac{R_{12}+R_{34}}{2}, R_H = \frac{R_{14}+R_{23}}{2} \tag{2.5}$$

$$e^{-\pi R_V/R_s} + e^{-\pi R_H/R_s} = 1 \tag{2.6}$$

Then the van der Pauw sample is fixed in between two permanent magnets and the current source puts a diagonal current in the sample and the voltage on the other diagonal is measured (figure 2.11). This voltage is referred to as the Hall voltage and it is the result of the equilibrium between magnetic and electric forces. The magnetic force can be applied in two directions (+B,-B) so eight Hall voltages are measured. The sum of all Hall voltages is used to calculate the carrier concentration of the sample [32]:

$$n_s = 8 \times \frac{10^{-8}\mathrm{IB}}{\mathrm{q}|\sum V_i|}\ cm^{-2} \tag{2.7}$$

$$n = n_s/d \quad cm^{-3} \tag{2.8}$$

Where q and *d* are electron charge and sample thickness (*cm*) respectively.

The carriers' mobility can easily be found from the sheet resistance and carrier concentration:

$$\mu = \frac{1}{\mathrm{q}n_s R_s} \quad (cm^2V^{-1}S^{-1}) \tag{2.9}$$

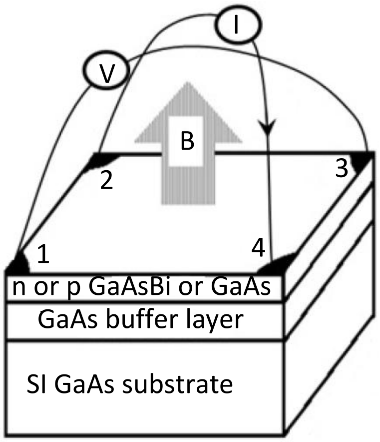

Figure 2-11: van der Pauw configuration for Hall measurements.

2.3.5. Cryostat for low temperature measurement

Low temperature measurements have a special place in semiconductor defect investigations. When thermal excitation is diminished in a lattice, the carriers concentrate at the band edges and the defect states can participate further in optical and electrical transitions that reveal important information about their energy and density. A cryostat is a device to cool samples to less than 10K for optical and electrical measurements. Figure 2.12 shows a schematic diagram of a helium cooled cryostat. A cryopump connected to a helium compressor cools a copper pillar. The sample holder is screwed to the end of the pillar and it is covered with a cap. The cap has 4 quartz windows for optical measurements and a pumping line to evacuate the space around the sample. There is also a heater inside the pillar. A sensor reads the pillar temperature and a controller sets the temperature by using the heater in on/off mode. A temperature range of 8-300 K with ±2° accuracy is accessible with this cryostat.

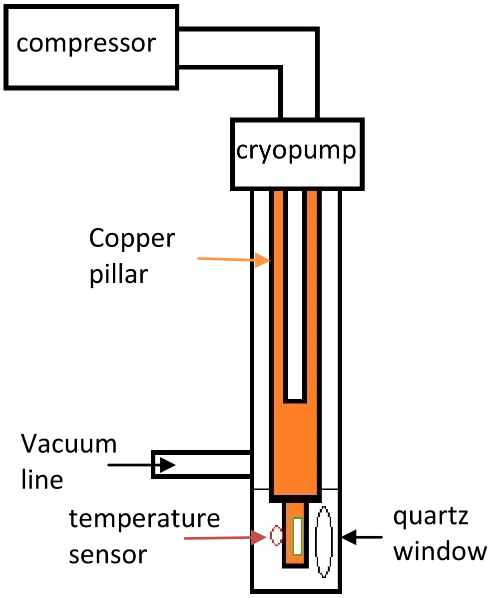

Figure 2-12: A closed cycle He cryostat system for low temperature optical measurements.

3. Growth of VECSEL structure

3.1. Introduction and Contributions

This chapter begins with a description of GaAsBi alloy growth conditions and then continues with the process of growing a laser sample. At the end, the x-ray and PL of the structure are explained and the lasing experiment and results are discussed.

All the samples in chapter 3 and 4 were grown and characterized by the author. More than 150 samples were grown for calibrations and understanding the growth parameters. The design of the laser structure was done at the University of Tampere in Finland by Mircea Guina and Ville Markus Korpijarvi. The laser test was done by Emmi Kantola at the University of Tampere.

3.2. GaAsBi growth

Before a long wavelength $GaAs_{1-x}Bi_x$ laser structure is fabricated the growth of $GaAs_{1-x}Bi_x$ material must be understood. To incorporate Bi into GaAs, the growth conditions have to be severely deviated from standard GaAs growth parameters. Standard GaAs is grown in an MBE system at a substrate temperature in the range of 550-600°C and the As_2:Ga (BEP) ratio is between 5 and 12. Ga is evaporated at a temperature of 800-1000°C, which provides a growth rate of 0.1-1 µm/hr and As is evaporated at 300-400°C inside a valved cell. The evaporation of As results in As_4 molecules that are broken into more reactive As_2 when they go through the cell long mouth, cracker, which is kept at 1000°C. The surface reconstruction of GaAs under standard growth conditions is 2×4 streaky lines. MBE GaAs at the standard high temperature growth conditions has the best crystal quality. Room temperature electron mobility higher than 8000 $cm^2V^{-1}S^{-1}$ for MBE grown GaAs has been reported [34].

GaAs can also be grown at lower temperatures down to 200°C and at smaller As_2:Ga (BEP) ratios, even with metallic Ga droplets forming on the surface, however the growth comes at the price of more crystal defects. It was shown by Mooney et. al [35] that the density of deep level defects gets 100× larger when the growth temperature drops from 580°C to 450°C.

Bi incorporates into GaAs when the growth temperature is lower than 400°C together with an As:Ga atom flux ratio of 1 or less. The dependence of Bi incorporation on the inverse of substrate temperature is shown in figure 3.1. The lower the growth temperature the more Bi incorporates. The square data points are a set of samples grown by the author and used also for the plot in figure 4.1. They are grown at different substrate temperatures with all other growth parameters fixed as described in section 4.2. The triangle data points are copied from R. Lewis et al. [36]. The solid line is also a fit with equation 3.1 by R. Lewis et al.

$$\frac{dx}{dt} = \theta_{Ga}\theta_{Bi} - a_1 x F_{Ga} - a_2 x e^{-U/k_B T} \tag{3.1}$$

The left side of the equation is equal to zero in steady state. x is the Bi incorporation in the crystal, θ_{Ga} is the surface fraction that is Ga-terminated, θ_{Bi} is the Bi surface coverage, F_{Ga} is the Ga flux, U is the energy difference between an incorporated and surfactant Bi atom. k_B and T are the Boltzmann constant and growth temperature respectively. $a_1$and a_2 are fitting constants. The fit had been done on the Lewis' data at low substrate temperatures whereas the author's data fall on the high temperature end of the fit and show good agreement with the fit. The bonding energy of 0.28 eV was found from the fit for growth temperatures lower than 270°C for the Lewis' data [36]. The agreement between the Lewis fit and my high temperature grown samples shows that the same bonding energy can be assumed for the high growth temperatures. The steep drop in Bi concentration for 1000/T < 1.6 corresponds to the temperature where surface Bi coverage begins to fall below unity.

The incorporated Bi atoms take As sites in the GaAs lattice. Arsenic makes stronger bonds with Ga and it can displace Bi atoms, therefore to improve the possibility of Bi atom incorporation, the As pressure is decreased to values close to the stoichiometric condition where As:Ga =1 and the surface becomes Ga terminated. When the growth temperature is less than 400°C and the Bi flux is fixed, the Bi incorporation depends only on the As_2:Ga ratio which is controlled by the As cell valve. There is almost zero Bi incorporation at large As:Ga ratios, but the Bi incorporation increases sharply when the As:Ga ratio gets close to 1:1. The incorporation saturates when the surface is Ga terminated and metallic Ga droplets appear [36].

Larger Bi flux provides more Bi atoms for incorporation. It has been shown by several MBE groups that Bi incorporation increases linearly with Bi flux at low Bi flux when the As:Ga ratio and growth temperature and growth rate are fixed [36,37]. Bi incorporation reaches saturation at large Bi flux when the surface is completely Bi covered and metallic Bi droplets start to form.

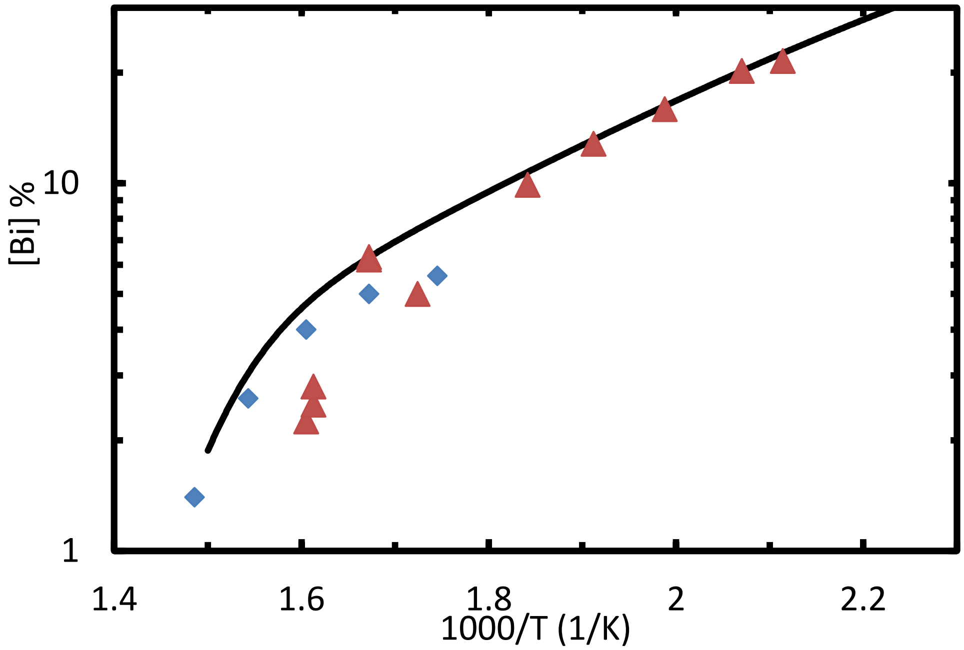

Figure 3-1: Bi incorporation as a function of inverse substrate temperature. The square data points are a set of samples used also for the plot in figure 4.1. They are grown at different substrate temperatures with other growth parameters fixed as it is described in section 4.2. The triangle data points belong to R. Lewis et al. [36]. The solid line is also a fit with equation 3.1 by R. Lewis et al. The Bi contents were found from (004) x-ray scan simulation.

Lowering the growth rate (Ga flux) with Bi flux and As:Ga ratio fixed, increases the Bi incorporation and the Bi droplets form faster on the surface. Further reading about the effect of growth rate on Bi incorporation and droplet formation can be found in Ptak et al. [37].

3.3. Vertical cavity semiconductor laser with external mirror

Growth of GaAsBi was described in the previous section. In the following, we explain what a multiple quantum well (MQW) vertical external cavity surface emitting laser (VECSEL) is about.

Yellow light laser sources have many applications such as optical pumping, laser projection displays and medical treatments and diagnosis. Hemoglobin of the blood cells has absorption peaks in the range of yellow spectra that makes yellow lasers very important for eye surgery [38]. Also, many of the fluorescent markers that are used in fluorescence medical imaging have a depletion wavelength in the yellow range and are important for dermatology. The depletion wavelength is a sub-bandgap emission in the fluorescent markers [39]. With all these important applications for high power yellow lasers, there are still serious imperfections in the existing yellow laser technologies. Semiconductor lasers with a direct yellow lasing wavelength have been achieved in the GaInP system but its efficiency is rather poor [40]. Amplification and frequency doubling in solid state lasers also produces yellow light which is known to be complex, expensive and limited in output power [41].

Recently, VECSEL technology, also known as semiconductor disk laser technology has been utilized to obtain high power yellow light source with several advantages [42]. In this method, an intra-cavity nonlinear crystal converts the infrared emission of the VECSEL's semiconductor gain medium into yellow light by frequency doubling. VECSELs have good beam quality with high output power. The output wavelength can be tuned over tens of nanometers without any gaps in between. Low carrier lifetime of the semiconductor gain medium makes it possible to modulate the output by simply modulating the pump laser on a time scale of hundreds of nanoseconds [42-47]. The structure of the VECSEL is described in section 3.3.2.

Yellow light VECSELs were first demonstrated by Optoelectronic Research Centre (ORC) in University of Tampere, Finland. They achieved high power yellow light from the InGaAs/GaAs and InGaAsN/GaAs material systems by frequency doubling [42,48]. One of the superiorities of their design is using GaAs alloys as the gain medium which makes it possible to grow the whole structure on a GaAs substrate with a DBR (distributed Bragg reflector) mirror of GaAs/AlAs layers. GaAsBi is a new direct bandgap GaAs alloy with infrared PL emission which grows highly strained on GaAs substrates. It can be a perfect replacement for InGaAs material at long wavelengths (1300nm to 1500nm) when the structure is grown on GaAs substrates. Dr. Guina from ORC, University of Tampere suggested a VECSEL GaAsBi/GaAs structure as a cooperative project in October 2012. I was being trained as an MBE grower at that time so I accepted the challenge. The MBE system experienced several failures in 2013 and at last the project was started in September 2013.

3.3.1. Lasing conditions

When the number of excited atoms in a medium is more than the number of ground state atoms, a population inversion is said to exist. A medium with a population inversion can amplify a wave passing through due to stimulated emission. If we want the medium to act as an oscillator (laser) a part of the output must be fed back to the system. One way is to put the gain medium in between a pair of mirrors to form what is called a resonator cavity. In this way various possible modes of the cavity are excited by the gain medium spontaneous emission. Each mode has a certain amplification gain obtained from the medium and loss due to the mirrors and medium absorption. If the gain cannot compensate for the losses the mode dies out. But the modes in which the gain overpowers the losses are amplified and draw energy from the gain medium. The amplitude of the amplified modes increases until the population inverted upper level is depleted to a value of which the gain is equal to losses and the mode oscillates in steady state. The condition of the gain being equal to the loss is important and indicates the beginning of lasing and is called the threshold condition. We focus on semiconductor lasers in the following section.

3.3.2. Multiple quantum wells as a laser gain medium

The gain (active) region in a semiconductor laser is the part of the hetero-structure where electrons and holes recombine, so the emission wavelength depends on the active region material bandgap. A schematic of a VECSEL is shown in figure 3.2. The VECSEL structure has GaAsBi/GaAs MQWs as the active region. The structure is pumped optically by an 808 nm laser which generates electrons and holes in the GaAs barriers. The carriers fall into the GaAsBi QWs with smaller bandgap and recombine to emit light. The gain region is terminated with a $Al_{0.3}Ga_{0.7}As$ window to reduce surface recombination. A 10 nm GaAs cap layer protects the AlGaAs from oxidation. The active region needs to be inside a cavity to lase. The cavity is made out of a distributed Bragg reflector (DBR) at the bottom and an external mirror at the top. Three calibrations were done before the final VECSEL structure was grown: QW, $Al_{0.3}Ga_{0.7}As$ and DBR.

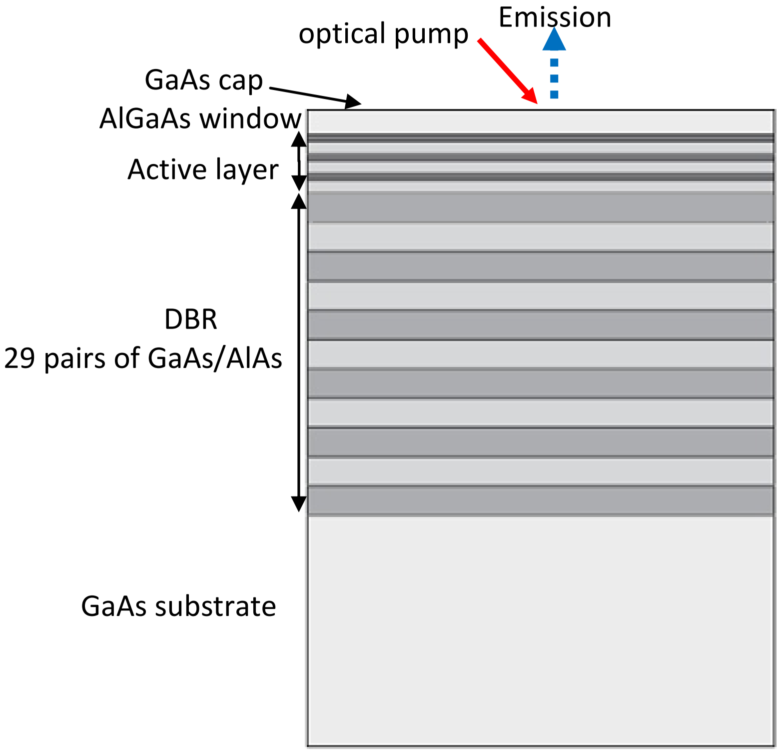

Figure 3-2: Schematic of a VECSEL structure: The active layer consists of GaAsBi QWs separated with GaAs barriers. The external mirror is not shown in the picture. The picture is not drawn to scale.

The first step to grow a VECSEL is to adjust the Bi content of GaAsBi so that the QWs emit at the desired wavelength (1175nm). The Bi content is approximated from the dependence of GaAsBi bandgap on Bi% plot that is looked up from related papers [30] and it is found to be 5-6% incorporation. Figure 3.3 and 3.4 show the x-ray scan and PL emission of an epi-layer GaAsBi calibration sample. The match between the fringes of the x-ray measurement and its simulation in figure 3.3 indicates that the layer is strained and uniform [36]. The growth parameters (arsenic valve, growth temperature and Ga, As and Bi fluxes) of a successful calibration sample are used as the starting point for the single quantum well calibration sample.

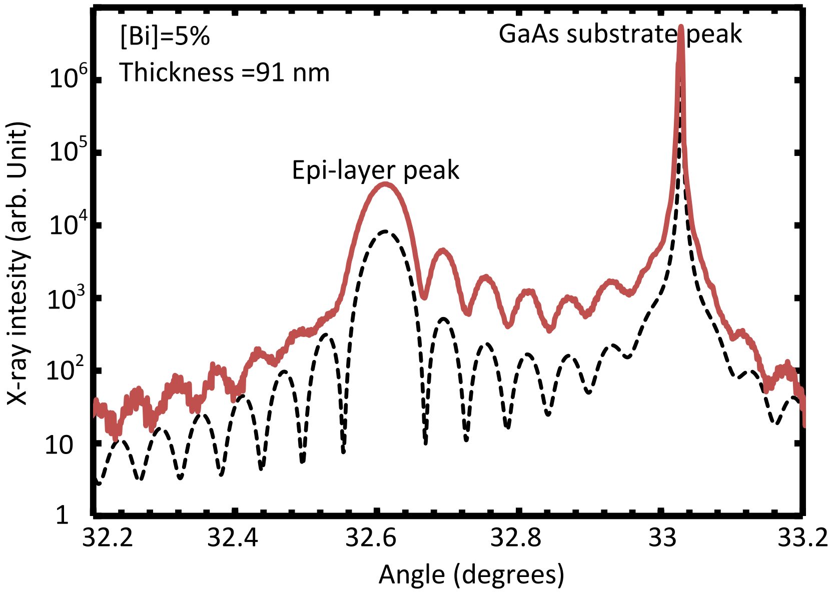

Figure 3-3: (004) x-ray scan of a 5% Bi content GaAsBi layer grown at 300°C (r2403). The dotted line is the simulation of the scan by LEPTOS software. The simulation parameters are shown on the top left side of the figure.

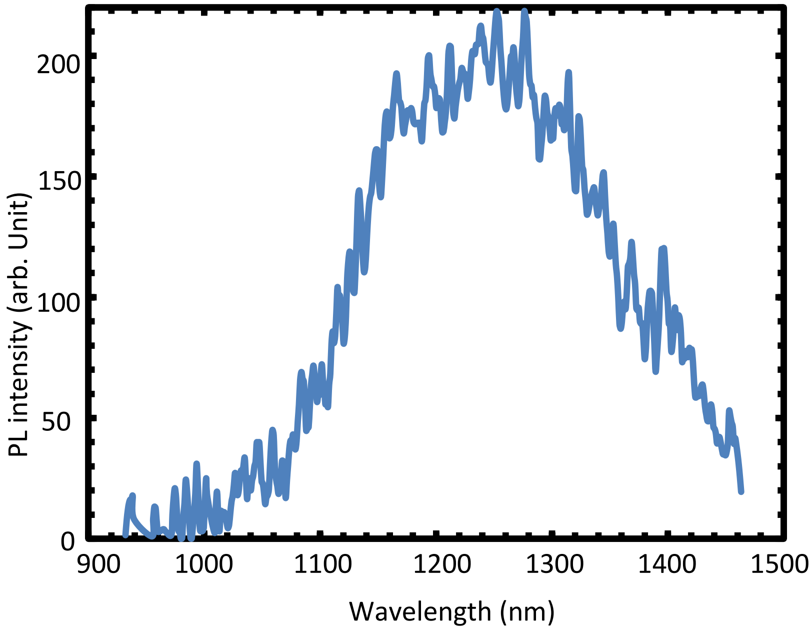

Figure 3-4: PL emission of the 5% Bi content GaAsBi layer whose x-ray scan is shown in figure 3.3 (r2403).

A single quantum well GaAsBi is grown with two growth-interrupts (GI) before and after the QW layer. The growth temperature and arsenic valve are lowered to the values necessary for Bi incorporation during the GI and then Ga and Bi shutters are opened simultaneously to deposit the QW. After the QW growth, the growth temperature is raised to 570°C and a GaAs cap layer is grown at standard growth conditions to cover the QW. The Bi covering the surface evaporates when the temperature is being increased to 570°C.

The growth dynamics of a QW are different from a thick GaAsBi layer. QW growth time is short and the cells fluxes are not stabilized therefore the surface is in a transient state unlike a thick layer which grows in steady state. Several QW calibration samples are needed to adjust the growth time and parameters exactly for the desired emission wavelength. X-ray diffraction and PL emission of a QW calibration sample are shown in figure 3.5 and 3.6. The composition and thickness of the QW are inferred from fitting its x-ray scan and also the growth rate is found and later used for the final VECSEL structure. Full width half maximum (FWHM) of the PL emission (figure 3.6) is about 150 nm which is broad in comparison to InGaAs QW emission (50 nm) [50].

It was shown by Lewis et al. [36] that GaAsBi films with 14% Bi incorporation grows pseudo-morphically up to 50 nm so there is no need to show that QWs with 6% Bi content and less than 10 nm thickness are completely pseudomorphic.

Lattice misfit is the relative difference of the film fully relaxed lattice constant (a_f) with the substrate lattice constant (a_s) [51]:

$$m = \frac{a_f - a_s}{a_s} \tag{3.2}$$

The fully relaxed lattice constant is calculated from Vegard's law with the Bi content which is found from x-ray diffraction measurements. In the pseudomorphic films the lattice misfit can also be calculated from the lattice mismatch ($a_\perp - a_s$) [51]:

$$m = \frac{1-\nu}{1+\nu} \times \frac{a_\perp - a_s}{a_s} \tag{3.3}$$

ν is the Poisson ratio for the film which is taken the same as GaAs, 0.31 [30]. The effect of Bi alloying on the elastic constants is unknown hence the GaAs Poisson ratio can cause non-negligible error for high Bi content samples ([Bi]>10%). The actual lattice constant ($a_\perp$) of the QW sample in figure 3.3 ([Bi]=5%) is calculated from equation 3.3 and plugged into the out of plain strain ($\epsilon_\perp = \frac{a_\perp - a_f}{a_f}$) relation. The resulting value of the out of plain strain is 0.53%.

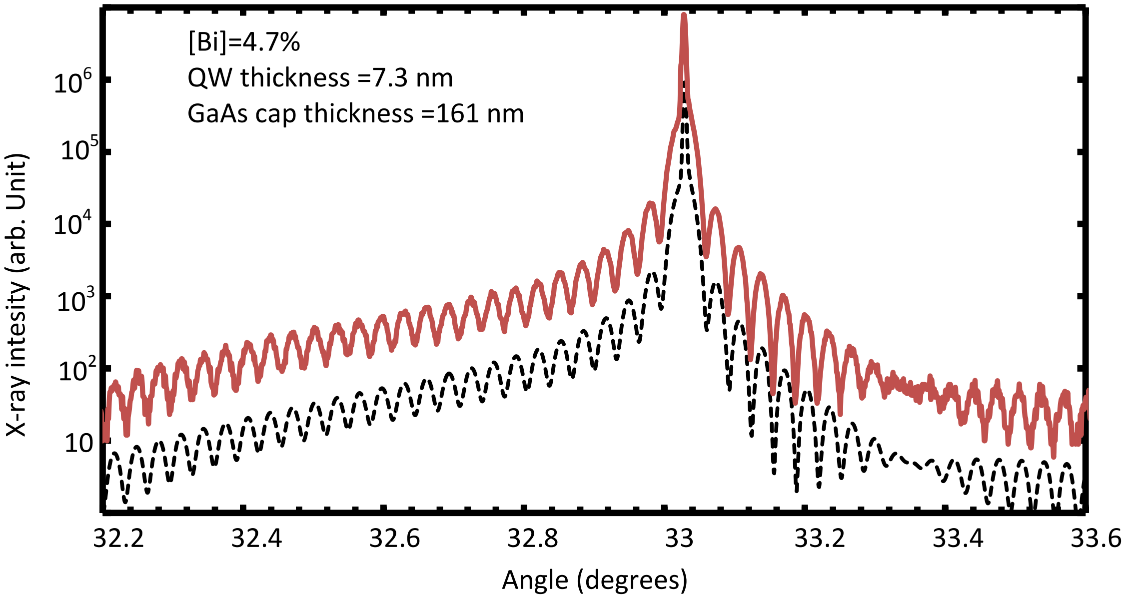

Figure 3-5: X-ray of a calibration GaAsBi QW which was grown at 300°C. (r2476) The dotted line is a simulation by LEPTOS software. The simulation parameters are shown on the top left side of the figure.

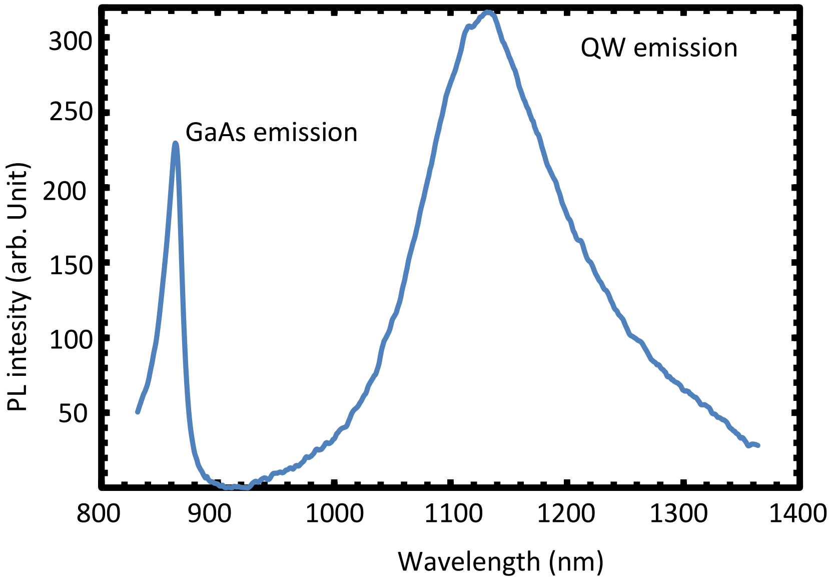

Figure 3-6: PL emission of the GaAsBi QW whose x-ray scan is shown in figure 3.5 (r2476).

3.3.3. DBR Calibration

The VECSEL cavity consists of 29 pairs of 100.51/85.54 nm AlAs/GaAs DBR on the substrate side. AlAs on GaAs substrate is the perfect choice for DBR as AlAs lattice mismatch with GaAs is very small and it can be grown up to 100 nm without any dislocation or relaxation concerns. The huge difference in the refractive indices of GaAs and AlAs (3.40 and 2.92) makes it possible to achieve a wide bandwidth reflectivity that guarantees the main cavity mode to be covered in its spectrum. Figure 3.7 shows the reflectivity spectrum of the very first AlAs/GaAs DBR. The thicknesses of the AlAs and GaAs layers are inferred from (004) x-ray scan of the sample (figure 3.8). Even though the total sample thickness is more than 4.5µm, the layer is still high quality single crystal with sharp x-ray peaks.

A cavity with length L allows all the modes with the wavelength of $\lambda = 2nL/m$ to oscillate where n and m are the gain medium refractive index and an integer number respectively. If the cavity of a VECSEL is taken as between its surface and the DBR, then the main mode of the cavity ($m = 1$) has the following relation with the GaAs barrier and GaAsBi QW thicknesses:

$$thickness_{GaAs\ Barrier} + thickness_{GaAsBi\ QW} = \lambda_{lasing}/(2 \times n_{GaAs}) \qquad (3.4)$$

The QWs are placed at anti-nodes of the cavity (half wavelength distances). The main mode wavelength is designed to be at the centre of the flat top of the DBR reflectivity spectrum so the AlAs and GaAs DBR layers thicknesses have to be ¼ of the lasing wavelength:

$$thickness_{AlAs} = \lambda_{lasing}/(4 \times n_{AlAs}) \qquad (3.5)$$

$$thickness_{GaAs} = \lambda_{lasing}/(4 \times n_{GaAs}) \qquad (3.6)$$

And the central wavelength of the DBR can be calculated as:

$$\text{Central wavelength} = 2 \times (n_{AlAs} \times thickness_{AlAs} + n_{GaAs} \times thickness_{GaAs}) \qquad (3.7)$$

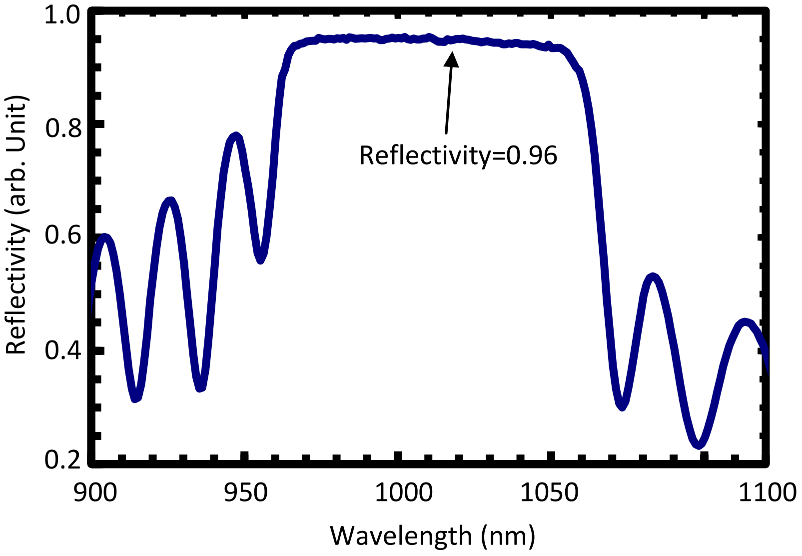

Figure 3-7: The measured reflectivity spectrum of an AlAs/GaAs DBR (r2449).

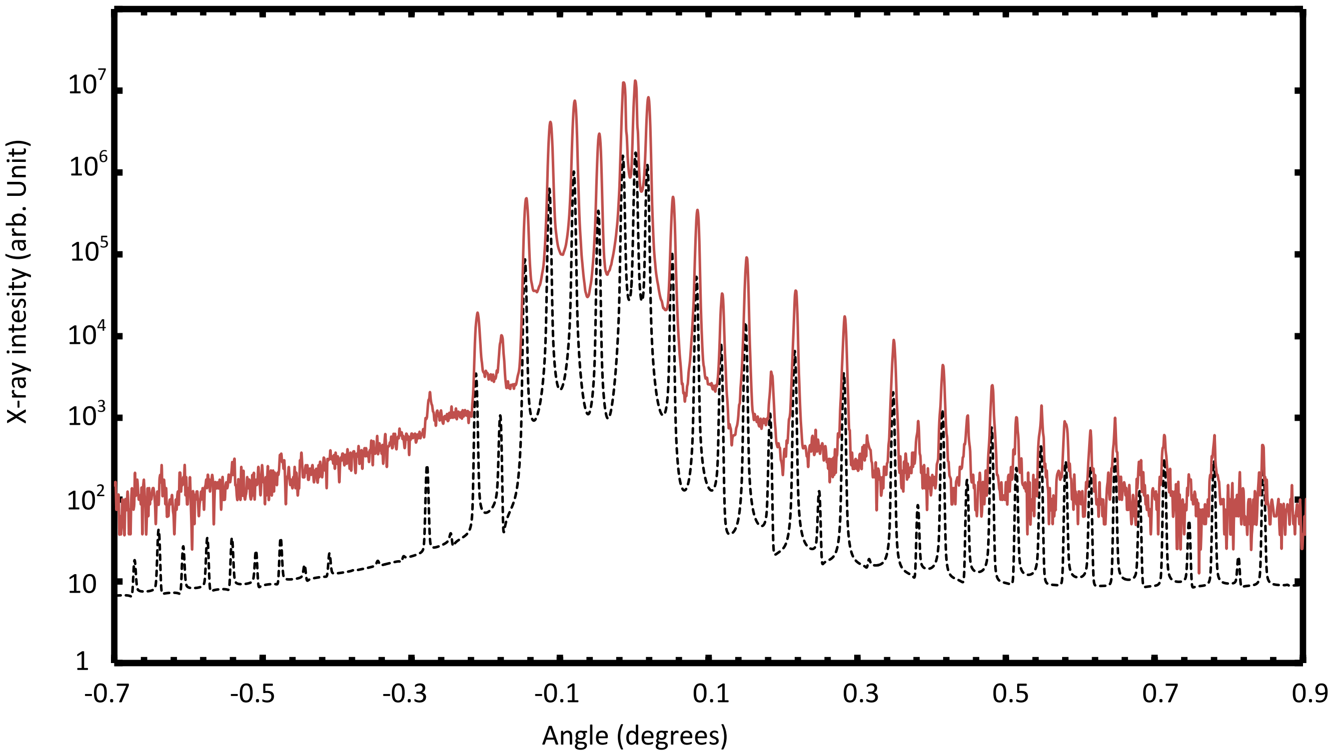

Figure 3-8: The (004) x-ray scan of the DBR sample shown in figure 3.7 (r2449). The dotted line is a simulation. The sample consists of 29 layers of 75.2 nm AlAs alternating with 29 layers of 84.3 nm GaAs. The substrate angle has been moved to 0°.

Growing a complete DBR with 29 GaAs/AlAs pairs takes more than 12 hours and needs the cells to be hot all the time and consumes a lot of material. It is quite impractical to grow the whole DBR to see if the central wavelength is at the desired value. One calibration method for DBR growth is to grow a structure with only 7 GaAs/AlAs pairs and one singularity in between them (figure 3.9). The reflectivity spectrum of such a structure has a dip at its central wavelength which can also be predicted from equation 3.7. The thicknesses of the AlAs and GaAs layers are inferred from the (004) x-ray scans and give us the growth rate of the AlAs and GaAs. The reflectivity measurement confirms the central wavelength position and the final DBR can be grown with the values from the calibration. Figures 3.10 and 3.11 show the reflectivity and x-ray scan of one of the DBR calibration samples. It should be noted that the central wavelength was designed to be at 1210 nm and the purpose of the sample was to find the growth rates.

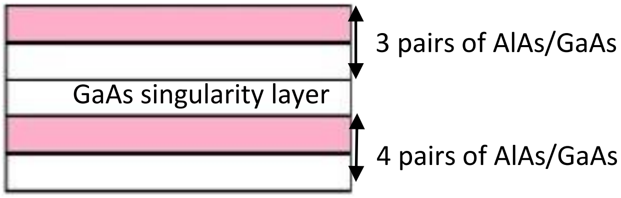

Figure 3-9: A DBR calibration sample with a singularity in the middle.

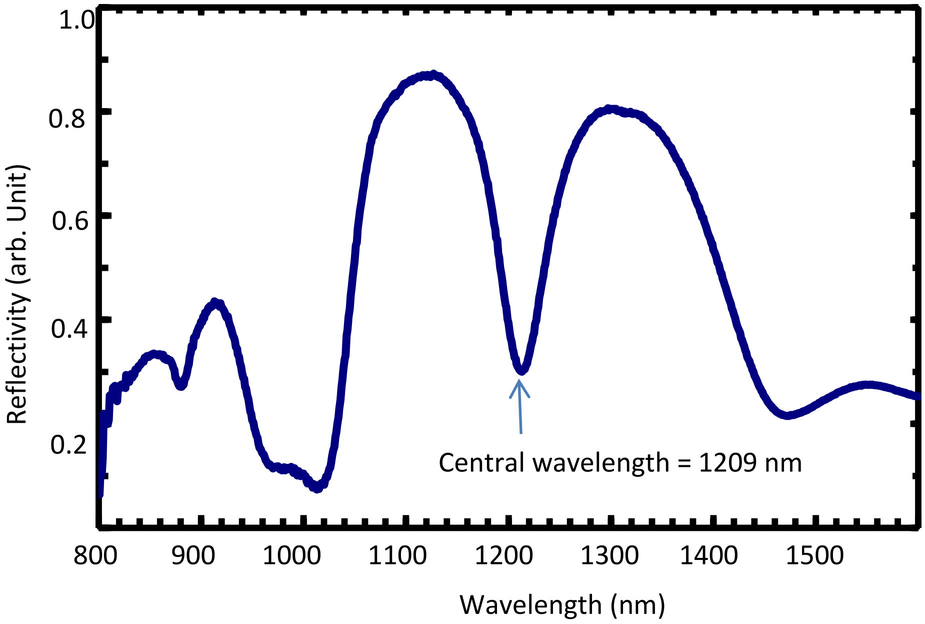

Figure 3-10: The reflectivity spectrum of a DBR calibration sample with the structure shown in figure 3.9 (r2455).

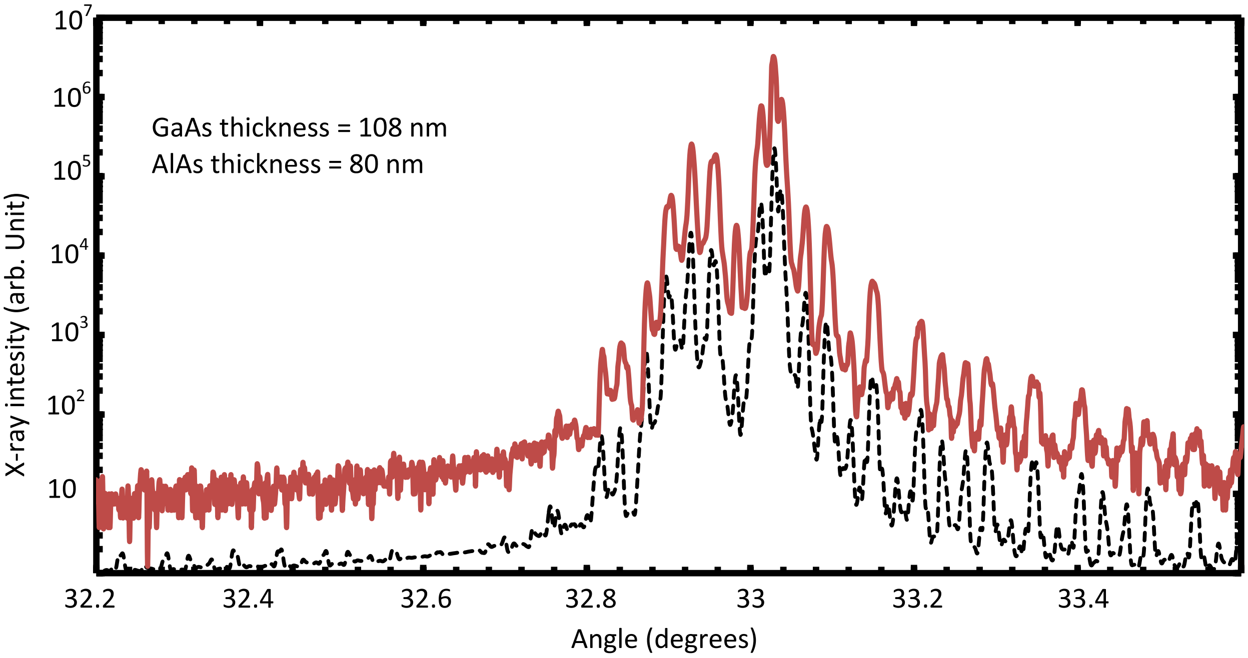

Figure 3-11: The (004) x-ray scan of the DBR calibration sample whose structure is shown in figure 3.9 and its reflectivity in 3.10 (r2455).

The last part of the VECSEL that needs calibration is the $Al_{0.3}Ga_{0.7}As$ window. The ratio of the Ga flux to the Al flux determines the Al fraction. The growth rate also changes with the fluxes. A half dozen samples with different cell fluxes were grown until the 30% Al content was achieved. Figures 3.12 shows a (004) XRD scan of a successful $Al_{0.3}Ga_{0.7}As$ calibration sample. Some of the AlGaAs samples that were grown for the VECSEL project were also used by R. Lewis for his investigation of the effect of the chiller cooled shroud on the MBE growth quality based on PL intensity from AlGaAs layers [23].

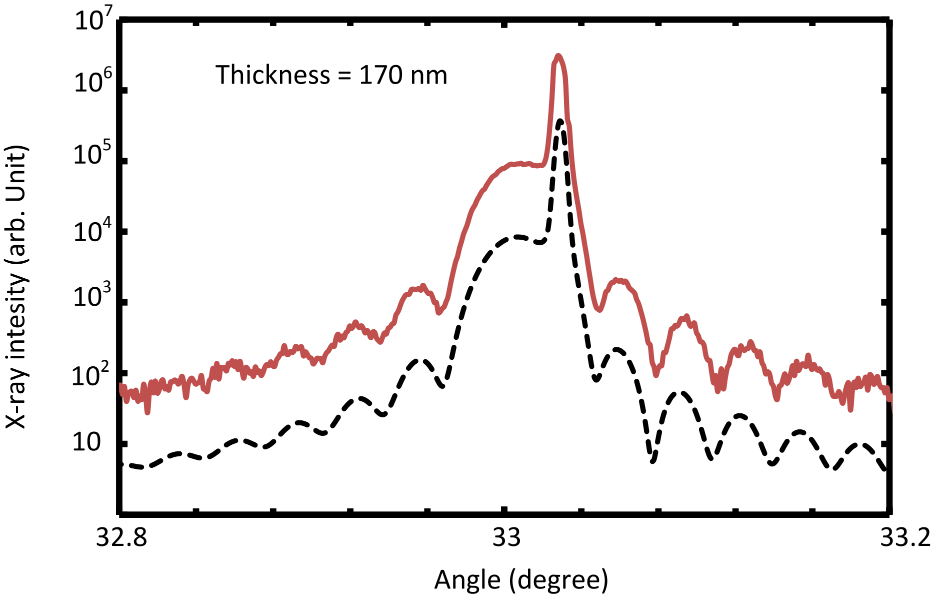

Figure 3-12: The (004) x-ray scan of an $Al_{0.3}Ga_{0.7}As$ calibration sample (r2475). The dotted line is a simulation.

3.4. Growth procedure, structure and optical properties of the VECSEL

3.4.1. Shutter automation

To grow 29 pairs of GaAs/AlAs layers, the cells shutters have to be controlled by computer but the MBE had pneumatic shutters controlled by manual switches at the time when I started the project. A pneumatic valve changes the direction of the compressed air to a shutter when its voltage is switched between high and low level.

A simple schematic in figure 3.13 illustrates the circuit of the computerized shutters. A "National Instrument NI-DAQmx" device was added to the MBE's computer to communicate with the analogue side of the circuit. This DAQmx card has an eight pin output port that gives 0/1 (H/L) order to VG-semicon shutters control unit through a box of relays. The output of the shutter control unit is used as the order signal for a relay that switches the voltage supply of the pneumatic valve coils. Connecting the computer directly to the external power supply was risky as the computer controls several units on the MBE, so the shutter control unit was used as a buffer. The output of the unit did not have enough electric power to actuate pneumatic valves. This problem was solved by using the relays with an external power supply.

National Instrument has developed a universal VI for all DAQ devices which is called "DAQ Assistant". This new VI is supported in LabVIEW version 8 or later and it can detect the DAQ device on a computer's PCI port automatically. It takes the output status as data and sends them to the DAQ card PCI port. The MBE's LabVIEW program was modified to include the necessary VIs for the DAQmx card (figure 3.14). The LabVIEW component "select" chooses between "entered data" and "initial values" based on "pattern" variable. When the MBE program is started pattern is true and the initial values are sent to the DAQ card which sets all the shutters to be closed then pattern changes into false and the user can manipulate shutters by changing the entered data through command line codes.

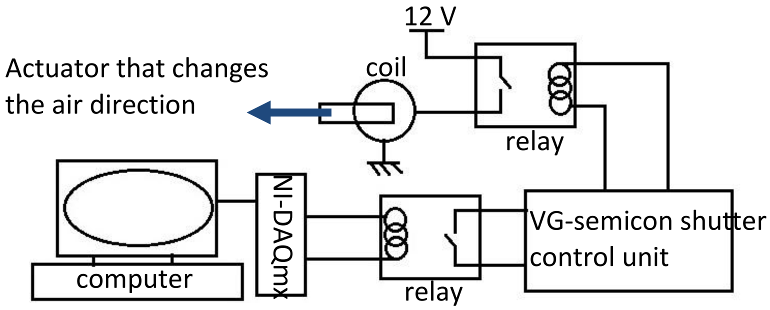

Figure 3-13: Schematic of the computerized control for the cell shutters.

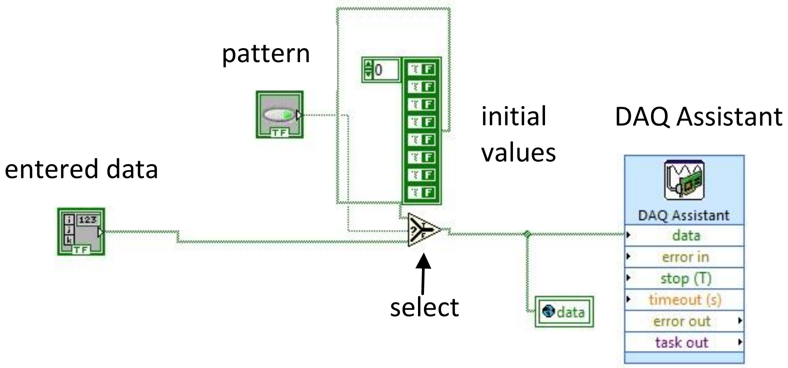

Figure 3-14: Piece of LabVIEW program that was added to computerize control for the cell shutters.

3.4.2. Structure and optical properties of the VECSEL

A VECSEL with the structure shown in figure 3.2 was designed using equations 3.4 to 3.7 for 1176 nm lasing wavelength. The structure was simulated in Finland to optimize the values. The computer codes of the simulation were not available for this thesis. Figure 3.15 shows the electric field of the light with the optimized layer thicknesses. The field decays in the DBR as it is reflected by the DBR layers and it turns into a standing wave when it enters from the DBR into the MQWs. The resulted optimized thicknesses are listed in table 3.1. The calibration samples were all aimed to achieve the layers with compositions and thicknesses needed to achieve the table 3.1 values. The growth rates of the layers were dependent on the cells flux and found from the calibration samples through x-ray fitting.

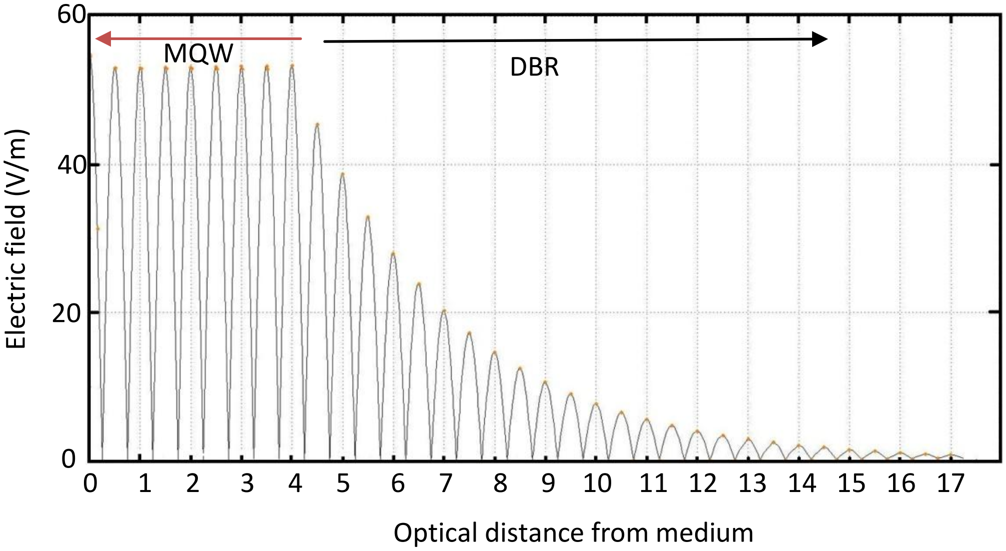

Figure 3-15: Electric field calculation in the VECSEL layers for 1176 nm lasing wavelength. The simulation was done in Tampere University, Finland.

The growth of a VECSEL structure took 22 hours of MBE growth. Being ~6μm thick, the VECSEL sample is the thickest sample ever grown with the UBC and UVIC MBEs. The sample's PL and reflectivity were measured to understand the optical properties of the structure and they are shown in figure 3.16. The reflectivity spectrum has a flat top with a dip at 1140 nm. The dip in the reflectivity is the result of the standing wave in between the DBR and the surface at 1140 nm. The standing wave stimulates the carriers to emit at its wavelength so the PL emission has a sharp peak exactly at the dip in the reflectivity. The (004) XRD scan of the VECSEL was simulated and shown in figure 3.17. The simulation confirmed the layer thicknesses with the maximum variation of 5% from the desired values.

Table 3-1: Thicknesses and compositions of the VECSEL designed for 1176 nm resonance.

Layer composition	Thickness (nm) in the design	Thickness (nm) measured from XRD fit	Growth rate(nm/sec) from calibrations	
GaAs	5	5	0.136	
$Al_{0.3}Ga_{0.7}As$	50	60	0.195	
GaAs	115.8	115	0.136	
GaAsBi QW	7	7	0.117	7X
GaAs barrier	163.53	158	0.136	
AlAs DBR	100.51	100	0.287	29X
GaAs DBR	85.54	79	0.079	

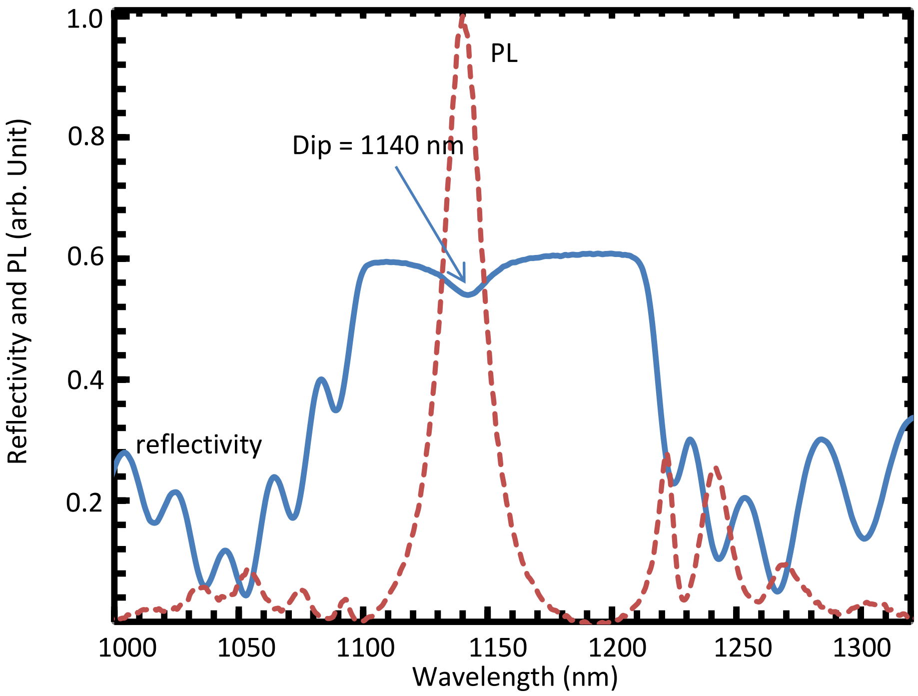

Figure 3-16: PL and reflectivity spectrum of a VECSEL structure grown at UVIC (r2477).

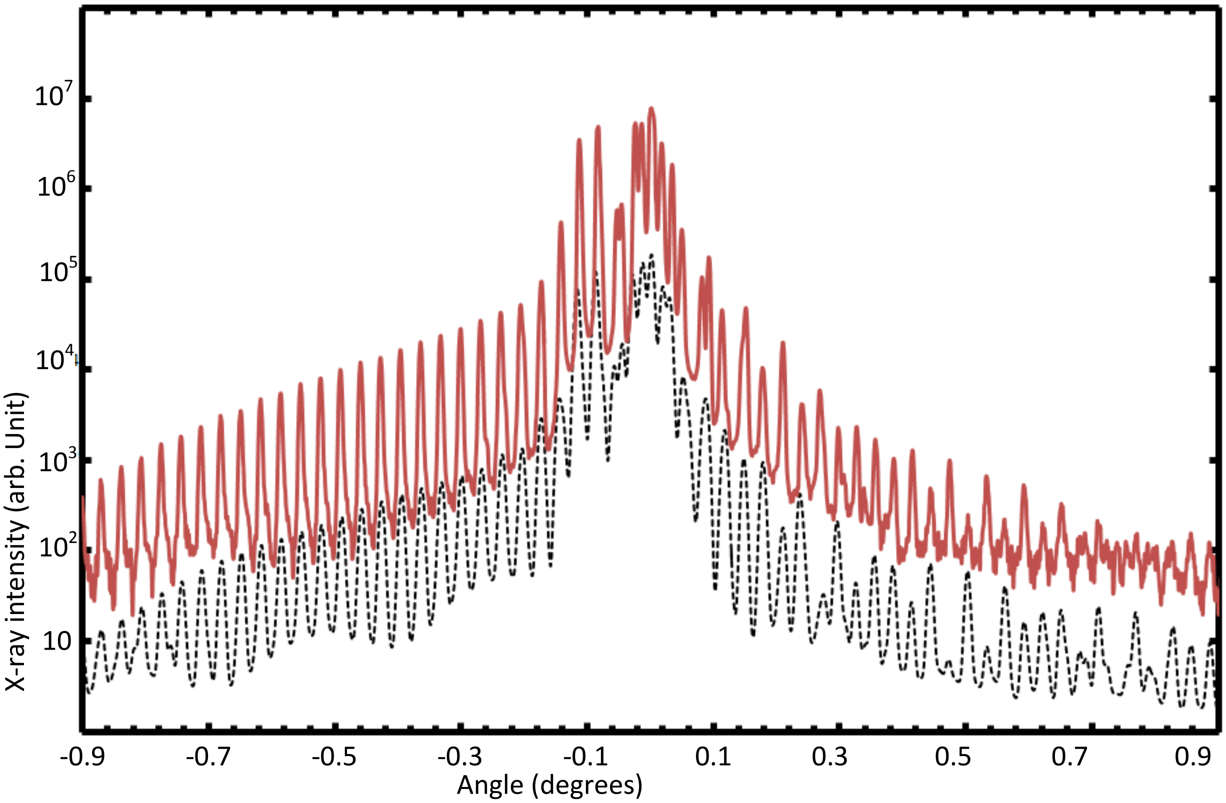

Figure 3-17: The (004) x-ray scan of the VECSEL structure (r2477) and simulation, the substrate peak is at 0°. The XRD fit parameters are listed in table 3.1.

3.4.3. Optical setup for the VECSEL laser

After the initial measurements, the sample was mailed to Tampere University for the lasing experiment. There, the quarter wafer sample was scribed into 2.5mm × 2.5mm chips and capillary bonded to a flat diamond heat spreader attached to a water-cooled copper mount. Then a V-shape optical setup shown in figure 3.18 was used to test the sample. The optical pump was a 200 W 808nm diode laser with a focused spot diameter of about 510 μm. Further information about the setup can be found in E. Kantola et al. [48]. The copper mount was cooled down to 4°C, but no lasing was detected even with highly reflective cavity mirrors (>99.8% reflectivity).

The failure in the VECSEL experiment brought up many questions about the probable cause. It was decided to investigate the quality of GaAsBi material for optical purposes which is the main topic of the next chapter.

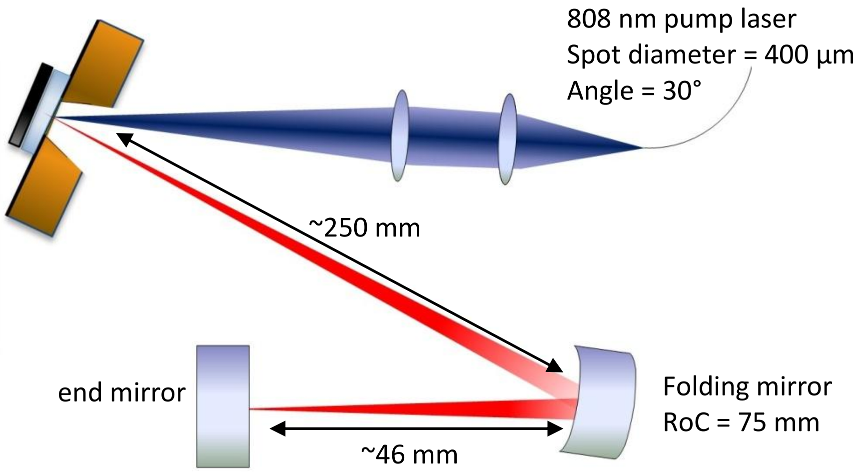

Figure 3-18: Schematic of the V-shape optical setup used for VECSEL experiment at Tampere University, Finland. RoC: radius of curvature.

4. Optimization of $GaAs_{1-x}Bi_x$ growth conditions

4.1. Contributions

This chapter mainly consists of my paper: “MBE growth optimization for $GaAs_{1-x}Bi_x$ and dependence of photoluminescence on growth temperature” [53]. All the experiments in this chapter including sample growth and measurements were done by me. Dr. Tiedje developed a theory about the relation of the sub-bandgap PL emission with the pump excitation intensity which was used to fit to the data. M. Masnadi-Shirazi helped me with the calibration of the detector of the PL setup.

4.2. GaAsBi growth parameters and PL spectrum

Four growth parameters which control Bi incorporation were discussed in section 3.2. The effect of three of the four growth conditions on the PL emission will be investigated thoroughly in this chapter. The three growth conditions are: growth temperature, As:Ga ratio and Bi flux. Growth parameters can affect the density of mid-gap defects which act as recombination centers. The PL intensity is sensitive to the density of non-radiative recombination centers therefore the effect of a growth parameter on the defect density appears in the PL intensity. The photoluminescence of GaAsBi alloys has been investigated as a function of Bi content by a number of researchers [30,54,55], but this chapter is the first systematic investigation of the effect of the various experimentally accessible growth parameters on the photoluminescence intensity and emission spectrum.

4.2.1. Growth temperature

It has been shown by Mooney et al [35] that deep level defect densities in GaAs increase 10-fold when the growth temperature is decreased from 390°C to 330°C, therefore, we expect that low temperature grown GaAsBi alloys will have a high density of defects. To investigate the effect of growth temperature on the defect density, a set of five samples, each consisting of a 100nm $GaAs_{1-x}Bi_x$ layer capped with a 10nm GaAs layer, were grown between 300°C and 400°C with growth temperature as the only variable parameter. The GaAs cap was grown at the same temperature as the $GaAs_{1-x}Bi_x$ layer with Bi shutter closed and As valve full open without any growth interrupt. The high As overpressure during growth of the GaAs cap layer means that residual Bi on the surface will not incorporate in the cap. The composition and thickness of the samples were determined by simulating the high resolution (004) x-ray diffraction scans using LEPTOS software assuming pseudomorphic growth and an assumed GaBi lattice constant of 6.33 A° [30]. An x-ray calibration factor of 0.33 Bi%/100 arcsec was obtained from the x-ray simulations.

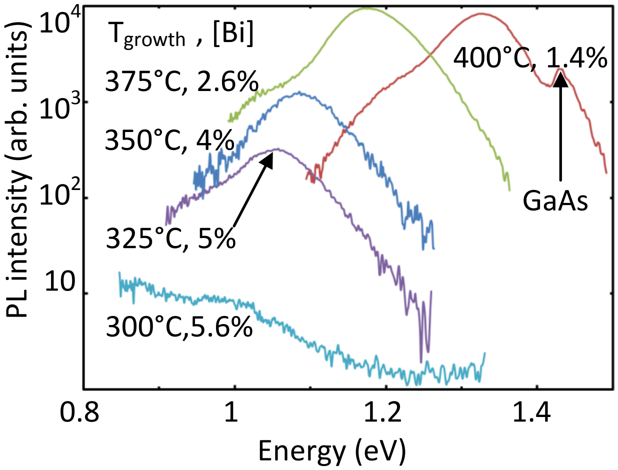

Figure 4-1: Dependence of room temperature PL intensity on growth temperature. All samples are 100nm $GaAs_{1-x}Bi_x$ layers capped with 10nm GaAs. They were grown at a stoichiometric As:Ga flux ratio and a Bi beam equivalent pressure of 1.18×10^{-8} mbar. The stoichiometric As_2:Ga BEP ratios of 2.4 and 2.9 were interpolated for the substrate temperatures of 300 and 330°C respectively. The Bi content is inferred from high resolution x-ray diffraction. The sample numbers are r2505 ([Bi]=1.4%), r2506 (2.6%), r2501 (4%), r2507 (5%) and r2508 (5.6%).

PL measurements were carried out on all five samples with the samples in the same position and with exactly the same optical alignment so that the PL intensity can be compared between samples. The results are shown in figure 4.1. Lowering the growth temperature leads to more Bi incorporation and lower PL intensity. No PL emission was detected from the 300°C sample even though the Bi content is almost the same as for the

325°C sample. As the growth temperature is decreased from 400°C to 300°C, with the other growth conditions kept fixed, the PL intensity drops more than 1000×. This trend suggests that the density of non-radiative recombination centres increases as the growth temperature decreases, similar to the case of GaAs.

4.2.2. Bismuth flux

We explore the effect of the Bi flux on the PL next. Bismuth shows a surfactant-like behaviour and tends to surface segregate and accumulate on the surface during the growth of $GaAs_{1-x}Bi_x$. The presence of the Bi surface layer can improve the electronic quality of the grown semiconductor. A set of three samples, similar to the above temperature dependent series consisting of 100 nm thick $GaAs_{1-x}Bi_x$ layers capped with 10 nm of GaAs, were grown with Bi beam equivalent pressures (BEP) of 0.7, 1.2 and 1.9×10^{-8} mbar, at a growth temperature of 350°C with other growth conditions fixed. Room temperature PL spectra for these samples under the same optical alignment are shown in figure 4.2. The increase in Bi BEP from 0.7 to 1.2×10^{-8} mbar increases the Bi content but it does not affect the PL intensity very much. The sample grown at 1.9×10^{-8} mbar BEP has 58% higher Bi BEP than the sample grown at 1.2×10^{-8} mbar but its Bi content is slightly lower (4.0% compared with 4.1%). A possible explanation for this behaviour is that once the surface is saturated with Bi, further increases in Bi flux leads to metallic Bi droplets on the surface but no increase in Bi content in the film. The high Bi flux 4.0% sample has droplets on the surface which were detected by an increase in the light scattering signal during growth whereas the 4.1% sample does not. The slight drop in Bi content may reflect small run-to-run variations in growth conditions or alternatively the droplets may be draining Bi atoms from the surface, reducing the surface coverage and causing the Bi incorporation to drop.

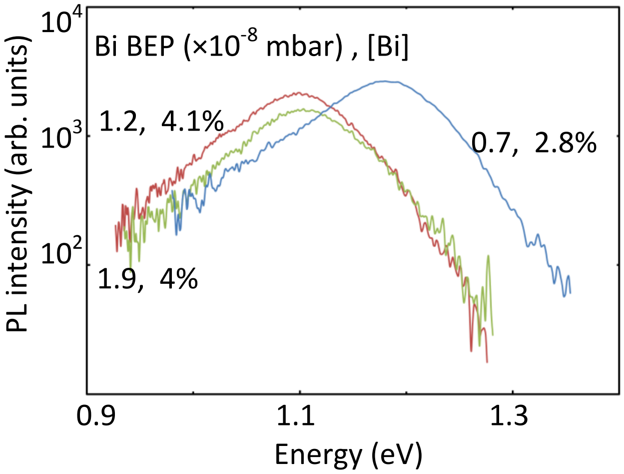

Figure 4-2: Dependence of room temperature PL intensity on Bi beam equivalent pressure. All samples are 100nm $GaAs_{1-x}Bi_x$ layers capped with 10nm GaAs. They were grown at stoichiometric As:Ga flux ratios (~0.9) and a substrate temperature of 350°C. The sample numbers are r2493 (2.8%), r2494 (4.1%) and r2495 (4%).

4.2.3. Arsenic flux

We now explore the effect of changing the arsenic flux. Bi incorporation is highly sensitive to As pressure in the vicinity of the stoichiometric As_2:Ga BEP ratio [36]. A set of four samples once again consisting of 100 nm thick $GaAs_{1-x}Bi_x$ layers capped with 10 nm of GaAs, were grown under exactly the same conditions except for small changes in the As_2 valve setting. The valve was set to the stoichiometric condition and three other nearby positions: 0.05 mm below stoichiometric (lower As_2 pressure) and 0.05 mm and 0.10 mm above the stoichiometric condition for a total of four samples with four different As_2 pressures. The very small changes in As_2 BEP's are indicated in figure 4.3 and were obtained by interpolation of pressures measured for large changes in valve position for which the difference in pressures could be measured with the ion gauge. The measured PL intensity for the four samples is shown in figure 4.3. As shown in figure 4.3 as the As_2 pressure is reduced the PL intensity drops and the Bi content increases. As expected the Bi content is highly sensitive to the arsenic flux. In fact the Bi content almost doubles with only a 5% reduction in arsenic flux. The Bi content is observed to be more sensitive to arsenic flux than predicted by the theoretical model of Lewis et al [36] for which the same change in Bi content would require a 9% change in arsenic flux.

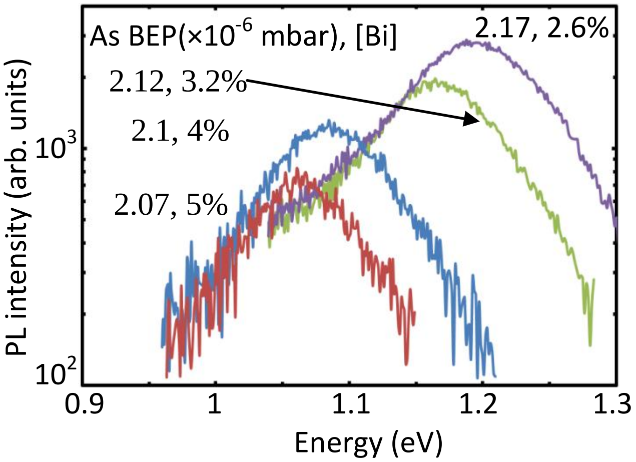

Figure 4-3: Dependence of room temperature PL intensity on As beam equivalent pressure. All samples are 100nm GaAs1-xBix layers capped with 10nm GaAs. They were grown at Bi BEP of 1.18×10^{-8} mbar and a substrate temperature of 350°C. The growth rate is 1μm/hr. The sample numbers are r2502 (5%), r2501 (4%), r2503 (3.2%) and r2504 (2.6%).

4.2.4. Temperature dependence of defect emission and bandgap

From the experimental results in figures 4.1, 2 and 3 we conclude that all three growth parameters affect the Bi content but that the growth temperature has the largest effect on the PL intensity. To investigate the effect of the growth temperature on the electronic properties of $GaAs_{1-x}Bi_x$, at fixed Bi content, we grew two samples with approximately the same Bi content (2.6% and 2.2% Bi) at different growth temperatures. The 2.6% sample was grown at 375°C and the 2.2% sample was grown at 330°C; we refer to these two samples as Sample A and Sample B respectively. The two samples were both grown with the stoichiometric As_2:Ga flux ratio. The tendency for higher Bi content in the sample grown at lower temperature was compensated by reducing the Bi flux for this sample. The thicknesses and growth conditions for the two samples are summarized in Table 4.1. The PL emission spectra in the temperature range from 8K to 300K are shown in figure 4.4 for both samples with the same excitation intensity and alignment of the optical spectrometer. Figure 4.4 shows that the peak room temperature PL intensity is about 5× higher in the high temperature sample (A) than in the low temperature sample (B). In addition Sample A is thinner than the absorption length of the 523 nm excitation wavelength [56]. Sample B on the other hand is thicker than the absorption length. Correcting for the difference in the absorption of the two samples at 523 nm will increase the PL intensity of the high temperature sample relative to the low temperature sample by a factor of 2. Furthermore the Bi concentration in sample A, is slightly larger than in sample B, (2.6% compared with 2.2%) therefore the degradation in PL intensity is not due to a higher Bi concentration since the higher Bi concentration sample has in fact a brighter PL.

Table 4-1: GaAsBi samples used for temperature dependent PL measurements, and grown at stoichiometric As:Ga flux ratios (As pressure of 2.1×10^{-6} mbar at 1μm/hr growth rate. As:Ga(BEP)=3).

sample	Growth temp. (°C)	Bi BEP ($\times10^{-8}$ mbar)	Thickness (nm)	Bi content
A(r2506)	375	1.18	100	2.6%
B(r2433)	330	0.73	280	2.2%

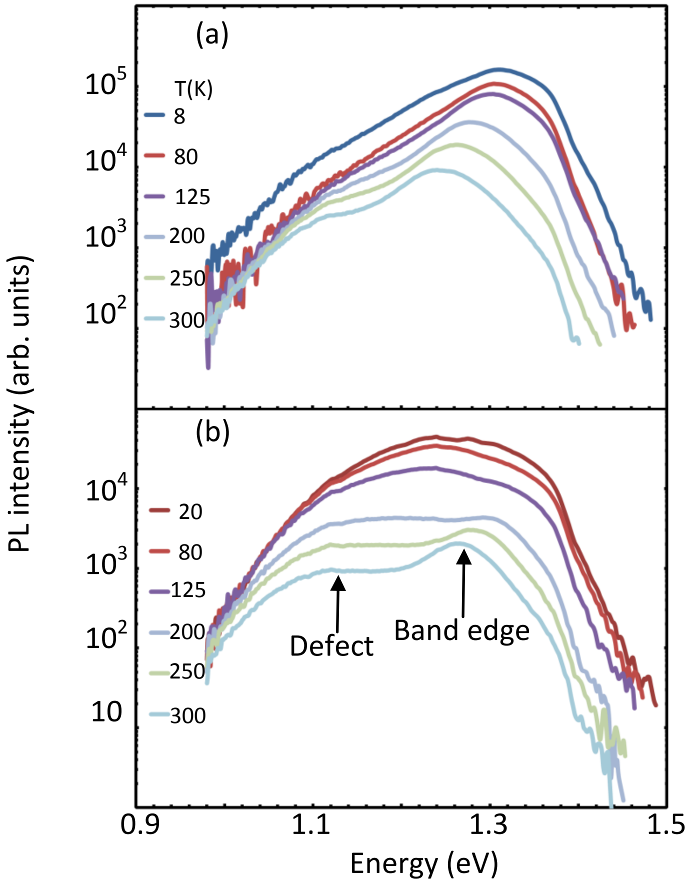

Figure 4-4: Temperature dependence of PL spectra for (a) sample A grown at 375°C and (b) sample B grown at 330°C. The weak temperature independent kink near 1.39 eV is associated with the rapid change in the InGaAs detector response at this energy that was not completely removed by the spectral calibration.

As shown in figures 4.4 and 4.5 each sample has a band edge PL emission peak as well as a lower energy PL emission in the form of a distinct peak or shoulder on the long wavelength side of the band edge peak. We assume that the low energy emission comes from shallow localized states in the bandgap near the valence band, associated with atomic scale fluctuations in alloy composition and/or with Bi clusters such as next nearest neighbour Bi dimers, trimers and so on [13,55,57,58,59]. The low energy emission is more prominent in Sample B, the sample grown at low temperature as shown in figure 4.4. Similar sub-gap emission peaks to that observed in our samples, have been reported for 4% and 6% Bi content samples by Mazur et al. [55]. The long wavelength emission dominates the PL spectrum at low temperature for the low temperature sample. This sample (B) grown at 330°C shows a distinct sub-bandgap emission peak below 150K while sample A grown at 375°C shows a weaker sub-gap emission consisting of a shoulder on the long wavelength side of the main band edge peak, even at the lowest temperature. The differences in the PL emission spectra for the two samples indicate that the concentration of shallow states in the bandgap decreases with increasing growth temperature. This may be due to growth temperature dependent Bi cluster formation or ordering [60-62].

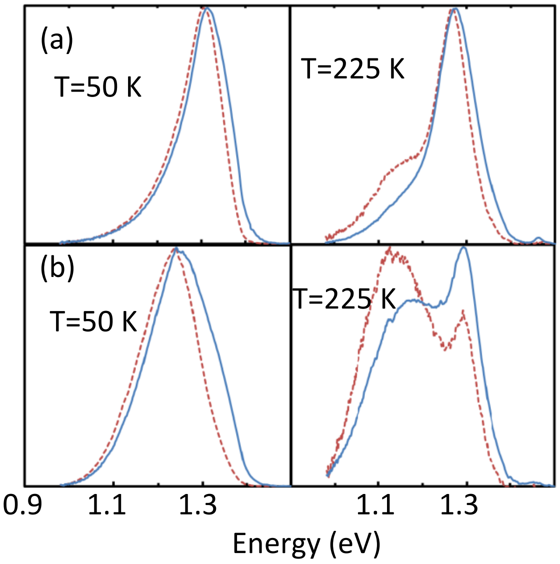

Figure 4-5: Normalized PL spectra for (a) sample A grown at 375°C and (b) sample B grown at 330°C with excitation intensity of 10^4 W/cm^2 (solid blue line) and 0.25×10^4 W/cm^2 (dashed red line), at 50K and 225K. Each spectrum was normalized to its own peak intensity.

If the sub-gap PL emission originates from localized Bi cluster states as proposed above, then the emission spectrum should depend on the pump intensity, since the occupation function for the localized states will depend on the density of holes in the valence band. To explore the pump intensity dependence, the PL measurements were repeated at lower excitation intensity. The normalized PL spectra of Samples A and B at 50K and 225K are shown in figure 4.5 for the full intensity pump and with the pump intensity reduced by a factor of 4. The band gap emission is relatively weaker at lower pump intensity, and shows a small 6 meV red shift in the high temperature sample (A) when the pump intensity was reduced. This intensity dependent shift is approximately independent of the measurement temperature. The small shift in the bandgap emission peak with pump intensity is interpreted as a band filling effect. The subgap emission peak has a relatively strong intensity dependence by comparison, that depends on temperature (figure 4.5b, see 225K). These results are qualitatively consistent with the subgap emission being associated with localized states [55].

In figure 4.6 we show the peak energies of the PL emission spectra as a function of temperature from room temperature to 8K for two different excitation intensities. The high temperature sample shows only one peak corresponding to the bandgap emission while the lower temperature sample shows two peaks, one corresponding to the bandgap emission and one corresponding to the sub-gap emission from localized states. The temperature dependence of the bandgap emission is expected to follow the temperature dependence of the bandgap, which can be fit most simply with an Einstein model which is known to give a good fit to the temperature dependence of the bandgap in semiconductors [63]. In this model the temperature dependence of the bandgap is given by,

$$\mathrm{E_g(T)} = \mathrm{E_g(0)} - \frac{S k_B \theta_\mathrm{E}}{e^{\theta_\mathrm{E}/\mathrm{T}} - 1} \qquad \text{(4-1)}$$

where $\mathrm{E_g(T)}$ is the bandgap as a function of temperature, $\mathrm{E_g(0)}$ is the bandgap at zero temperature, θ_E is the Einstein temperature for the material and S is a dimensionless coupling constant which describes the slope of $\mathrm{E_g(T)}$ as a function of temperature for $\mathrm{T} \rightarrow \infty$. We fit the energy of the bandgap emission peak as a function of temperature with equation 4.1 for T>200K using the Einstein temperature for GaAs ($\theta_\mathrm{E} = 270\mathrm{K}$) and taking $\mathrm{E_g(0)}$ and S to be adjustable parameters. The best fits are shown by the solid lines in figure 4.6. The corresponding fitting parameters are included in Table 4.2. The bandgap emission for sample A follows the fit down to 125K while in sample B the emission peak deviates from the solid line below 200K. Sample A follows the model over a wider temperature range because the sub-gap emission that causes the PL emission peak to shift to lower energies in Sample B, is relatively weaker in Sample A. We note that the dependence of the band edge emission energy on temperature in the temperature range where the bandgap emission is dominant is -0.35 meV/K and -0.25 meV/K for Samples A and B respectively.

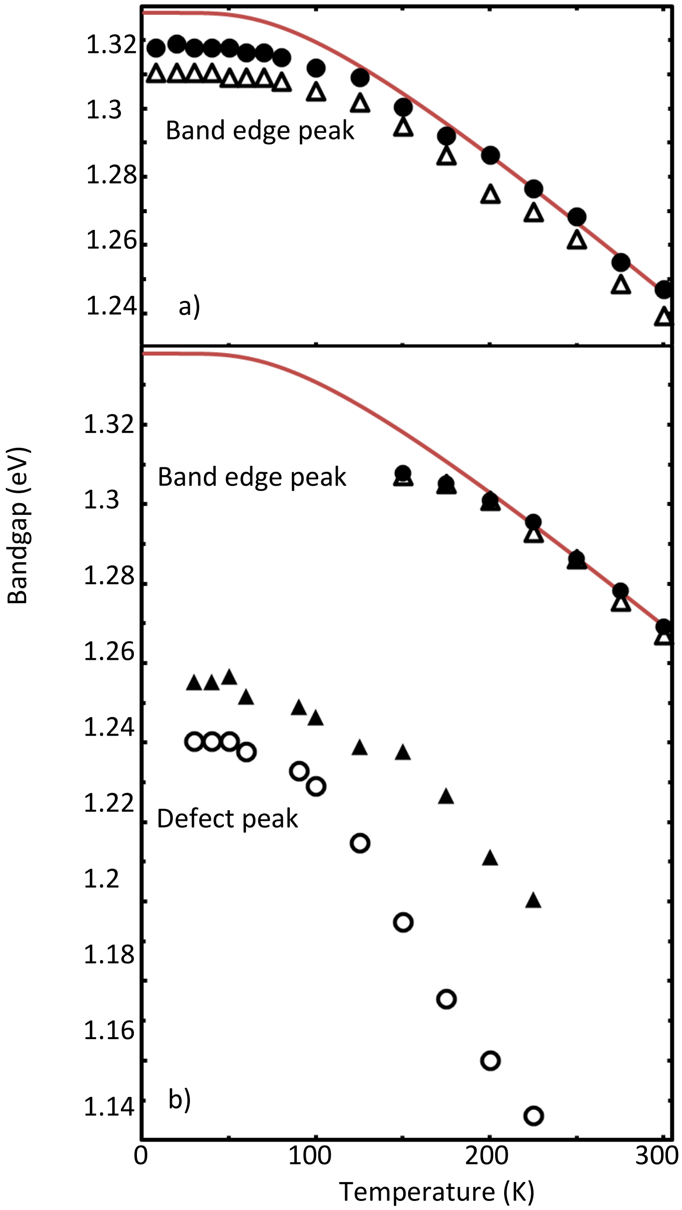

Figure 4-6: Temperature dependence of PL peak energies and Einstein fits for (a) sample A grown at 375°C (band edge emission) and (b) sample B grown at 330°C (band edge and defect emission) measured at an excitation intensity of 10^4 W/cm^2 (solid marks) and 0.25×10^4 W/cm^2 (empty marks). No distinct defect peak was observed in sample A as can be seen in figure 4.4. The peak energies were determined by picking the maximum of the curves.

The different temperature dependences for the bandgap for the two samples (sample A and B) which have almost the same Bi content, may help explain the contradictory reports in the literature on the temperature dependence of the bandgap for $GaAs_{1-x}Bi_x$ alloys [64-67]. Although Sample B has a lower temperature sensitivity than Sample A it is still larger than the temperature dependence observed by Tominaga et al. [65] (-0.18 meV/K with 2.5% Bi incorporation). Our explanation for the weaker temperature dependence of the PL emission energy in Sample B is that the higher density of sub-gap states in Sample B enables the holes to emit from lower energy states as the temperature drops, which partially compensates for the increase in the bandgap at low temperatures.

Table 4-2: Einstein fit parameters and temperature dependence of the bandgap for samples A and B and for GaAs.

sample	$E_g(0)$	S	$\Delta E/\Delta T$(meV/K) (150-300K)
A(r2506)	1.33	5.13	-0.35
B(r2433)	1.34	4.3	-0.25
GaAs	1.52 [63]	6.03 [63]	-0.42 [64]

4.2.5. Intensity dependence of defect emission

Optical absorption measurements show that $GaAs_{1-x}Bi_x$ with x~2.2%-2.6% has an exponential Urbach tail in the optical absorption edge with a characteristic energy E_0 = 0.03 eV at room temperature [30,68]. We take this exponential distribution to be a measure of the density of localized states associated with Bi cluster states in the bandgap close to the valence band. Under illumination the occupation function for the valence band tail states will be controlled by the position of the hole quasi Fermi level. Due to the competition between the energy dependence of the density of states and the energy dependence of the occupation function we expect to see a peak in the density of trapped holes in the vicinity of the hole quasi-Fermi level at low temperatures when $k_B T<E_0$. In this case recombination of electrons in the conduction band with trapped holes in the

valence band tail will give rise to a peak in the PL emission in the vicinity of the hole quasi-Fermi level which is below the bandgap energy.

As the PL excitation intensity increases the density of holes in the valence band will also increase and the quasi-Fermi energy will move closer to the valence band edge according to the expression,

$$\mathrm{E_{fp}} - \mathrm{E_v} = -\mathrm{k}_B\mathrm{Tln}(\mathrm{CF}^{\gamma}) \tag{4-2}$$

where $\mathrm{E_{fp}}$ is the hole quasi-Fermi level, $\mathrm{E_v}$ is the energy of the valence band edge, F is the optical excitation intensity, γ is a dimensionless exponent and C is a constant. In this expression we are assuming that the density of holes in the valence band depends on the excitation intensity raised to the power γ. The measured temperature dependence of the energy separation between the PL peak at the bandgap and the sub-gap emission peak is shown in figure 4.7 for the low temperature sample (B) for two different excitation intensities. As shown in figure 4.7, the energy difference is linear in temperature and decreases with increasing excitation intensity, consistent with equation 4.2.

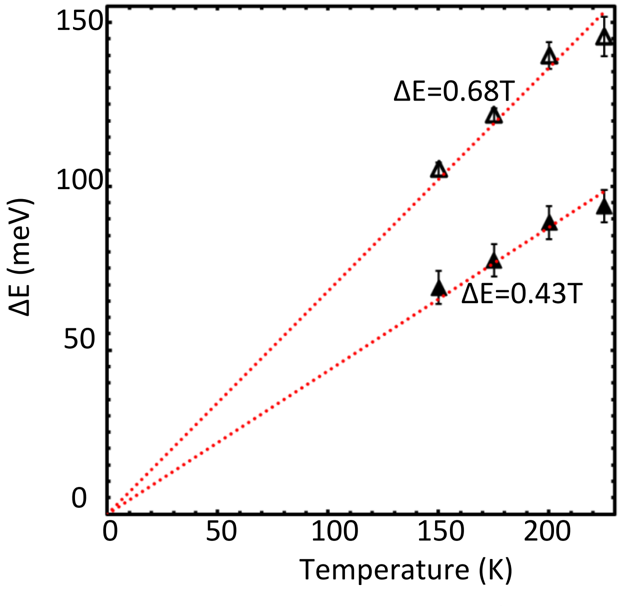

Figure 4-7: The energy separation between band edge and defect peaks in sample B at excitation intensities of 10^4 W/cm^2 (solid marks) and 0.25×10^4 W/cm^2 (empty marks) as a function of temperature.

The intensity dependence of the energy separation between the bandgap emission peak and the sub-gap emission peak is shown in figure 4.8 and is also consistent with equation 4.2, with $\gamma = 1.9 \pm 0.1$. Normally one would expect $\gamma < 1$ [69]. For example in the case of radiative recombination for which $F \sim Bp^2$, γ is equal to 0.5. Supralinearity in the carrier density as a function of light intensity can occur if there are two different types of recombination centres with different capture cross sections for electrons and holes and the dominant recombination channel shifts from one type of recombination centre to the other as the light intensity increases [69].

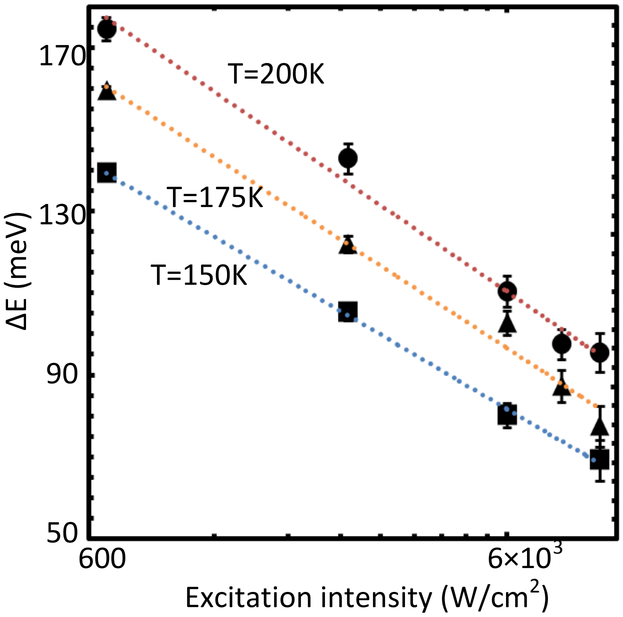

Figure 4-8: Excitation intensity dependence of the energy separation between the band edge and defect peaks in sample B at T=150K, 175K and 200K. The measurements are fit with equation 4.2. The slope of the fit is $k_BT\gamma$. The γ values for 150K, 175K and 200K are 2.0, 1.9 and 1.9 respectively

4.3. VECSEL structure grown at high temperature

New QW samples were tried at higher growth temperature (370°C) and they showed approximately 10× PL intensity increase compared to the previously grown QWs at low temperature (300°C). This improvement motivated us to try the VECSEL growth again.

The calibration procedure is the same as described in chapter 3. Figure 4.9 compares the PL emission of the new high temperature grown VECSEL sample (r2568) with the one described in chapter 3. The PL intensity has improved ~200×. The reflectivity of the VECSEL sample (r2568) confirms the highly reflective DBR and cavity resonance at 1140 nm (figure 4.10). The sample was handled with the utmost care to prevent any dust or contamination getting into its surface and mailed to our collaborators in Finland for the lasing experiment. No lasing was achieved again.

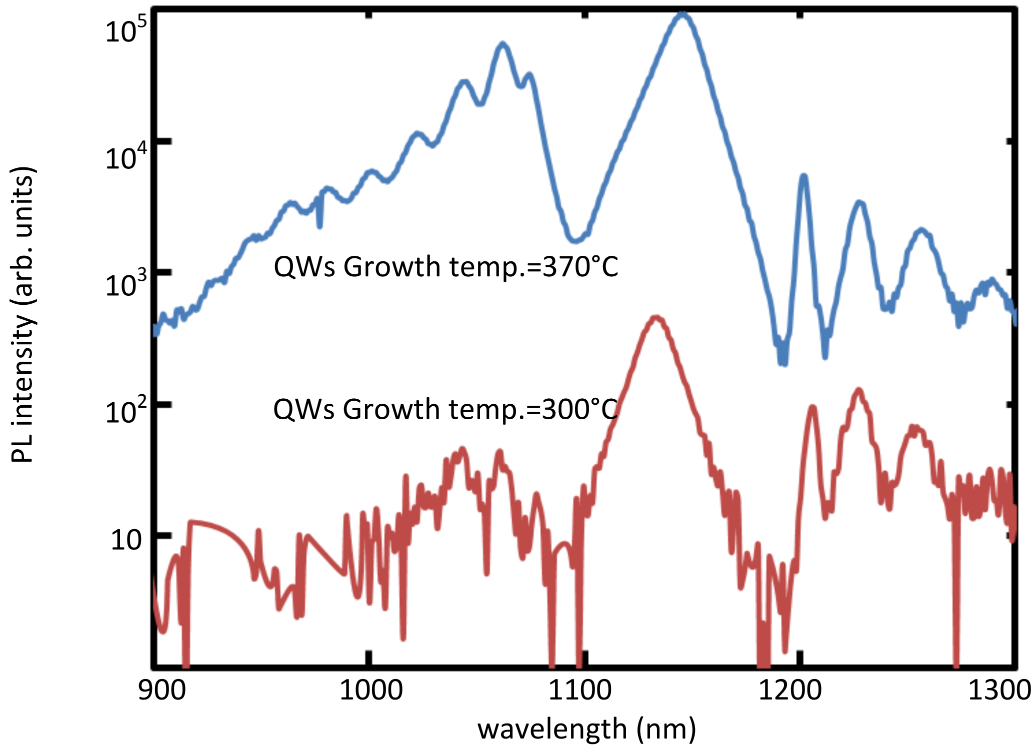

Figure 4-9: Comparison of the PL emission intensity of the new high temperature grown VECSEL sample (r2568) with the one explained in chapter 3 (r2477). The PL intensity has improved ~200× with the 370°C growth temperature.

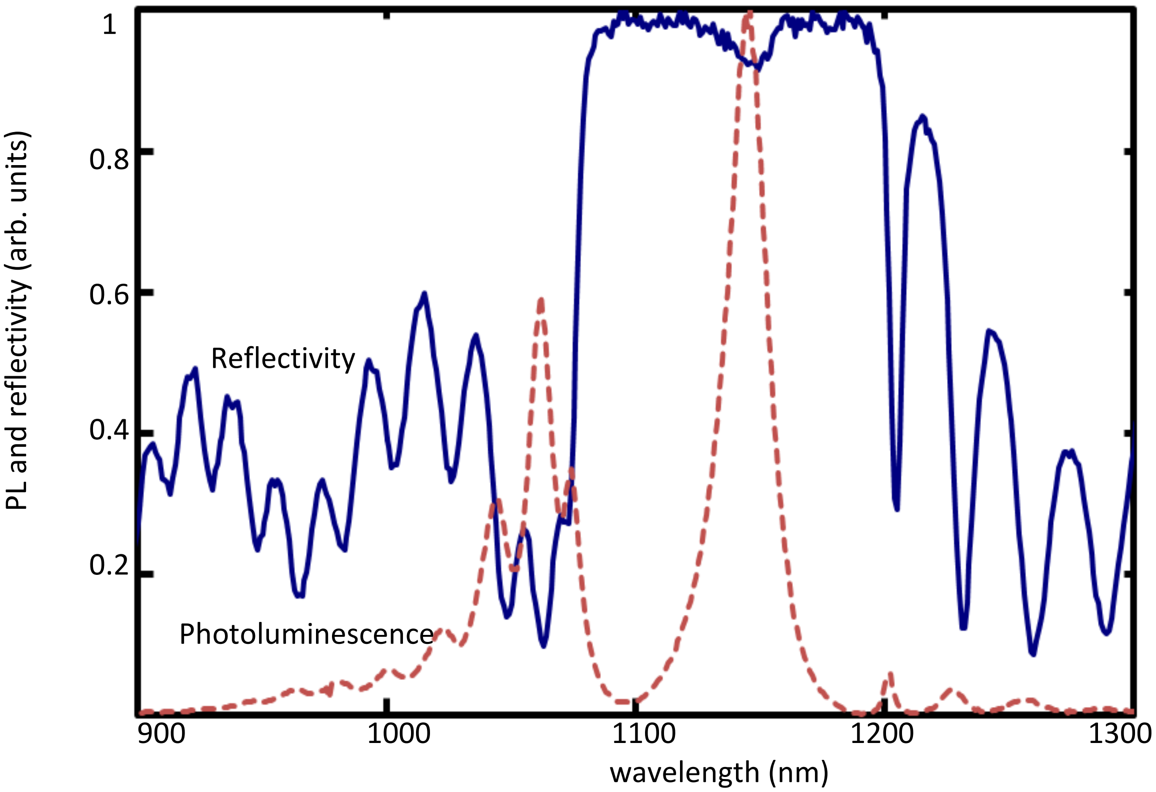

Figure 4-10: Measured reflectivity and PL spectra of the VECSEL in which the GaAsBi layers were grown at 370°C (r2568).

Scanning electron microscopy images of the sample surface and its cross-section revealed dust particles that were stuck in the epitaxialy grown material (figures 4.11 and 12). The particles should have sat on the surface during the loading of the wafer into the chamber. The DBR had grown skewed under the particles which will create scattering and non-radiative losses. In our opinion the density of these defects is too low to prevent lasing. The DBR is layered perfectly away from the defect.

A possible reason for the failure is the wide line width of GaAsBi PL emission which causes low gain across the mode bandwidth and makes the lasing threshold too large. This concluded 3 years of effort to grow a laser device and investigation of GaAsBi electronic quality by optical measurements. We asked Dr. Pat Mooney from Simon Fraser University to investigate the deep defect levels in our GaAsBi which is the topic of the next chapter.

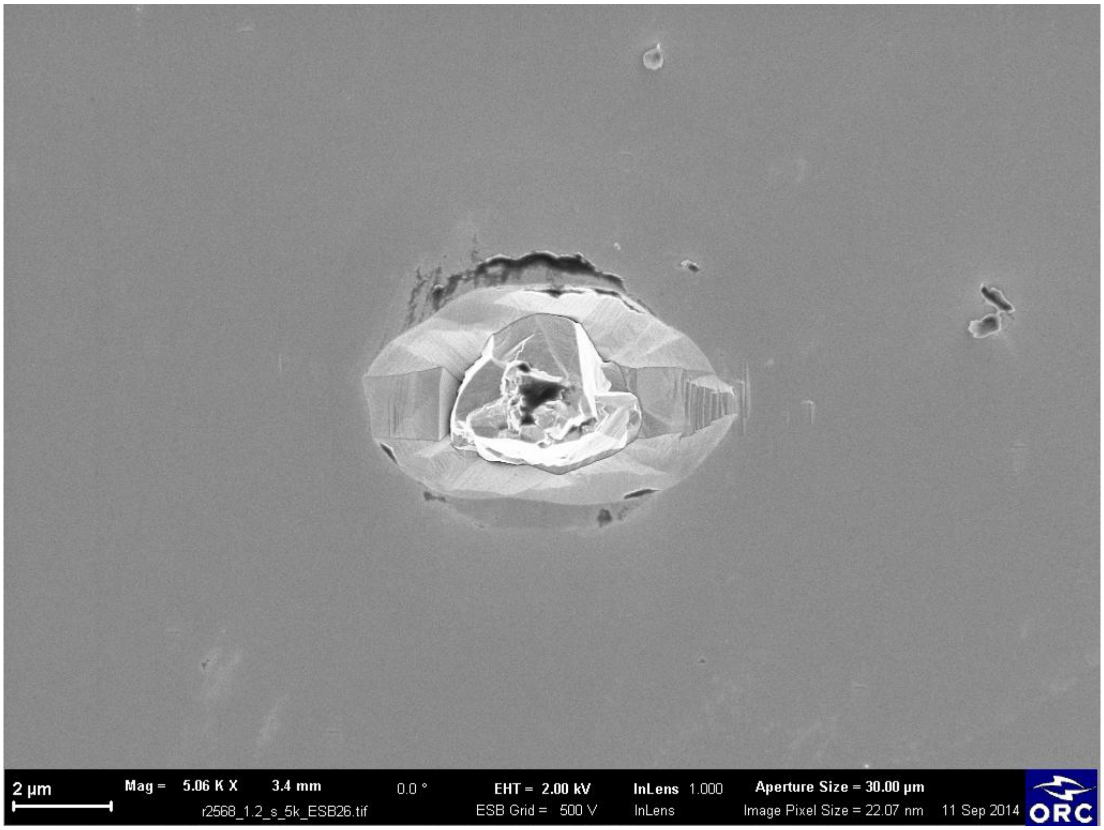

Figure 4-11: An oval defect made on the sample surface due to a dust particle. The SEM image was made by Optical Research Center at Tampere University.

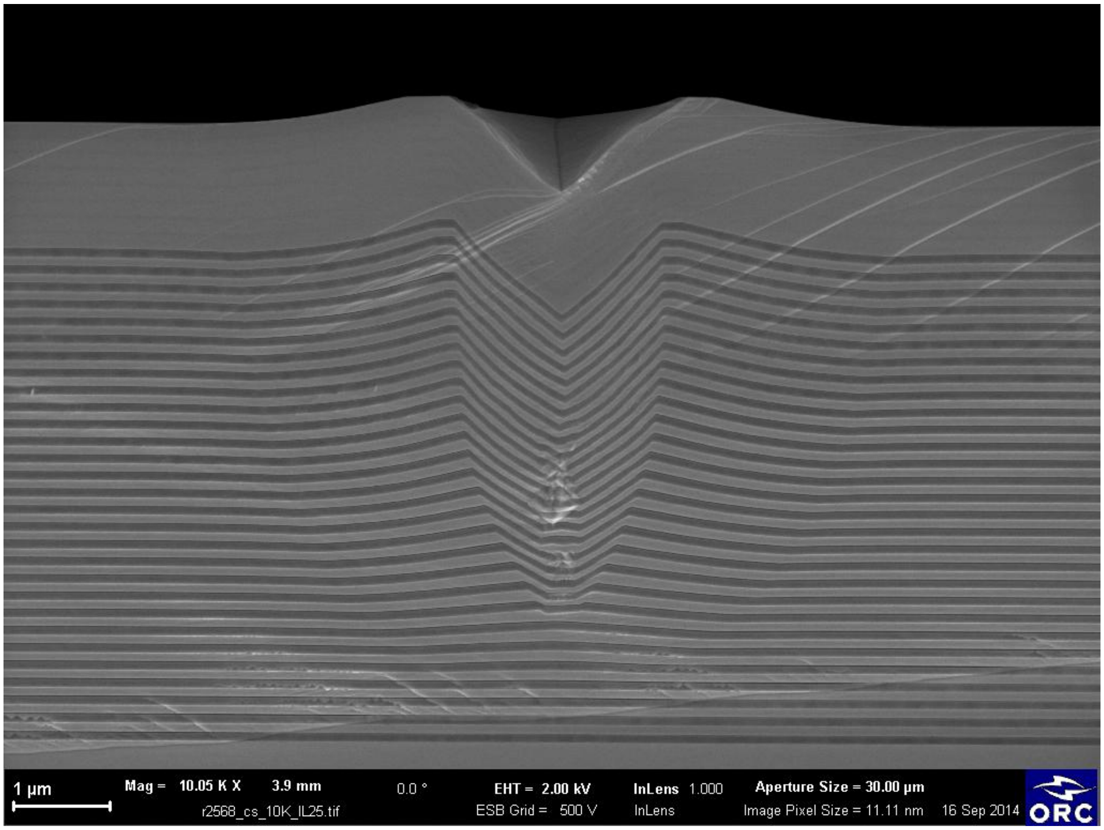

Figure 4-12: The cross section SEM image of an oval defect. The DBR grows skewed and deformed under the defect but it is layered perfectly away from the defect. The image was made by Tampere University optical group (ORC). The number of defects counted on the sample surface by an optical microscope is 64×10^4 /cm^2.

5. Deep level transient spectroscopy (DLTS) of the GaAsBi

5.1. Contributions

In order to investigate the electronic defects in GaAsBi alloys, a collaboration with Simon Fraser University was established to determine the growth temperature effect on the deep level defects concentration and energy. The calibration and growths of all the samples except one (r2482), were done by me at UVIC and all the DLTS measurements were carried out by Marianne Tarun at the University of Simon Fraser. Sample r2482 was grown by R. Lewis and its calibrations were carried out by me and M. Masnadi-Shirazi. Dr. Tiedje and Dr. Patricia Mooney supervised the project.

In the following sections there is an introduction to the doping calibration and CBr_4 doping source, then the DLTS sample structure and measurement method are described, and finally the GaAsBi deep level measurement results are discussed.

5.2. Doping calibration

The DLTS method basically measures the transient response of the depletion capacitance of a one-sided abrupt semiconductor junction diode. The semiconductor has to be doped to certain levels to make a diode suitable for measuring certain densities of defects. DLTS is sensitive to defect densities down to $\sim 10^{-4}$ times the doping concentration of the semiconductor, e.g. to measure $\sim 10^{12}$ cm^{-3} defect concentration the semiconductor doping has to be $\sim 10^{16}$ cm^{-3} or less.

Silicon and carbon are used to n and p-dope GaAs and its alloys. Silicon atoms occupy gallium sites in the GaAs lattice and give up extra electrons as donors while carbon atoms occupy arsenic sites in the lattice and cause p-doping. An effusion cell containing Si wafer pieces generates enough flux to n-dope GaAs samples in the range of 10^{17} to 2×10^{18} cm^{-3}. The p-doping is done by a CBr_4 gas source and the dopant concentration depends on the gas pressure which is controlled by a diaphragm valve. CBr_4 gas molecules break into bromine and carbon on the hot substrate surface. Bromine is pumped out of the growth chamber but carbon incorporates into the growing layer. A doped single layer grown on a semi insulating substrate is used for doping calibration. It is cut into square pieces and its doping concentration is found from van der Pauw and Hall measurements (section 2.3.4).

The doping calibrations showed that each 25 degrees increase in the silicon cell temperature doubles the n-doping in 1 µm/hr growth rate samples. Also, the relation between p-doping concentration and the CBr_4 gas pressure was found from experimental data points (figure 5.1):

$$\text{p-doping (cm}^{-3}\text{)} = -6.62\times10^{11}\times x^{2} + 9.43\times10^{14}\times x \tag{5.1}$$

The gas pressure (x) is in mTorr unit. This relation helps to estimate the needed pressure for any desired p-doping in the range of 10^{16} to 3×10^{17} cm^{-3}.

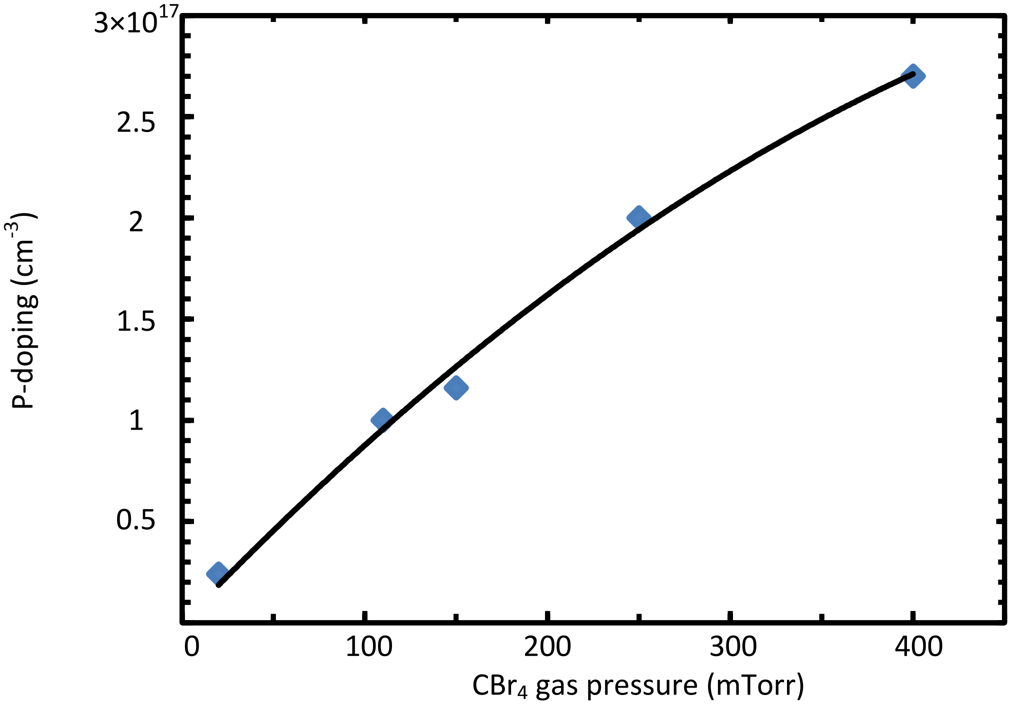

Figure 5-1: P-doping concentration as a function of CBr4 gas pressure found from Van der Pauw measurements of several calibration epi-layer samples at 1 µm/hr growth rate.

5.3. Carrier interactions with deep levels

Real semiconductors are not perfectly crystalline and periodic. They can have several types of imperfections such as impurity, interstitial, vacancy and anti-site defects. Crystal defects may cause localized states inside the bandgap which can be shallow (a few tens of meV from the band edges for GaAs) or deep (farther away from the band edges). Shallow levels are ionized at room temperature and provide the free carrier concentration while mid-gap deep levels are effective recombination centers and reduce the carrier lifetime. Non-radiative recombination at deep levels decreases photoluminescence and electroluminescence intensity. An electron or hole can have two types of interactions with a deep level: capture and emission.

Capturing a carrier is characterized by capture cross section ($\sigma_{n\ or\ p}$). The capture cross section is a property of the deep level. The capture rate of an empty state c_n (in the unit of s^{-1}), depends on the density of carriers n and mean thermal velocity $\langle v_n \rangle$ as follows: [70,71]

$$c_n = \sigma_n \langle v_n \rangle n \tag{5.2}$$

The number of carriers which are emitted per unit time from an occupied deep level is called the emission rate ($e_{n\ or\ p}$). Figure 5.2 illustrates a trap bellow the Fermi level interacting with conduction and valence bands in an n-type material. The occupancy of a deep level is determined by the relative values of the capture and emission rates. The net rate of charge transition is calculated from the total concentration of the deep level states (N_T) and the concentration of the states occupied by electrons (n_T):

$$\frac{dn_T}{dt} = \left(c_n + e_p\right)(N_T - n_T) - \left(e_n + c_p\right)n_T \tag{5.3}$$

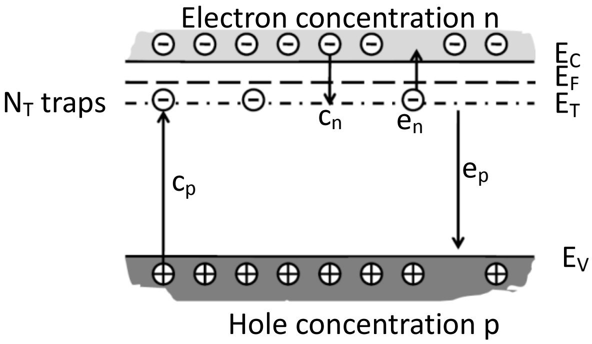

Figure 5-2: A trap with the energy smaller than Fermi level capturing and emitting carriers in an n-type material. The picture is partially copied from reference [70]. e_n, e_p, c_n and c_p are electron and hole emission and capture processes respectively.

Here $N_T - n_T$ is the concentration of empty states and N_T is assumed to be small compared to the net doping. The left side of equation 5.3 is zero at thermal equilibrium which results in the detailed balance conditions:

$$e_n n_T = c_n(N_T - n_T) \tag{5.4}$$

$$c_p n_T = e_p(N_T - n_T) \tag{5.5}$$

Therefore the occupancy of the trap states depends on the capture and emission rates of the traps:

$$\frac{n_T}{N_T} = \frac{c_n}{c_n+e_n} = \frac{e_p}{e_p+c_p} \tag{5.6}$$

The occupancy of the trap states is also described by the Fermi-Dirac distribution at equilibrium:

$$\frac{n_T}{N_T} = \frac{1}{1+\exp\left(\frac{E_T-E_F}{kT}\right)} \tag{5.7}$$

E_T and E_F are the trap and Fermi energies. If we substitute 5.2 and 5.7 into 5.6 and use the carrier concentration relation ($n = N_c \exp\left(-\frac{E_c-E_F}{kT}\right)$) to simplify the final expression, it gives us the following relation for electron emission:

$$e_n(T) = \sigma_n \langle v_n \rangle N_c \exp\left(-\frac{E_c-E_T}{kT}\right) \tag{5.8}$$

This relation is later used to find trap activation energy, which is the energy separation between the trap level and the band edges: $E_a = E_c - E_T$, when σ_n is independent of temperature.

5.4. DLTS method

The DLTS method was first patented by D. V. Lang [71]. It uses a Schottky or a one sided abrupt p/n junction diode to determine the thermal emission activation energy, capture cross section and concentration of deep level defects (far in energy from band edge). DLTS is sensitive to defect densities, ~10^{-4} times the doping concentration of the semiconductor, e.g. ~10^{12} cm^{-3} when the semiconductor doping is 10^{16} cm^{-3}. Figure 5.3 illustrates the DLTS measurement principle for an n-type Schottky diode. The defect states below the Fermi level trap electrons and are filled with electrons at zero bias. When a reverse bias is applied to the junction the depletion width is increased and the defect (trap) states close to the junction are pushed up above the equilibrium Fermi level and emit their electrons into the conduction band [70,71].

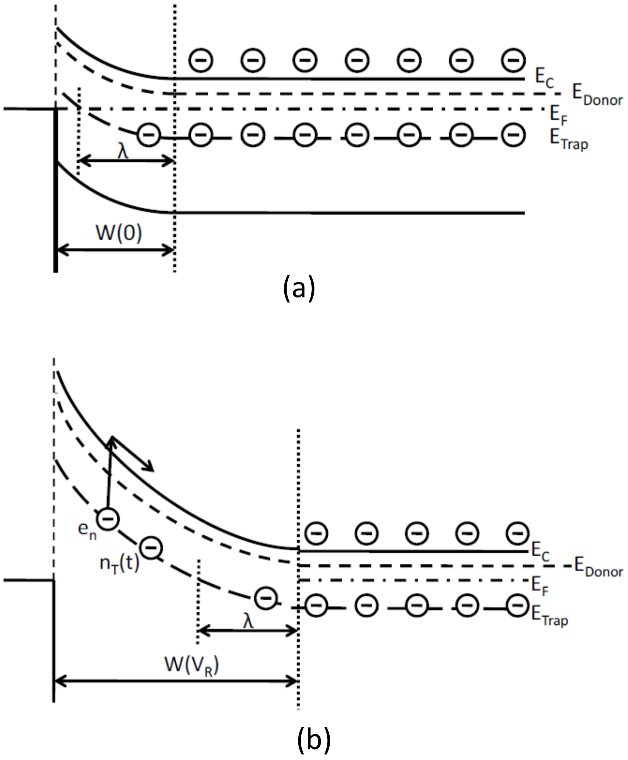

Figure 5-3: A Schottky junction at (a) zero bias and (b) reverse bias (V_R). The arrows show the electron emission from the trap level to the conduction band. The figure was copied from reference [72].

The capacitance across the junction depends on the depletion width. In the DLTS method, a reverse bias (V_R) maintains the steady state depletion width and short positive voltage pulses reduce the depletion width and cause the trap states to be filled. The transient capacitance following the short filling pulse has an exponential dependence on time as electrons are emitted into the conduction band (e_n) [70]:

$$\Delta C(t) = \Delta C_0 \times e^{-e_n t} \tag{5.9}$$

Where $$\Delta C_0 = \Delta C(t=0) = \frac{-1}{2}\left\{\frac{(W(V_R)-\lambda)^2-(W(0)-\lambda)^2}{W^2(V_R)}\right\}\frac{N_T}{N_d}C(V_R) \tag{5.10}$$

is the capacitance difference between t=0 and the steady state value. $W(V_R)$ and $W(0)$ are the depletion widths at reverse (V_R) and zero biases. N_T and N_d are the trap and donor (n-doping) densities. λ is the distance within the depletion region where the traps do not emit electrons to the conduction band because the trap energy level (E_{Trap}) lies above the Fermi energy (E_F).

The temperature dependence of the carrier emission rate (equation 5.8) combined with a "rate window" are used to determine emission rate from the transient capacitance [71]. As is illustrated in figure 5.4, the transient capacitance is sampled at times t_1 and t_2 after the positive voltage pulses. S(T) is the capacitance difference at t_1 and t_2 , which is temperature dependent because it is a function of emission rate. The capacitance difference has a peak whenever the rate window matches the emission rate of a deep level. The capacitance difference as a function of temperature is known as the DLTS signal or spectrum.

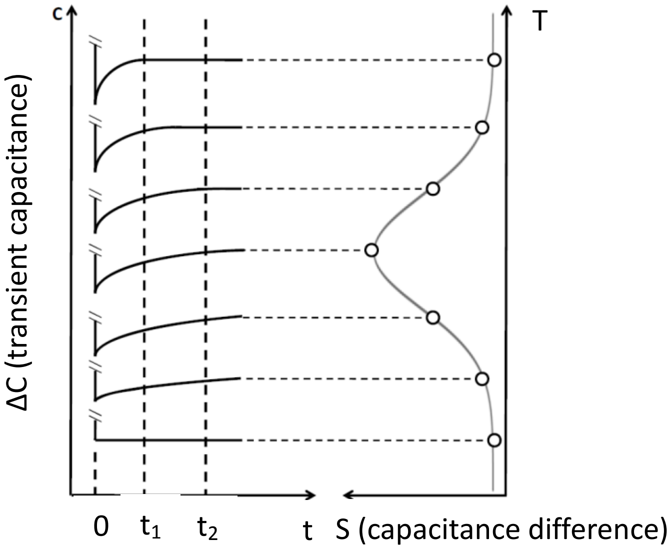

Figure 5-4: Transient and difference capacitance when the measurement temperature is swept. t=0 is at the end of filling pulse [Adapted from reference 71]. The right side curve is a DLTS signal.

From equation 5.9:

$$S(T) = g\Delta C_0\{e^{-e_n t_1} - e^{-e_n t_2}\} \tag{5.11}$$

Where g is a calibration factor taking account the system gain.

If the derivative of equation 5.11 with the respect to τ ($\tau = 1/e_n$) is equated to zero, the emission rate at maximum $S(T)$ is found to be:

$$e_n(T_m) = \frac{\ln(t_2/t_1)}{t_2 - t_1} = 1/\tau_{ref}(T_m) \tag{5.12}$$

$1/\tau_{ref}$ is the instrument rate window which is equal to the trap emission rate at the DLTS signal maximum. The sampling time dependence of the instrument rate window means that the DLTS peak position (T_m) varies for different rate windows.

Thermal velocity and density of states depend on temperature with 3/2 and 1/2 powers. If we take out all the temperature dependencies to one side of the equation 5.8 it can be rearranged in the following form (Arrhenius form):

$$\ln\left(\frac{e_n}{T^2}\right) = \ln(\gamma\sigma_n) - \frac{E_A}{k_B}\frac{1}{T} \tag{5.13}$$

$\gamma = 2\sqrt{3}M_C(2\pi)^{3/2}k^2 m_e^* h^{-3}$ is a constant. M_C, m_e^* and h are the number of conduction band minima, electron effective mass and Planck constant. e_n is the spectrometer's rate window which is varied over a range of values and then $\ln\left(\frac{e_n}{T^2}\right)$ is plotted as a function of $\frac{1}{T}$ and the activation energy is calculated from its slope and the capture cross section is found from the intercept with the vertical axis.

The peak height of the DLTS signal is proportional to ΔC_0 (equation 5.10). The trap concentration, N_T, is calculated from the magnitude of the DLTS peak, ΔC, with the relation:

$$N_T = 6N_a \left|\frac{\Delta C}{C(V_R)}\right| \left\{\frac{W^2(V_R)}{(W(V_R)-\lambda)^2 - (W(V_P)-\lambda)^2}\right\} \tag{5.14}$$

The trap concentration for a measured capacitance difference is obtained when the filling pulses are long enough for all the traps to be filled. Figure 5.5 shows the block diagram of the SULA deep level spectrometer which was used for the measurements at Simon Fraser University. The sample was cooled inside a liquid Nitrogen cryostat and the measurements were carried out from 78K to 500K. The time window of the measurement (t_2 and t_1) is set by a delay time after the filling pulse (initial delay, ID).

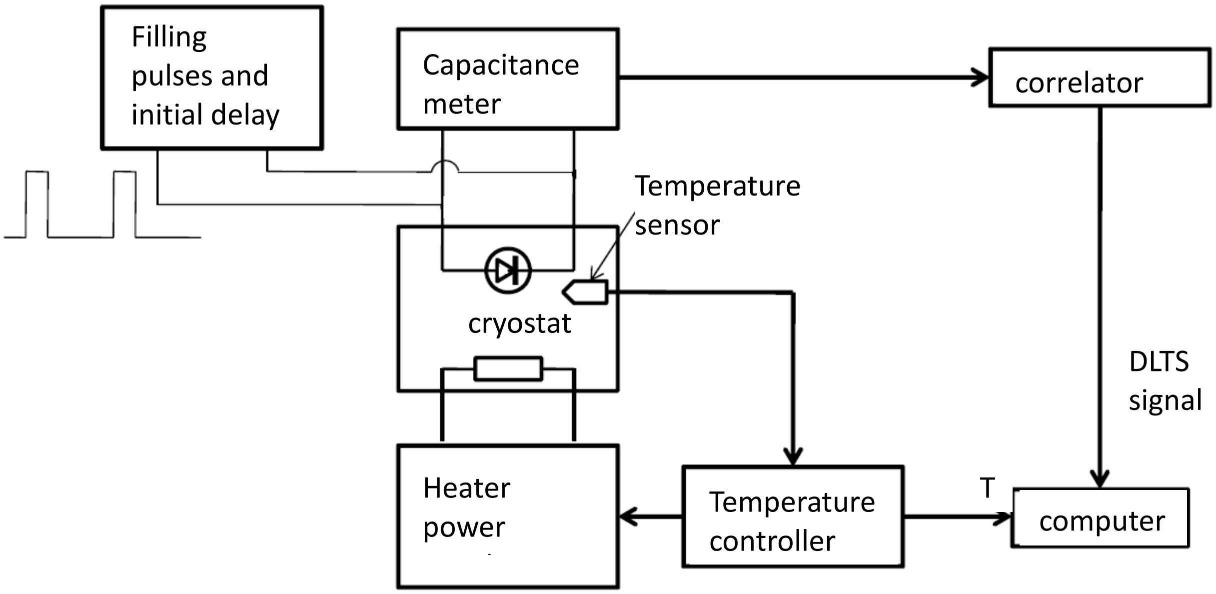

Figure 5-5: Block diagram of the SULA deep level spectrometer. The figure was partially taken from [70].

5.5. DLTS sample structure

A Schottky or a one sided abrupt p/n junction diode consists of several layers. Figure 5.6 illustrates a schematic of a GaAsBi one sided abrupt p/n junction diode diode which is used for DLTS measurements. The structure is grown on a n+GaAs substrate with 2-5×10^{18} cm^{-3} doping concentration. More than 100 nm of n+GaAs buffer layer smooths the surface for the diode growth. Then the substrate temperature is lowered and the Ga:As 1:1 ratio is found and the arsenic valve is set to the desired values for GaAsBi growth. Whenever a shutter is opened the growing surface goes through a transient phase until the cell flux becomes stable hence the number of shutter changes has to be minimized when the junction is grown. The Bismuth cell and CBr_4 source are opened long before the junction is grown in order to be stabilized and 116 nm of n+GaAsBi is grown. It has to be noted that the p-doping level is less than 2×10^{17} cm^{-3} so having the CBr_4 and silicon cell open simultaneously still results in n+ doping. The silicon shutter is closed at the junction and causes an abrupt change from 5×10^{18} cm^{-3} n-doping to 1-2×10^{17} cm^{-3} p-doping. More than 500 nm of p-GaAsBi is grown which is the region of interest with the required band bending for the DLTS measurement. The p-doped layer is capped with a 300-400 nm p+ layer which guarantees an ohmic contact on the top of the sample. Ti/Pt/Au and AuGe/Ni/Au contacts are evaporated by electron-beam evaporator on the top and back side of the sample.

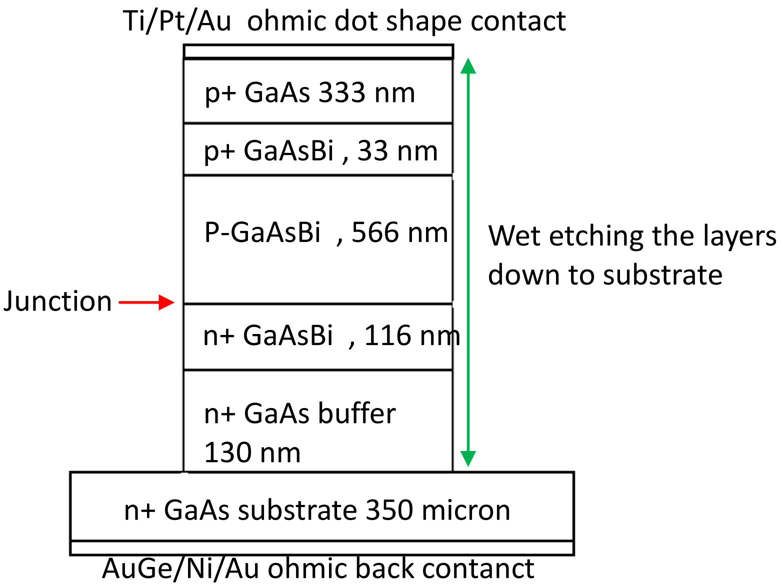

Figure 5-6: Schematic of an n+/p diode which is used for DLTS measurement.

The top contact is designed to be circle shape with 400µm diameter. The diode layers are etched down to the substrate by Piranha wet etching to define the junction area. The etchant solution is $H_2SO_4/H_2O_2/H_2O$ with 4:1:5 proportionalities that cannot affect gold contact but etches GaAs with 83 nm/sec speed at 21ºC. Figure 5.7 shows the effect of the etching on a DLTS diode device. The top gold remains intact.

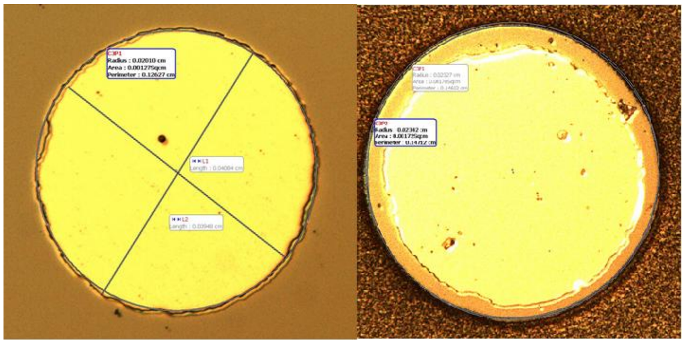

(a) (b)

Figure 5-7: The circular top contact of a DLTS diode device (a) before and (b) after Piranha etching under optical microscope. The etching has not changed the top gold contact. The image was made at Simon Fraser University.

5.6. DLTS measurement results

Seven of the DLTS samples were chosen to present the DLTS results. The sample composition and growth conditions are listed in table 5.1 and they are labeled with the letters A-G. Samples A and B are both GaAs n+/p diodes grown at high temperature (570ºC) with two different CBr_4 gas pressure of 100 and 20 mTorr. Samples C-G were grown at the substrate temperatures of 330 and 370ºC with the arsenic pressure set to a value near the stoichiometric surface condition to incorporate Bi and to avoid the formation of metal droplets on the growth surface. It has to be noted that sample D is different from the other samples as its p+GaAs cap layer was grown at 400 ºC, a higher temperature than the growth temperature of its GaAsBi layer. We come back to this difference later when discussing the traps in samples D and E.

Table 5-1: The DLTS samples (n+/p abrupt junction diodes) composition and growth conditions. The Bi contents were inferred from (004) x-ray scan simulation.

Sample #	[Bi]%	Growth temp. (ºC)	As_2:Ga (BEP) ratio	doping of p-GaAsBi layer from C-V curves (cm^{-3})	Contact anneal
A (r2590)	0	570	6	1.0×10^{17}	No
B (r2592)	0	570	7.3	2.4×10^{16}	No
C (r2614)	0	330	3.1	1.0×10^{17}	No
D (r2482)	0.68	330	3.03	1.1×10^{17}	450 ºC for 30s
E (r2613)	0.84	330	2.9	1.3×10^{17}	No
F (r2609)	0.82	370	3.6	2.5×10^{17}	No
G (r2552)	0.92	370	3.1	4.0×10^{17}	450 ºC for 30s

The diode devices were prepared with the procedure explained in section 5.5 and mailed to Simon Fraser University for DLTS measurements. The reverse bias leakage current of the diodes has to be less than 10^{-4}A in order for the capacitance meter of the DLTS spectrometer to function. However, a much lower reverse leakage current is important in order to obtain an accurate measurement of the trap concentration to obtain trustable DLTS data. The I-V curve of a sample helps to find the leakage current and confirm the diode structure. The capacitance of a Schottky diode or a one-sided p/n junction can be rearranged as a function of reverse bias (equation 5.15). The C-V characteristic is useful to determine the doping level (N_a) of the p-GaAsBi layer (low doped region in figure 5.6) [70]:

$$\left(\frac{1}{C}\right)^2 = \frac{2(V_{bi}+V_R)}{e\epsilon N_a} \tag{5.15}$$

ϵ and V_{bi} are the GaAs permittivity and the diode's barrier voltage. Figure 5.8 shows the I-V and C-V characteristics of n+/p abrupt junction diodes grown at 570ºC (samples A and B) which are the reference GaAs samples. Both samples have nice diode characteristic with ~1.47 V barrier voltage. They both meet the criteria of DLTS maximum acceptable leakage current, 10^{-4}A at -2 V reverse bias. The inferred values of the p-doping show sample A to be 5× more heavily p-doped than sample B.

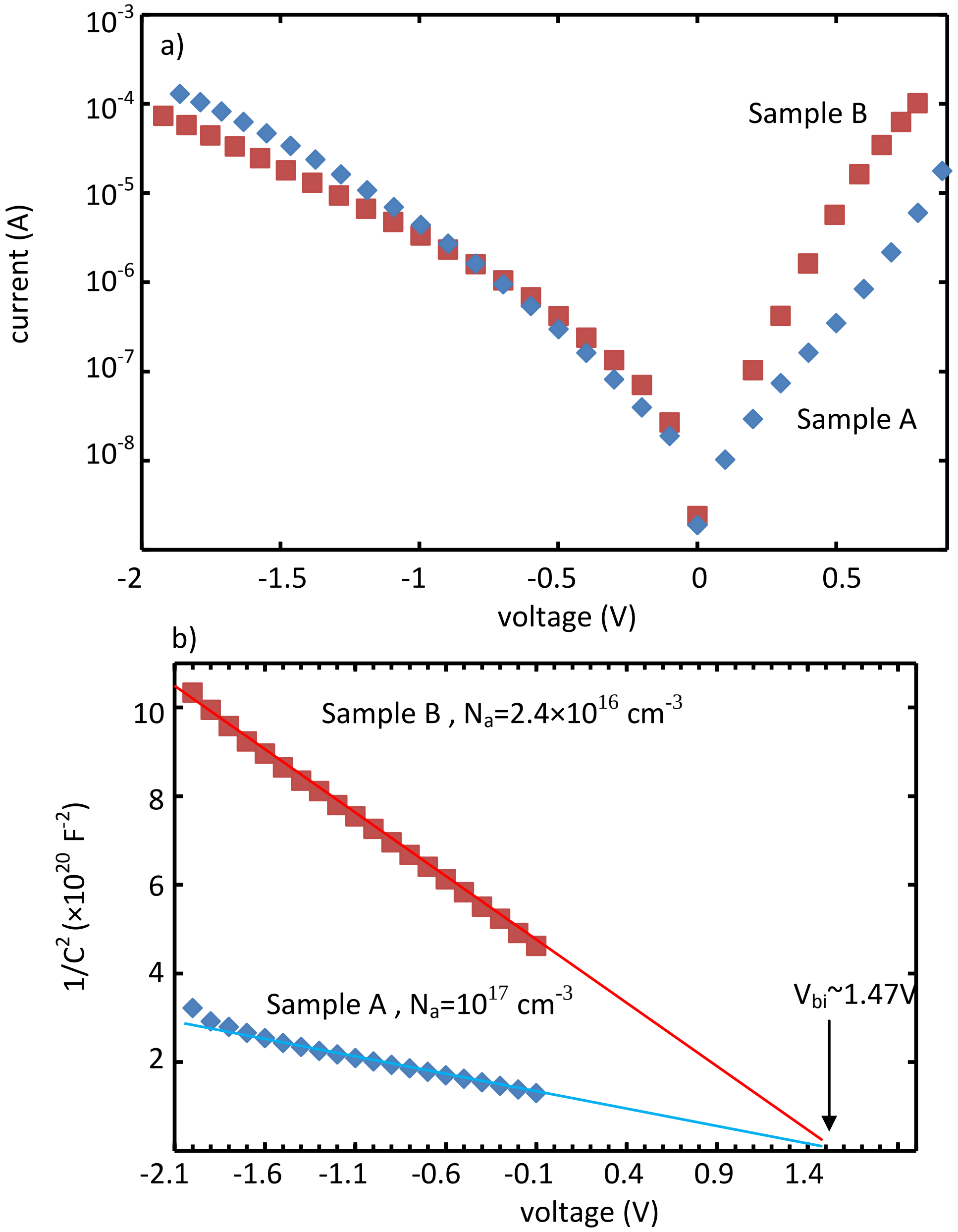

Figure 5-8: Samples A and B are GaAs n+/p diodes grown at 570ºC with CBr4 gas pressure of 100 and 20 mTorr a) I-V curves of the samples. b) C-V curves. The measurements and fits were done by Marianne Tarun at SFU. The dopant concentrations are inferred from equation 5.15.

Samples A and B DLTS signals were measured at -1V reverse bias and 2ms spectrometer initial delay (equal to 116 s^{-1} rate window). The DLTS spectra are shown in figure 5.9. Both curves have only one hole trap peak at ~305 K. The trap concentrations, N_T, were calculated from the magnitude of the DLTS peak, ΔC, with the equation 5.14 and are almost the same value for both samples ~7.5×10^{14} cm^{-3}.

The thermal emission energy (E_A) and capture cross section for each deep level defect were determined from the slope and intercept of Arrhenius plots of T^2/e_p vs. $1000/T$, as described in equation 5.13 where e_p is the spectrometer rate window. The Arrhenius plot for each trap was obtained from a series of DLTS spectra taken at different rate windows ranging from 4.65 to 4.65×10^3 s^{-1} and they are shown in figure 5.10. The samples A and B trap parameters are listed in table 5.2. They both have the same emission activation energy of ~0.55 eV which is the same as that of the Fe acceptor level in p-GaAs [73]. This activation energy is close to the single donor level of the $As_{Ga}^{-}As_{i}$ complex, also known as EL2 [76]; but EL2 was not observed in n-GaAs grown at standard conditions [35] and therefore the hole trap in samples A and B can only be Fe impurity.

The Fe impurity source is not from contact annealing as the annealed and non-annealed pieces of sample A showed identical DLTS signal. It is not from mesa etching either because using semiconductor grade acid for etching did not change the DLTS signal of the samples. We concluded that the Fe impurity has to be introduced during the growth process most likely from CBr_4 or arsenic source. The Fe trap concentration is the same in both samples A and B whereas the p-doping of A is 5 times that of B; hence the source of the Fe impurity is not the CBr_4 doping source. Based on trace contamination information obtained from United Mineral and Chemical corp. (UMC), our arsenic source material has 9 ppb (or 4.5×10^{14} cm^{-3}) Fe concentration which is of the same order of magnitude as the Fe trap concentration in the samples A and B (7.5×10^{14} cm^{-3}). Therefore arsenic is the most likely Fe impurity source in our MBE system.

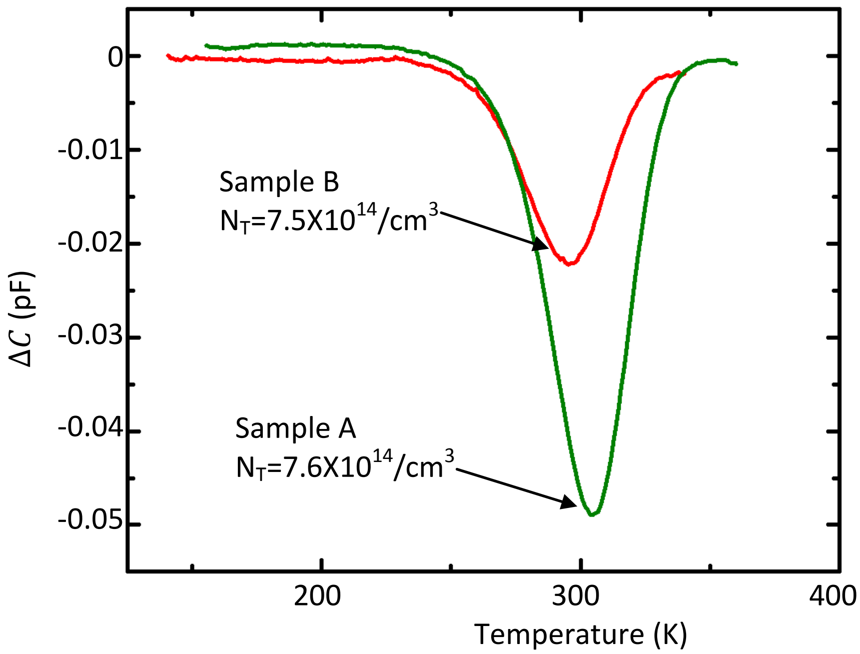

Figure 5-9: Differential transient capacitance as a function measurement temperature for GaAs n+/p abrupt junction diodes grown at 570ºC (samples A and B with CBr4 gas pressure of 100 and 20 mTorr). The trap density is the same for both samples. The measurement was done at -1V reverse bias and 2ms delay time. (SFU lab results)

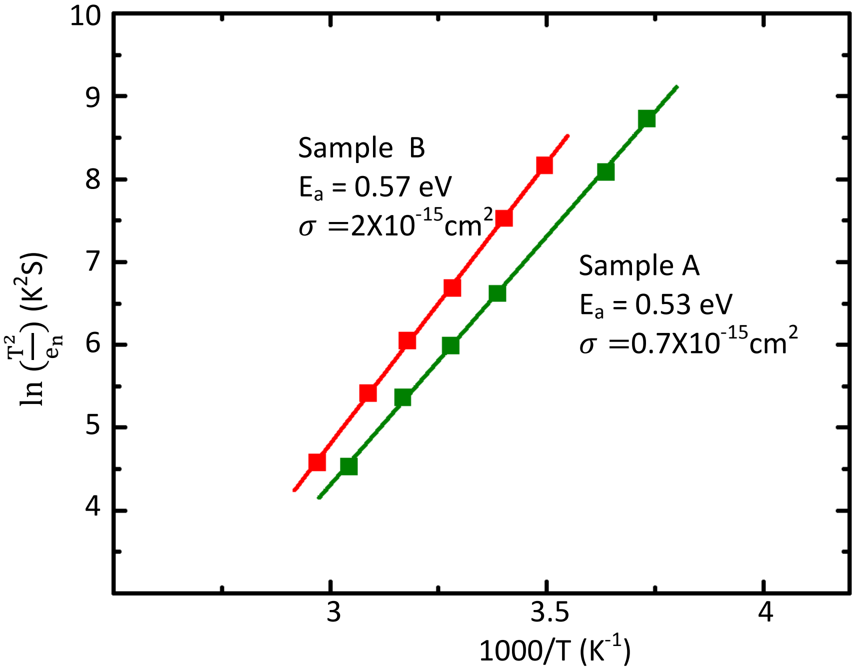

Figure 5-10: Arrhenius plot for the two trap peaks shown in figure 5.9 for GaAs n+/p diodes A and B. The activation energy of the peaks is (0.55±0.02) eV the same as for the Fe impurity. (SFU lab measurements)

Figure 5.11 shows the DLTS signal and Arrhenius plots for the n+/p GaAs grown at 330°C (sample C). Sample C trap parameters are compared to the Fe impurity trap in the standard grown samples (A and B) in table 5.2. Sample C was grown with an As_2/Ga ratio close to stoichiometric similar to the ratio used for growing GaAsBi layers. The DLTS signal indicates the presence of four DLTS peaks and the total trap concentration is 40 times larger than the trap concentration of the standard grown samples A and B. When trap H(0.6) of sample C is compared to the Fe trap of sample A on the Arrhenius plot, it is clear that they overlap with each other confirming that they are the same trap and the magnitude of the trap concentration is 3 times larger in sample C. The uncertainty in the trap activation energy is ±0.03, which is a typical uncertainty for measuring thermal emission energy by the DLTS method.

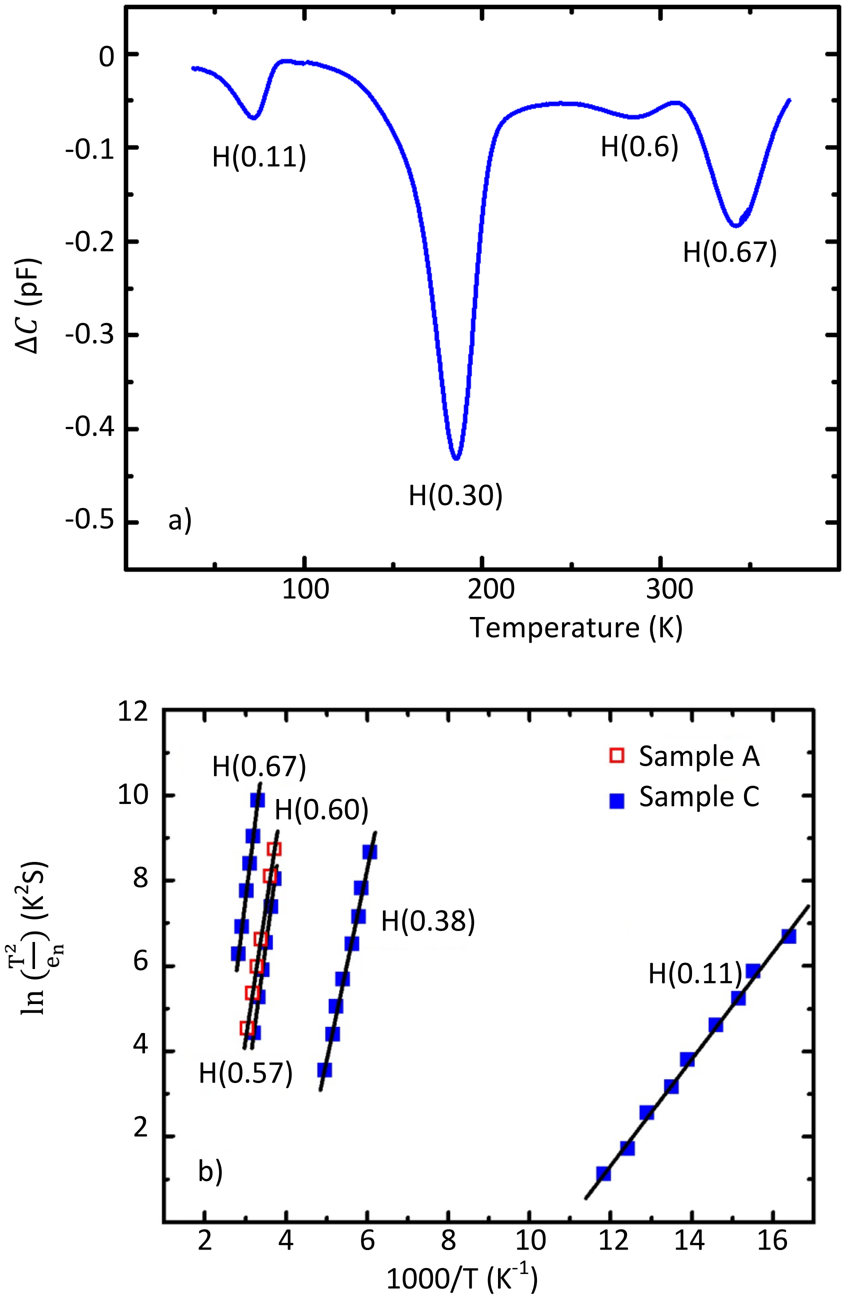

Figure 5-11: a) DLTS signal of the GaAs n+/p diode grown at 330ºC, sample C (r2614). b) Arrhenius plots for the trap peaks shown in (a) compared with sample A's Fe impurity trap. The DLTS peaks and corresponding Arrhenius plots are labeled by the trap activation energy. (SFU lab measurement)

Table 5-2: Hole traps in n+/p GaAs grown at 570 ºC and 330 ºC. The uncertainty in EA is ±0.03 eV and in σ it is about an order of magnitude.

Sample	**Hole Trap Parameters**			**Fe**	
A GaAs 570 ºC	E_A (eV) σ (cm^2) N_T (cm^{-3})			0.53 7e-14 7.6e14	
B GaAs 570 ºC	E_A (eV) σ (cm^2) N_T (cm^{-3})			0.57 2e-15 7.5e14	
C GaAs 330 ºC	E_A (eV) σ (cm^2) N_T (cm^{-3})	0.11 5e-16 9.0e14	0.38 6e-14 1.5e16	0.60 4e-14 2.4e15	0.67 6e-15 8.3e15

Figure 5.12 shows the DLTS signal and Arrhenius plots of two n+/p GaAsBi diodes (D and E) grown at 330ºC substrate temperature with As_2/Ga BEP ratio close to the stoichiometric surface condition. The Bi content of the samples was inferred from the simulation of the 004 x-ray scans and it is similar for both samples 0.68% and 0.84%. The DLTS signals are very different for these two samples with stronger carrier freeze-out in sample E at low temperature. The traps parameters of samples D and E are listed in table 5.3 and show that the total hole trap concentration is almost the same for both samples $\sim 3\text{-}5\times10^{16}$ cm^{-3} , and similar to the total trap concentration in sample C, the 330 ºC grown n+/p GaAs. The traps labeled H4 in the table 5.3 are from the same defect since their Arrhenius curves overlap however the concentration of this trap is 3× larger in sample D than sample E. The traps labeled H3 in table 5.3 have similar activation energies, 0.48 and 0.53 eV, but their capture cross sections are different by a factor of 1000 and their Arrhenius curves are displaced, therefore they do not originate from the same defect. The traps labeled H2 in the table have displaced Arrhenius curves and they are not from the same defect although their activation energies and capture cross section are reasonably close. The trap with 0.74 eV activation energy (H1 in table 5.3) appears to be present in both samples D and E but its parameters were measurable only in sample E because sample D's reverse bias leakage current was too large at above ~450K for DLTS

measurement. As noted earlier, sample D’s p+GaAs layer was grown at 400 ºC while the layer was grown at 330°C in sample E. Therefore sample D’s GaAsBi was effectively annealed for 30 min at 400 ºC during the p+GaAs growth which may explain the traps are different in samples D and E. As well, sample D had a contact anneal at 450 ºC for 30 s which is likely a minor issue and unlikely to change the spectrum as much as the 30 min cap layer growth.

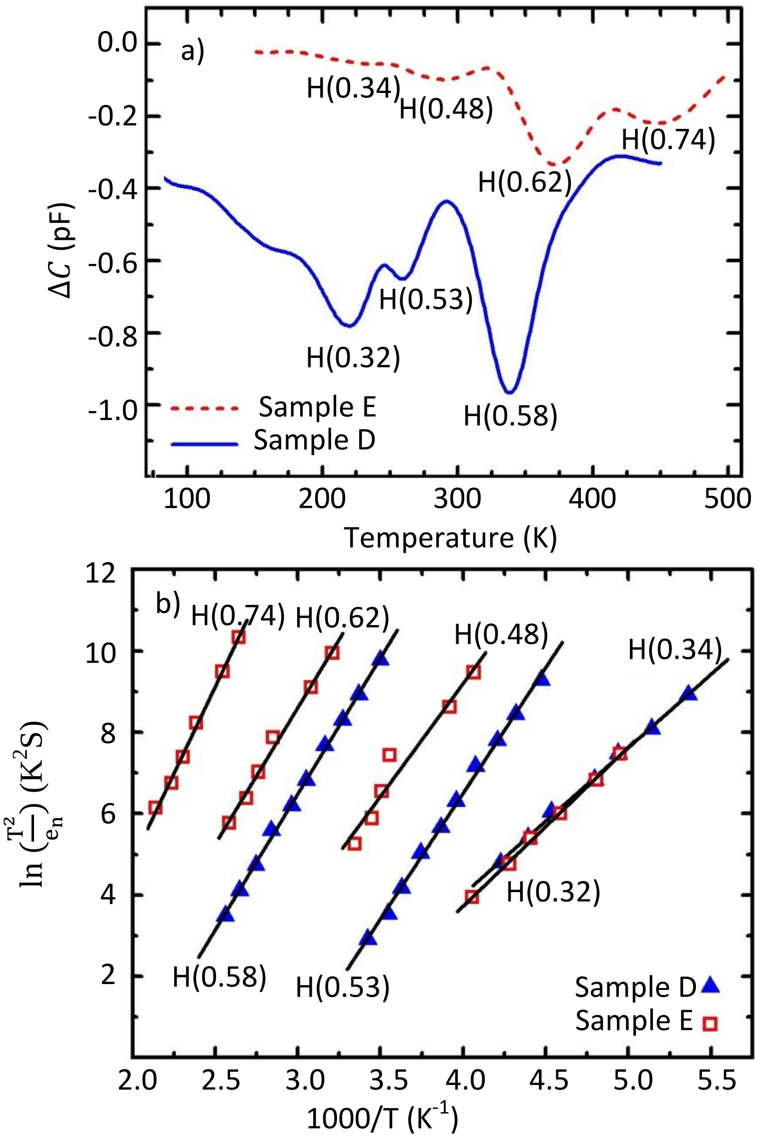

Figure 5-12: a) DLTS signals of two GaAsBi n+/p diodes grown at 330ºC, sample D and E (r2482 and r2613). b) Arrhenius plots for the trap peaks shown in (a). The DLTS peaks and corresponding Arrhenius plots are labeled by the trap activation energy. (SFU lab measurement)

Table 5-3: Hole traps in dilute GaAsBi grown at 330ºC. The uncertainty in E_A is ±0.03 eV and in σ it is about an order of magnitude. The scatter in N_T among devices measured on the same sample is typically about a factor of 2. The column labels H1 to H4 are useful for discussions of the traps observed in the various samples.

Sample	**Hole Trap Parameters**	**H4**	**H3**	**H2**	**H1**
D GaAsBi 0.68% 330 ºC	E_A (eV) σ (cm^2) N_T (cm^{-3})	0.32 8e-16 1.3e16	0.53 1e-14 1.2e16	0.58 1e-16 2.9e16	--- --- ~3e15
E GaAsBi 0.84% 330 ºC	E_A (eV) σ (cm^2) N_T (cm^{-3})	0.34 9e-17 4.8e15	0.48 9e-17 4.8e15	0.62 2e-16 1.1e16	0.74 1e-16 8.6e15

Samples F and G were grown with similar growth conditions at 370ºC substrate temperature with As_2/Ga ratio close to the stoichiometric surface condition. They have similar Bi incorporation, 0.8% and 0.9%. The DLTS signal and Arrhenius plots of samples F and G are shown in figure 5.13 and their traps parameters are listed in table 5.4. The DLTS signals for samples F and G show three hole traps with total trap concentration of 4×10^{15} cm^{-3} , which is 10 times smaller than the total trap concentration for the 330 ºC grown GaAs and GaAsBi samples. The trap labeled H3 (0.49 eV) in table 5.4 is not well resolved in sample G's DLTS signal, but it seems to appear in both samples F and G. Trap H4 is from the same defect in both samples since their Arrhenius curves overlap and the trap parameters are very similar in the samples. Trap H5 is not from the same defect in the two samples as the parameters are vastly different. Sample G had a 30s contact anneal at 450 ºC which could affect the defects and may be responsible for the differences in the traps parameters.

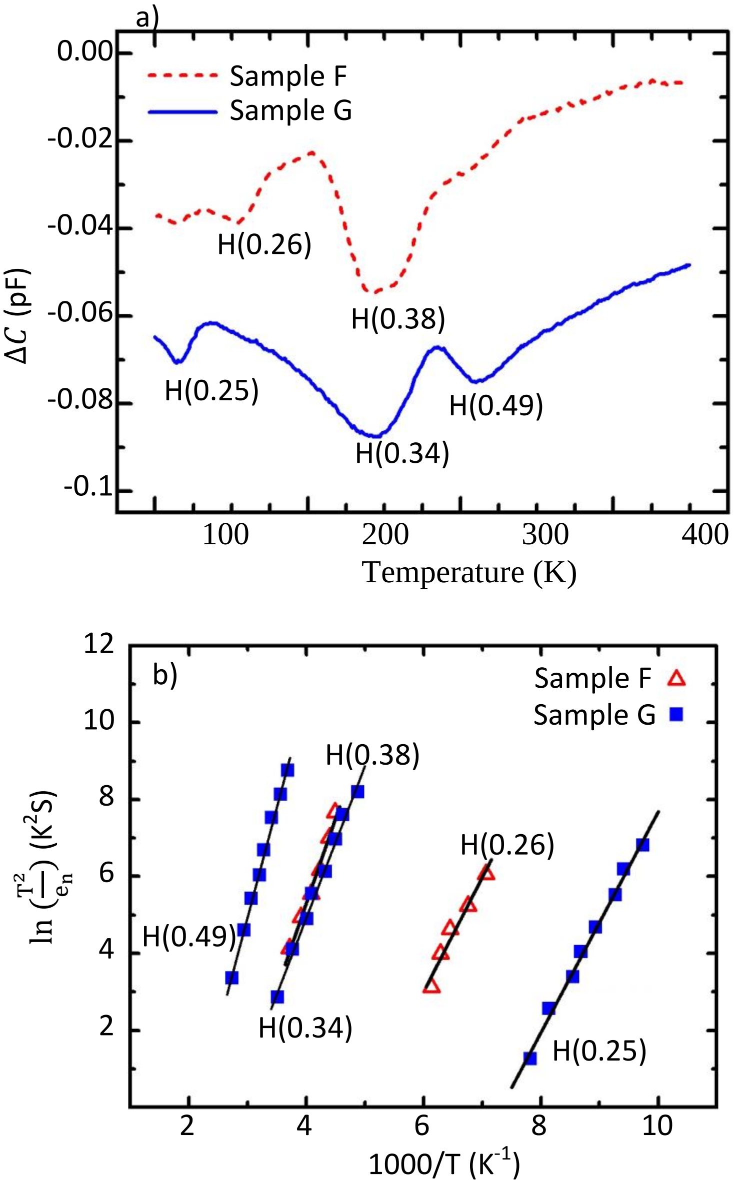

Figure 5-13: a) DLTS signals of two GaAsBi n+/p diodes grown at 370ºC, sample F and G (r2609 and r2552). b) Arrhenius plots for the trap peaks shown in figure (a). The DLTS peaks and corresponding Arrhenius plots are labeled by the trap activation energy. (SFU lab measurement)

Table 5-4: Hole traps in dilute GaAsBi grown at 370ºC. The typical uncertainty in E_A is ±0.03 eV and in σ it is about an order of magnitude. The scatter in N_T among devices measured on the same sample is typically about a factor of 2. The labels H3 to H5 are useful for comparing the traps observed in the various samples.

Sample	**Hole Trap Parameters**	**H5**	**H4**	**H3**
F GaAsBi 0.82% 370 ºC	E_A (eV) σ (cm^2) N_T (cm^{-3})	0.26 2e-15 1.3e15	0.38 1e-16 1.6e15	--- --- ~1e15
G GaAsBi 0.92% 370 ºC	E_A (eV) σ (cm^2) N_T (cm^{-3})	0.25 8e-13 3.8e14	0.34 1e-17 2.0e15	0.49 5e-17 1.2e15

5.7. Discussion

Samples E and F are GaAsBi n+/p diodes made with the same growth conditions and preparation steps except for the substrate temperatures. They have two similar traps, H3 and H4 (tables 5.3 and 5.4) with 0.49 and 0.36 eV activation energies. The trap concentration is smaller in the 370ºC grown sample by a factor of ~3 and ~5 respectively but E and F's most significant difference is the absence of H1 and H2 traps in sample F, which have the largest activation energy and concentrations in the 330ºC grown sample. E and F's total trap concentration are compared to the PL intensity of GaAsBi layers grown at different temperatures in figure 5.14. The PL data points are from the samples discussed in section 4.2.1. The trap concentration increases 10 times with 40º reduction in growth temperature while PL intensity decreases by a factor of ~40. A lower PL intensity would be expected with a larger density of deep levels. Clearly the PL intensity and trap density show a consistent trend with growth temperature.

The two GaAs and GaAsBi n+/p diodes grown at 330 ºC with similar preparation steps (C and E) have no traps with both activation energy and carrier cross section similar within the measurement uncertainty. Therefore, although C and E have comparable total trap concentration, about 2.8×10^{16} cm^{-3}, the incorporation of Bi has indeed modified the traps either chemically through Bi clustering and bandgap reduction or by strain effects. The bandgap reduction with [Bi]=0.8% incorporation is 0.07 eV which mostly shifts the valence band upward hence the traps activation energies in GaAsBi are expected to be reduced compared to their GaAs values with this shift. If sample C‘s three highest concentration traps are shifted down 0.07 eV, the obtained activation energies are 0.60 eV, 0.52 eV and 0.31 eV. These values are reasonably close to the three highest concentration traps in sample E, 0.62 eV, 0.48 eV and 0.34 eV, therefore trap H3 in sample E may be the Fe impurity level. The capture cross sections of all the traps in the GaAsBi sample are significantly smaller. We cannot say definitely whether the traps in the low temperature grown GaAsBi are due to the native defects present in low temperature GaAs, or whether they are associated with Bi incorporation.

Fuyuki et al. reported DLTS results for two Schottky GaAsBi diodes grown at 370 ºC [77]. Their DLTS spectra show a single broad DLTS peak for [Bi]=1.2 and 3.4% content samples. The difference between the hole trap activation energy in the two samples was equal to the reduction in the bandgap energy. The total trap concentration in their GaAsBi samples is similar to the samples F and G’s trap concentrations, grown at 370 ºC, but our measurements revealed several peaks (traps) in the DLTS spectra. It is not clear if the difference in the spectra is due to the difference in the Bi content or differences in the growth conditions of the samples.

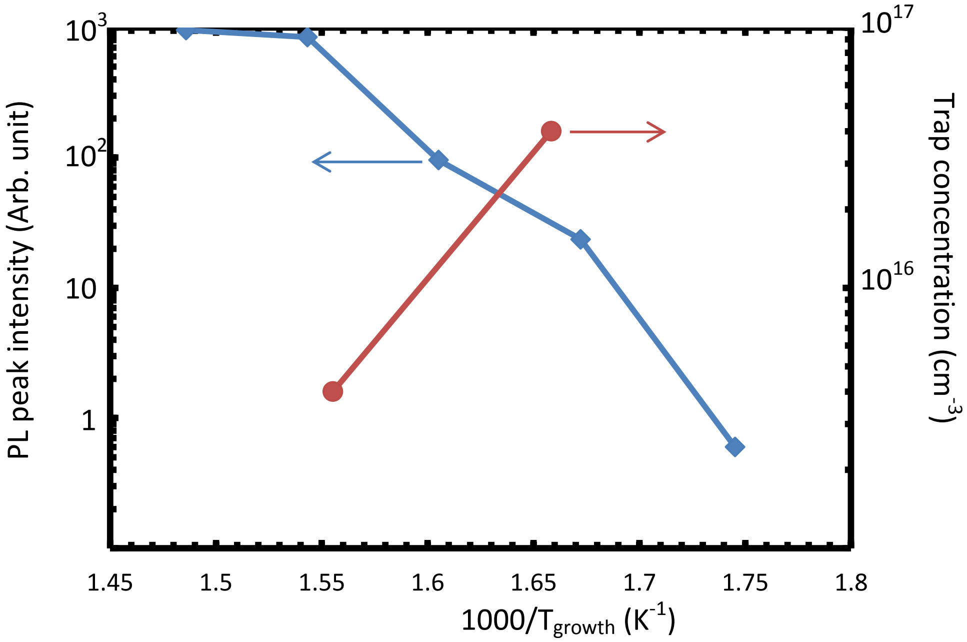

Figure 5-14: Growth temperature dependence of the PL intensity and total concentration of deep trap levels. The circular points are samples E and F from the current chapter and the square points are the samples in figure 4.1.

6. Group V ordering in GaAsBi

6.1. Contributions

This chapter is a summary of my investigation in the first two years of my PhD. The goal was to understand ordering, spontaneous long range arrangements of atoms, in III-V alloys. We begin the chapter with an introduction of the ordering concept and we continue with characterizing ordering in GaAsBi by x-ray and polarized PL methods. The chapter is concluded with some band structure simulations.

The GaAsBi samples which were used in this chapter had been grown by Daniel Beaton, Ryan Lewis and Mostafa Masnadi-Shirazi. The x-ray and PL measurements were all done by me.

6.2. Ordering in III-V alloys

Ordering in a crystal lattice happens when the atoms of an alloying element are arranged in certain direction and populate certain planes in the lattice in a periodic manner. Many III-V alloys are ordered spontaneously. The most frequently seen spontaneous ordering consists of monolayer super-lattice alternation along the <111> cubic body diagonals which is called CuPt ordering. There are two types of <111> ordering, CuPt (A), ordering along [111] or $[\bar{1}\bar{1}\bar{1}]$ directions, and CuPt (B), ordering along $[\bar{1}\bar{1}1]$ or $[1\bar{1}\bar{1}]$ directions [78]. As an example, figure 6.1 illustrates Cu-Pt ordering in GaAsBi alloy with Bi atoms occupying mostly the alternative {111} planes hence there are sequences of high and low Bi content {111} planes. These high Bi content planes can be described as {0.5 0.5 0.5} planes as their separations are twice the {111} planes' separation.

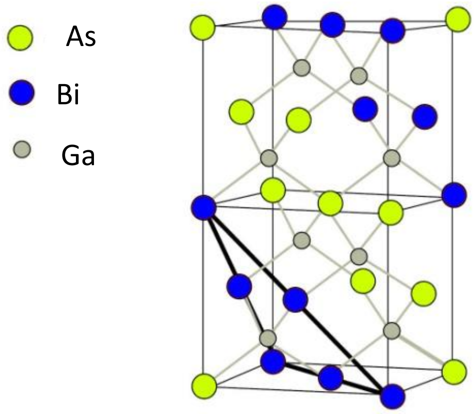

Figure 6-1: Cu-Pt ordering in GaAsBi alloy.

Ordering is caused by a surface driven phenomenon during growth. It relates the processes that are going on, on the surface during growth to the structure of the bulk material. We can relate surface reconstruction patterns to the ordering in the samples.

An ordered semiconductor has different properties along different crystal axes, for instance the optical and electrical properties like polarized photoluminescence and mobility change in two perpendicular crystal directions. Some vertical-cavity surface emitting lasers (VCSEL) applications like magneto-optic discs and coherent detection systems need the polarization state of the output to be well defined. The growth of ordered materials is one way to make lasers with well polarized output [79-82].

6.3. Detecting CuPt ordering in GaAsBi alloy by x-ray diffraction

As stated before (figure 6.1) CuPt ordering in GaAsBi creates new {0.5 0.5 0.5} lattice planes. It was initially shown by A. Norman et al. [83] that the electron diffraction pattern of ordered GaAsBi specimen has {0.5 0.5 0.5} reflections in between the origin and {111} diffraction points (figure 6.2). High resolution x-ray is a fast way of looking at different crystal plane diffractions without doing complex sample preparation. Although the intensity of the superlattice diffraction is weak, nevertheless we have observed for the first time CuPt ordering by x-ray diffraction.

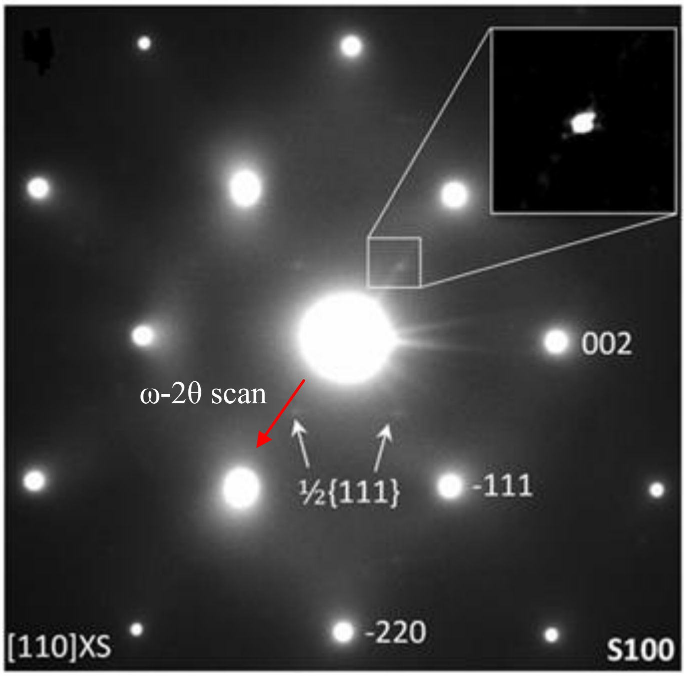

Figure 6-2: Electron diffraction pattern of an ordered GaAsBi sample. The image was copied from Reyes et al. [87].

We predicted that if an ordered sample is aligned along the (111) direction then an ω-2θ scan at small enough angle can diffract from the {0.5 0.5 0.5} planes. The red arrow on figure 6.2 shows the direction of such ω-2θ scan.

There was a difficulty with the x-ray geometry of the {0.5 0.5 0.5} planes. The epi-layers were grown on (001) GaAs substrates. The tilt angle between (0.5 0.5 0.5) plane and (001) surface (τ) is 54.75° which has to be subtracted from (0.5 0.5 0.5) Bragg's angle (θ_B=6.8°) to obtain the detector angular position for the asymmetric (0.5 0.5 0.5) x-ray scan. But the detector angular position for (0.5 0.5 0.5) plane turns out to be on the back of the wafer (figure 6.3), that is impossible to be set. To solve this problem, skew-symmetric geometry was used for (0.5 0.5 0.5) x-ray scan. The sample was rotated 90° around ϕ-axis and the sample was tilted 54.75° around Ψ-axis, therefore the detector and x-ray source only had to be set to meet the Bragg's angle θ_B on the sample surface.

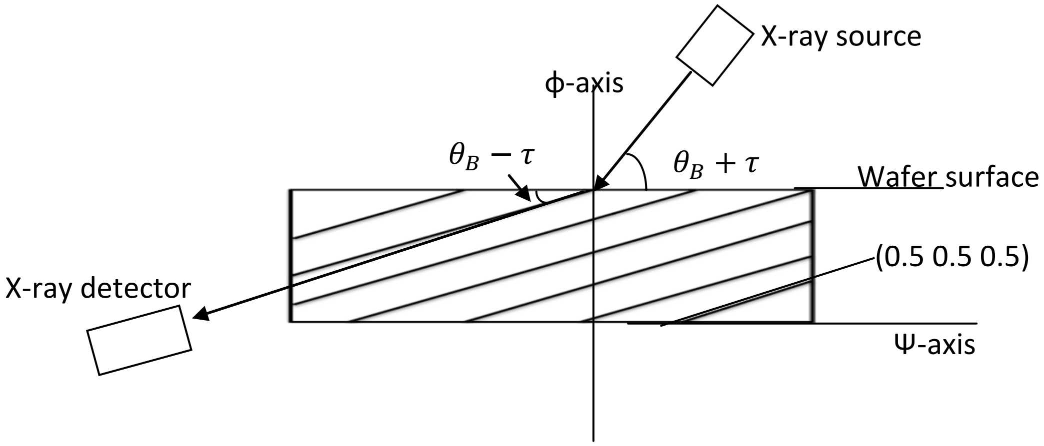

Figure 6-3: Asymmetric x-ray geometry

Four ω-2θ scans are performed on each sample with alignment on its respective (111) planes. The {0.5 0.5 0.5} peak appears in two of the four ω-2θ scans which is the indication of CuPt (B) along $[\bar{1}\bar{1}1]$ and $[1\bar{1}\bar{1}]$ directions. GaAsBi grows in domains [84], which causes ordered areas in both $[\bar{1}\bar{1}1]$ and $[1\bar{1}\bar{1}]$ directions. This type of segmented ordering has also been observed in GaInP [82]. Figure 6-4 shows the x-ray diffraction signal of an ordered sample. (111) peak emerges at ω~13.7° while the 1/2(111) peak appears at ω~6.8°.

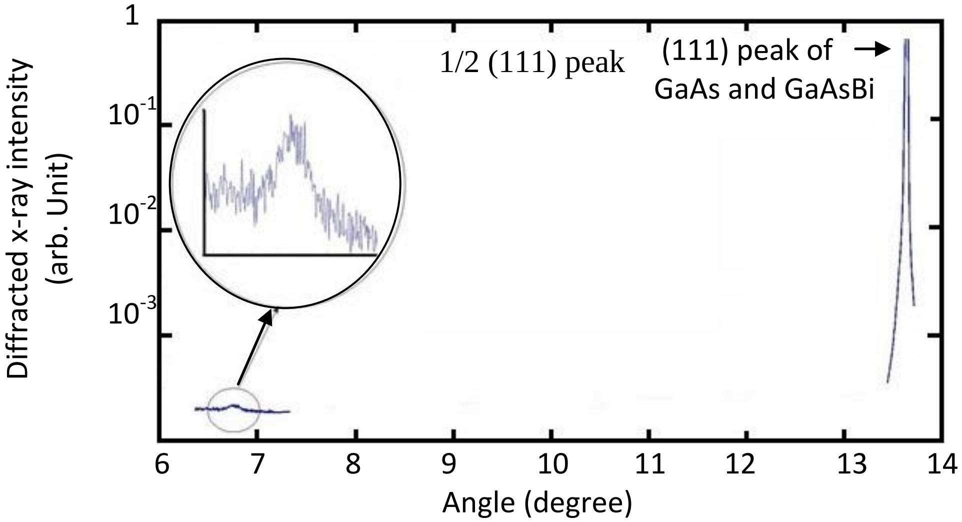

Figure 6-4: The experimental x-ray diffraction of ω-2θ scan of {0.5 0.5 0.5} peak. [Bi] = 1.8%.

Calculation of the {0.5 0.5 0.5} peak angle could help to decrease the time of the measurement as we search for the peak around the calculated value and it confirms the assignment of the peak. Differentiation of Bragg's law gives a relation between the change in crystal plane spacing due to strain ($\Delta d/d$) and the angular separation between the film and substrate peaks ($\Delta\theta$):

$$\frac{-\Delta d}{d} = \frac{\Delta\theta}{\tan(\theta)} \tag{6.1}$$

The distance between (111) planes in GaAsBi alloy can be calculated by replacing hkl indices in the following formula:

$$d_{hkl} = \frac{1}{\sqrt{(\frac{h}{a_{GaAs}})^2+(\frac{k}{a_{GaAs}})^2+(\frac{l}{a_{001GaAsBi}})^2}} \tag{6.2}$$

$a_{001GaAsBi}$ is calculated from $\Delta\theta_{004}$ and equation 6.1 then it is replaced into equation 6.2 to calculate $d_{111GaAsBi}$. Now, the Bragg law for (111) planes is used to calculate (111) planes Bragg angle ($\theta_{111calc}$). The difference between this calculated value and the measured value of (111) planes Bragg angle is the x-ray machine's offset for the sample which is added to the calculated Bragg angle of {0.5 0.5 0.5} planes ($\theta_{\frac{1}{2},\frac{1}{2},\frac{1}{2}} = \arcsin(\frac{\lambda_{xray}}{2\times d_{0.5,0.5,0.5}})$) to estimate the expected angle for the {0.5 0.5 0.5} x-ray diffraction peak.

6.4. Dynamical x-ray diffraction calculation and order parameter

An incoming x-ray beam is scattered by the electron cloud around the atoms inside the lattice. The scattering strength depends on the diffraction angle and the atomic number. Heavier atoms scatter more of the wave. The scattering strength of different types of elements have been measured and formulated in terms of the atomic form factor [85]:

$$f^0(\sin\theta/\lambda) = \sum_{i=1}^{4} a_i \exp\left(-b_i\left((\sin\theta/\lambda)^2\right) + c\right) \tag{6.3}$$

Where a_i, b_i and c are nine coefficients that can be looked up from a table for an element. The atomic form factors of the arsenic sites in GaAs can be weighted with arsenic and bismuth fractions to include Bi incorporation and ordering in a 64 atom supercell. Figure 6.5 illustrates the 64 atom supercell with group V (111) planes being either high (layer H) or low (layer L) bismuth content. We call the degree of ordering in the material the "order parameter" which is the ratio of the difference of layer H and L Bi concentration to the total Bi concentration:

$$\delta = \frac{x_H - x_L}{x_H + x_L} \tag{6.4}$$

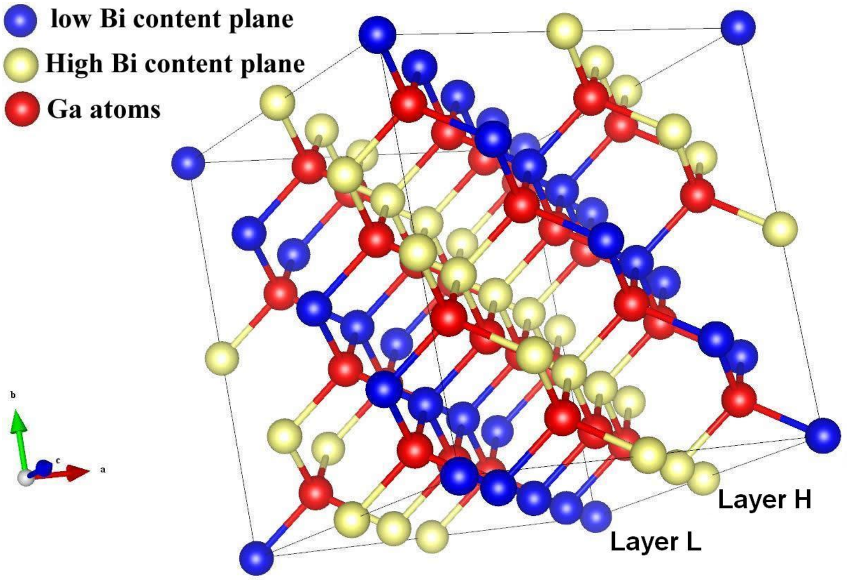

Figure 6-5: The 64 atom supercell which is used for the simulation of ordered GaAsBi alloy x-ray diffraction.

The weighed atomic form actor of the L layers turns into pure arsenic form factor when the material is 100% ordered:

$$f_L = f_{As} \times \delta + ((1 - x)f_{As} + xf_{Bi}) \times (1 - \delta) \tag{6.5}$$

The weighted atomic form factor of the H layers holds the entire Bi incorporation at 100% ordered material:

$$f_H = ((1-2x)f_{As} + 2xf_{Bi}) \times \delta + ((1-x)f_{As} + xf_{Bi}) \times (1-\delta) \qquad (6.6)$$

The structure factor is a complex-value unitless measure of the strength of scattering from a crystal, incorporating both the atomic form factors as well as the geometry of the crystal.

The atoms' positions (r_n) in the 64 atom supercell and atomic scattering factors from the equations 6.5 and 6.6 are plugged into the structure factor formula (equation 6.7) to calculate the structure factors along (111) and (0.5 0.5 0.5) directions:

$$SF = \sum\nolimits_{n=all\ supercell\ atoms} f_n \exp\left(-iK.r_n\right) \qquad (6.7)$$

K is the scattering vector from a set of crystal planes with Miller indices (h,k,l).

$$K = 2\pi/a(h\hat{x} + k\hat{y} + l\hat{z}) \qquad (6.8)$$

A recursive formulation for calculating the reflected amplitude of multi-layers and super-lattices was developed by Bartels et al. [86] which is called dynamical diffraction theory (DDT). The formulation was written in Python codes to simulate Sapphire x-ray diffraction by Scott Webster from University of British Colombia. I received the codes and rewrote them in Matlab for Zincblend GaAsBi crystal system. The DDT uses structure factor (equation 6.7) and calculates the transmitted and reflected beams from each super-lattice layer as they enter the Bragg condition and leave it. The complete description of the formulation is available in the Bartel et al. paper.

Figure 6.6 shows the measured {0.5 0.5 0.5} peak for a $GaAs_{0.983}Bi_{0.017}$ sample and its simulated curve from DDT. The peak width depends on the thickness, the detector slit size and ordered domains size. The simulation is done with an infinitely small detector slit on a single crystalline layer, so the simulated curve is much narrower than the experimental one. The ordered domain size (τ) is calculated from the broadening of the experimental peak with Scherrer equation [88]

$$\tau = \frac{K\lambda}{\beta cos\theta_B} \qquad (6.9)$$

K is a dimensionless shape factor with a typical value of 0.9. λ, θ_B and β are x-ray source wavelength, Bragg angle and the peak broadening (in radians) respectively. The calculated size of the ordered domains for figure 6.6 is 50 nm which is rather large therefore it is unlikely that the x-ray broad peak is due to the ordered domains.

The x-ray strength is proportional to the area under the peak and it can be used to fit an order parameter to the measurement which is 70% in the case of the sample in figure 6.6.

The search for ordered samples was done on a wide range of GaAsBi samples (30 samples) grown from 10 years earlier with different Bi contents and growth conditions but only 6 samples showed the {0.5 0.5 0.5} peak in their x-ray scans. The small number of ordered samples provoked us to see if the Bi incorporation or certain growth conditions could improve ordering.

The area under the peak increases with increasing values of the order parameter and epi-layer thickness so a larger peak is expected from thicker and more ordered samples. Figure 6.7 shows the peak area calculation for a couple of different Bi concentrations. The Bi concentrations and thicknesses belong to the ordered samples that we found in x-ray experiments.

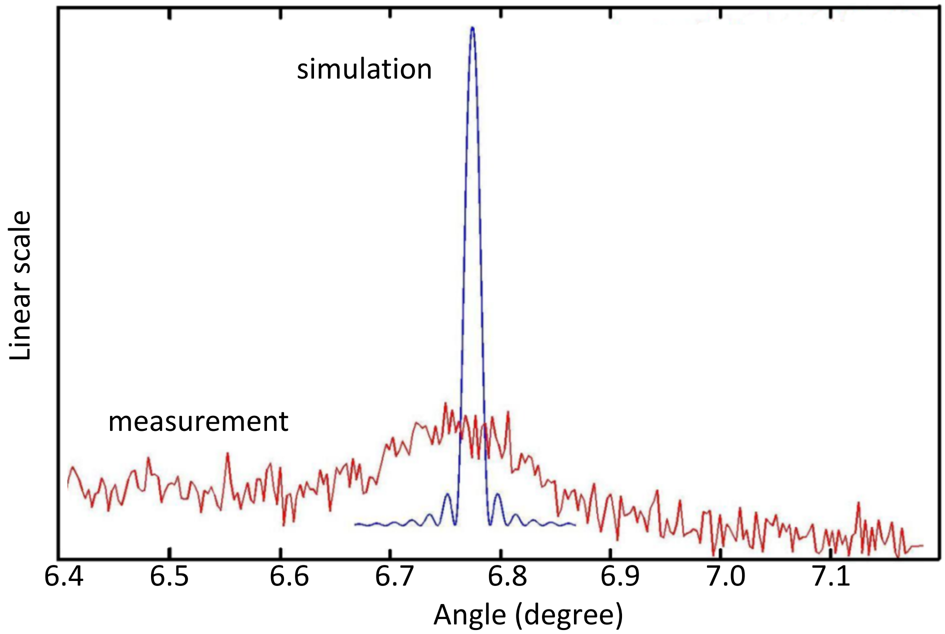

Figure 6-6: The experimental and simulation result for {0.5 0.5 0.5} peak of a sample with [Bi]=1.68% and thickness = 280 nm, which results in δ =70%.

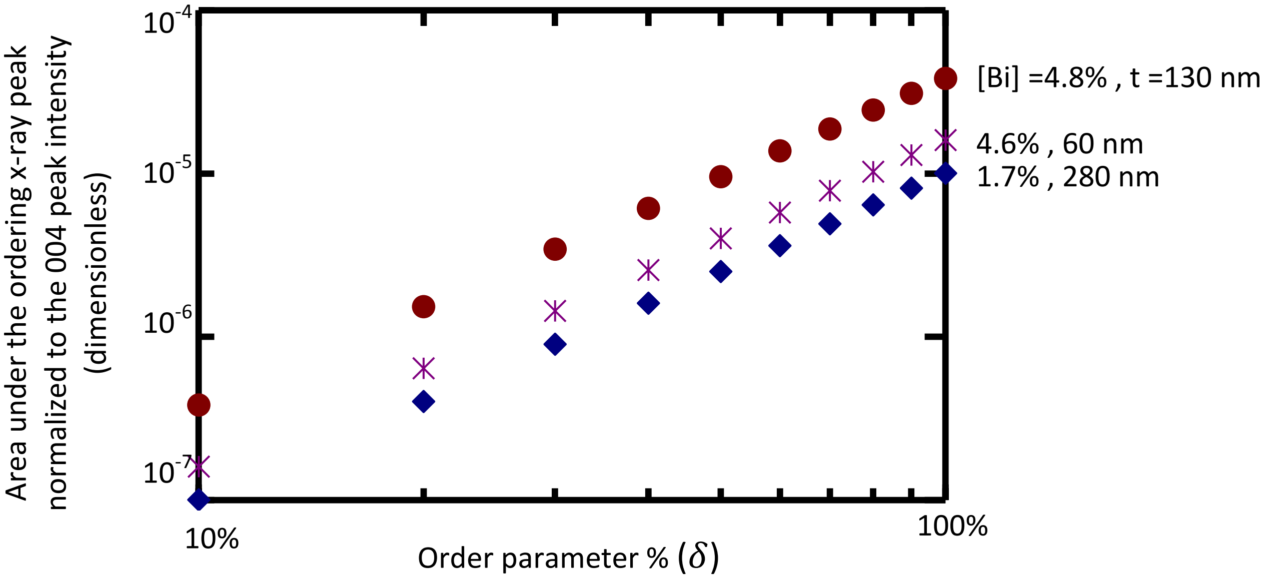

Figure 6-7: Area under the {0.5 0.5 0.5} peak normalized to the 004 peak intensity as a function of order parameter (log-log scale) calculated by DDT. Simulations were done with thickness and Bi concentration of the available ordered samples to fit the order parameter to the experimental data.

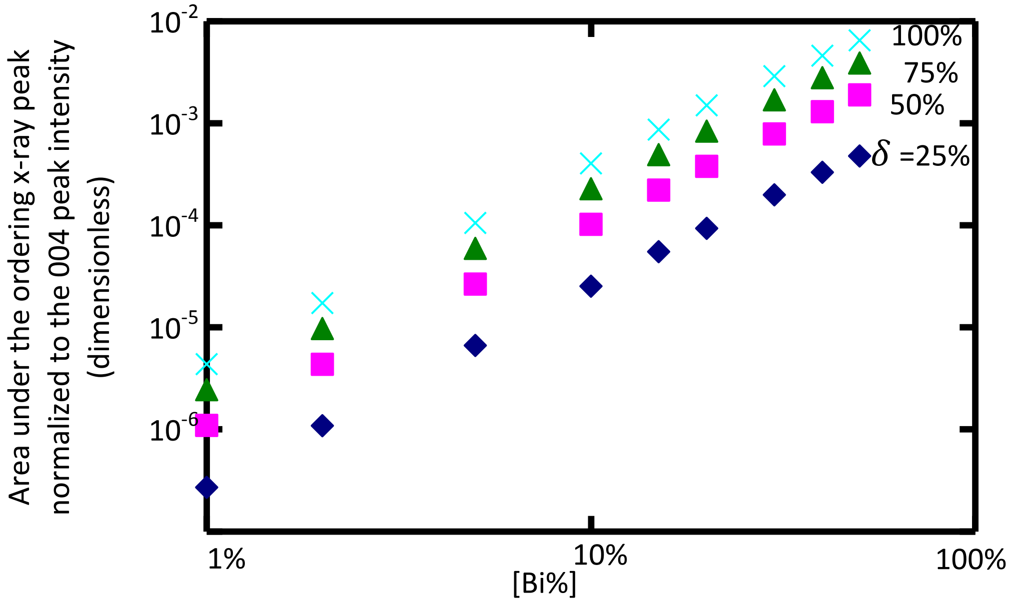

Figure 6-8: The area under the {0.5 0.5 0.5} peak normalized to the 004 peak intensity vs. Bi concentration, for four different order parameter values calculated by DDT. The thickness is 280 nm for all the curves. Bi concentration and order parameter increase the peak area.

The order parameters of the ordered samples were found by calculating the area under their {0.5 0.5 0.5} measured peak and comparing with plots similar to figures 6.7 and 6.8. Figure 6.9 shows the order parameter of the samples as a function of Bi content. The measured order parameter decreases linearly with Bi concentration and varies between 40% to 70% for a fixed Bi concentration near 1.7%.

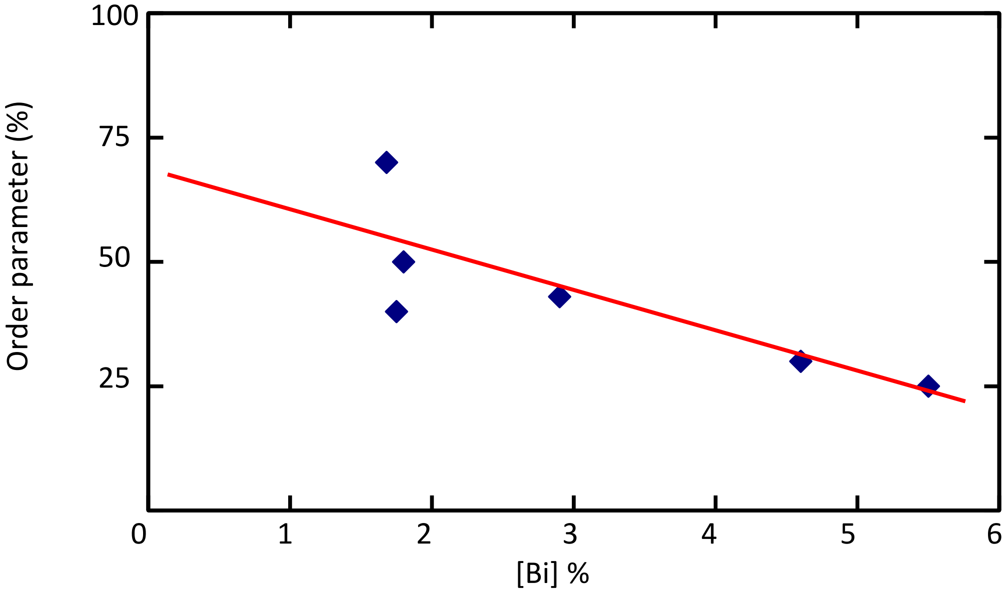

Figure 6-9: The fitted values for the order parameters of the ordered samples vs. their Bi concentration. The red line is a guide to the eye.

It had been observed in GaInAs and other III-V alloys that CuPt ordering depends on the growth temperature and growth rate [89,90]. GaInAs shows more Cu-Pt ordering when its growth temperature is lowered from 700 to 550°C. It was explained as the competing processes of growth surface-induced ordering and bulk disordering [90]. The growth conditions of the ordered GaAsBi samples were investigated to look for similar correlations to GaInAs. The growth conditions of the ordered samples are listed in table 6.1. The As_2/Ga (BEP) ratio is not included because this important parameter was not being measured regularly at the time of the growths. The samples that did not show ordering are listed in table 6.2. The first obvious condition which is common for all the ordered samples in table 6.1 is the 2×1 surface reconstruction. The 2×1 reconstruction does not guarantee CuPt ordering, as many 2×1 grown samples do not show ordering (table 6.2). The importance of 2×1 surface reconstruction in the occurrence of CuPt ordering occurrence has been suggested before by other groups and our results confirm it [83].

Table 6-1: Growth conditions of the ordered samples in the UVIC MBE lab. The Ga, As and Bi source temperatures were the same for all the ordered samples, namely 850, 350 and 450°C respectively. The Bi content and thicknesses are inferred from (004) x-ray scan simulations.

Sample #	Order parameter	[Bi]	Thickness (nm)	Surface reconstruction	Growth temp. (°C)
R2182	50%	1.80%	360	2×1	352
R2178	70%	1.68%	280	1×3 and mostly 2×1	360
R2171	40%	1.75%	300	Mostly 2×1	350
R2165	43%	2.90%	380	Mostly 2×1	320
R2148	25%	4.8%	130	1×3 and mostly 2×1	305
R2152	30%	4.60%	60	1×3, mostly 2×1 and 2×chevron	303

Table 6-2: Growth conditions of the samples that did not show the ordering peak. The Ga, As and Bi source temperatures were not the same for the samples and were equal to 850-941, 300-350-360-370 and 450-475-500-575°C respectively. The Bi content and thicknesses are inferred from (004) x-ray scan simulations

Sample #	[Bi]	Thickness (nm)	Surface reconstruction	Growth temp. (°C)
R2018	2.72 %	119	No data	295
R2031	2.58 %	50	No data	303
R2080	1.9%	220	2×1	295
R2087	2.32 %	100	2×4 , 1×3 and 2×3	300-360-425
R2139	5%	110	2×1, 2×chevron	297
R2147	4.4%	40	1×3, mostly 2×1	300
R2164	1.9%	250	Mostly 2×1	360
R2275	2.2%	261	1×	245
R2286	12.5 %	220	2×chevron	225
R2288	17.8 %	7	No data	223
R2295	4.5%	20	2×chevron	227
R2297	3.2%	7	No data	280
R2298	4.8%	10	1×1	225
R2299	10%	183	No data	225

R2300	2.5%	240	2×1, 1×3 and 2×3	330
R2301	2%	500	2×1	323
R2304	4.25%	250	1×chevron	220
R2305	2.55%	100	2×very dim	330
R2310	1.35%	670	2×chevron, 2×1	328
R2313	5.75%	40	1×3, 2×1 and 2×chevron	265
R2315	1.55%	660	1×3	330

Figure 6.10 shows the ordering parameter of the samples as a function of growth temperature. The red line has been added for eye-help. Higher growth temperature causes more ordering. This can be a result of the larger mobility of the atoms on the surface at higher growth temperatures which allows them to find the ordered sites in the lattice. Systems in thermodynamic equilibrium normally order at low temperatures. As noted above GaInAs shows more ordering at 550°C than at 700°C, which is consistent with this expectation. In the case of crystal growth limited by chemical kinetics however, more order would be expected at higher temperature for which the atoms can more readily find the lowest energy configuration through motion. The fact that the GaAsBi system shows more ordering at 380°C than at 310°C suggests that kinetic limitations are a factor in film growth at this temperature. Also relevant is that the increase in ordering occurs in a lower temperature regime (310°C - 380°C) than in the case of GaInAs system (550°C - 700°C), which shows the opposite temperature dependence. This observation is consistent with the DLTS and PL results which show fewer deep level defects at high growth temperatures. This is another indication of a more ordered crystal at high growth

temperatures. The ordering associated with the deep levels is more strongly temperature dependent than in the case of the Cu-Pt ordering because the energies associated with the disordered state are higher. Unfortunately, I began working on the VECSEL project at the time and could not test the results to grow ordered samples.

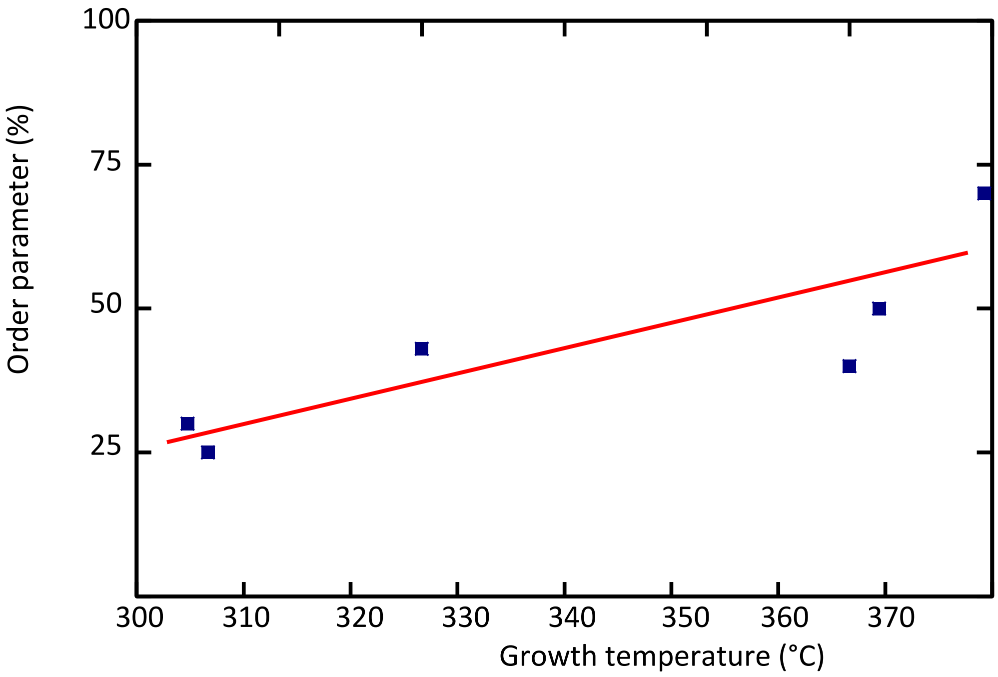

Figure 6-10: Order parameter as a function of growth temperature. The red line is a guide to the eye.

6.5. Polarized PL results

The band structure along the ordering direction is different from the direction perpendicular to it and this causes different optical and electrical properties along different lattice directions. The PL emission is one of the properties that depends strongly on the band structure. Adding a Glan-Taylor prism polarizer in front of the detector allows only the light emitted from one of the band structure directions to get in. The sample is rotated 90°, four times, to take the light from the perpendicular directions. We observed that the PL intensity and wavelengths in two perpendicular directions are different in the CuPt ordered samples.

Figure 6.11 shows the room temperature polarized PL experimental results for a 1.8% GaAsBi sample with 70% order parameter. The PL intensity is normalized to signify the wavelength shift in the peak position. The shift is 10 nm (0.01eV) in the figure. When the polarizer is removed from the setup, the peak position is at an average location in the middle of the two polarized peaks.

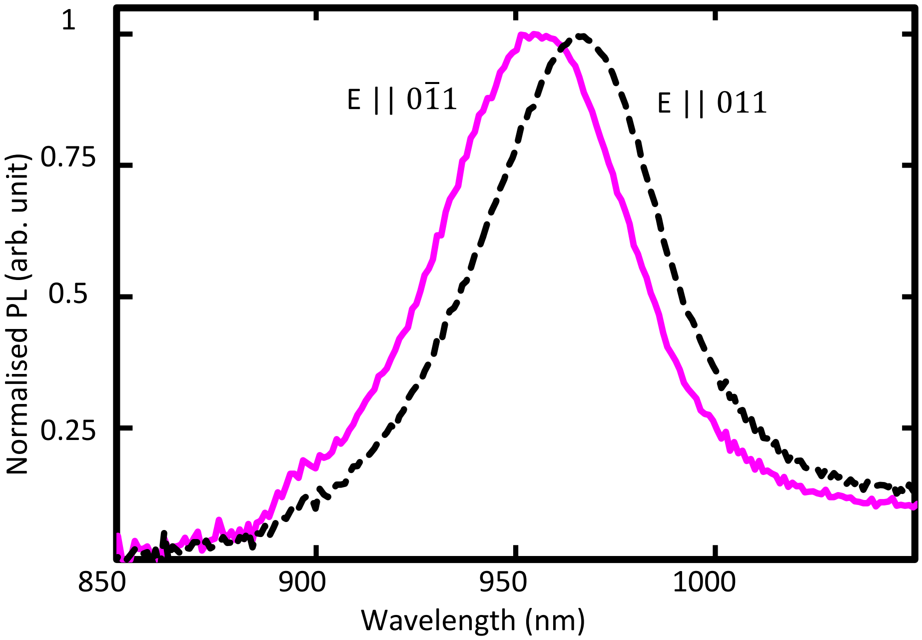

Figure 6-11: The room temperature polarized PL experimental results for a GaAsBi sample with 1.8% Bi content and 70% order parameter.

The polarized PL experiment was carried out as a function of temperature from room temperature to 25K (figure 6.12). It was observed that the separation between the two polarized PL peaks decreases linearly with the temperature reduction. We assume the valence band is different in the two directions parallel and perpendicular to the ordering direction as in figure 6.13 for example. The electrons and holes are distributed with a Boltzmann distribution in the band structure and all the recombination occurs inside the red rectangle in figure 6.13. The transitions from the conduction band to the perpendicular valence band occur with higher energies than the parallel valence band transitions and cause different PL wavelengths for the two directions. When the temperature decreases the carriers are frozen around the Γ point where the difference between the parallel and perpendicular valence bands is much less and the PL emission becomes the same for both directions.

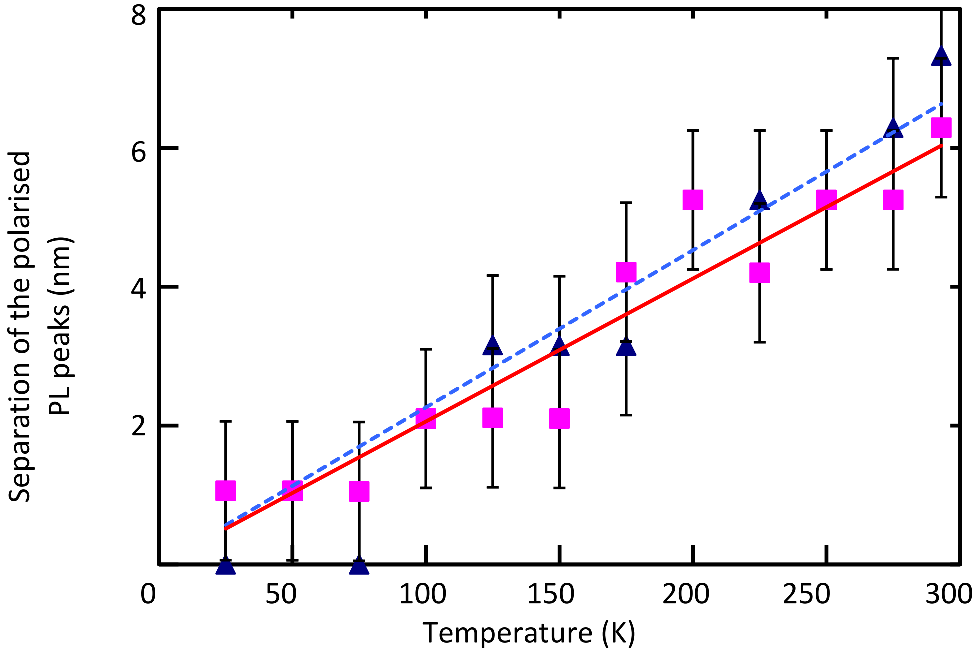

Figure 6-12: Separation of the polarized PL peaks decreases linearly at low temperature and disappears at 0K. The square data points belong to a [Bi]=1.68% sample and the line is a linear fit to them. The triangle data points belong to a [Bi]=1.8% sample and the dotted line is a linear fit to these data points.

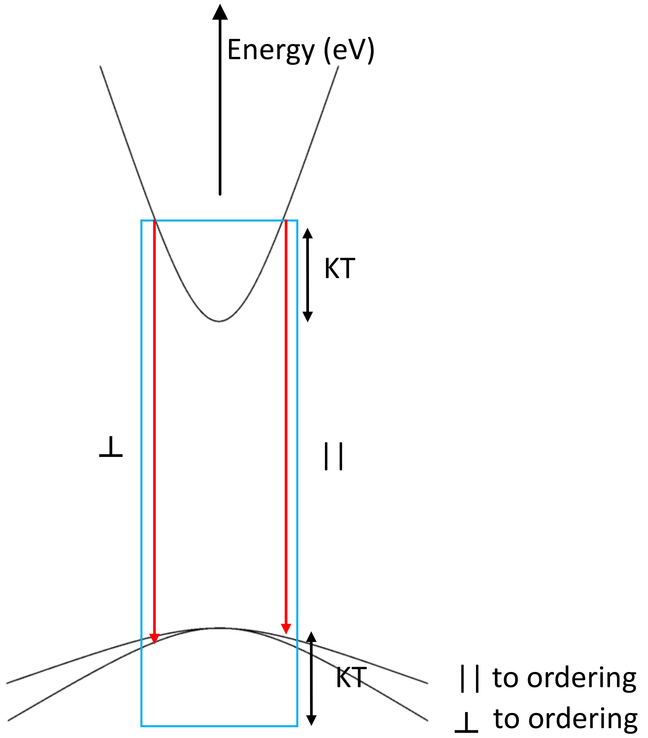

Figure 6-13: The valence band is different in the two directions parallel and perpendicular to the ordering direction.

O’Reilly et al. [91] used a tight binding model to calculate the band structure of ordered GaInP material and predicted the separation in the polarized PL. He calculated the polarized PL separation with the assumption of directional strain. His room temperature results show that polarized PL peak separation of 10 nm can occur in GaInP, although he does not have low temperature result to compare with figure 6.12.

6.6. Westgrid computer network

Westgrid is a network of super computers which are used by researchers in Canada for large calculations. Westgrid computational work is done through batch-processing. Job scripts containing execution commands are submitted to the server through a batch file handling system which queues the requests, allocates processors and manages the jobs. A general user does not have to know how the batch handler works. The only things to know are the commands to add the job to the system with the desired number of processors and estimated process time. The user also needs an ftp file monitor program to access the allocated memory on the server [92].

6.6.1. DFT calculation results

DFT (density functional theory) is a quantum mechanical method to model electronic band structure. There are numerous open source programs to do DFT calculations but only two of them are available on Westgrid for free use: Siesta and ABINIT. Siesta [93] is preferred for large molecule simulations in chemistry. Siesta does not include spin-orbit (SO) interaction, therefore it is not the best option for semiconductor band structure calculations where SO plays an important role in lifting degeneracies and making band splitting. ABINT [94] is the other open source program for DFT calculation available on Westgrid. It includes SO interaction and I used it for the band structure calculations in this section.

The 64 atom supercell was used to model 3, 6, 9 and 12% Bi concentrations with CuPt ordered or randomly distributed bismuth atoms in the lattice. The Bi atoms could be placed in the neighboring positions (clustered) or far from each other. The degree of clustering of the supercell was described by cluster parameter (C). A 12% Bi concentration supercell is shown in figure 6.14; The 4 Bi atoms are in a square cluster to make the largest cluster with ordering (C=100%). The 4 Bi atoms connected to one Ga atom on two (111) planes make a lager cluster but without ordering.

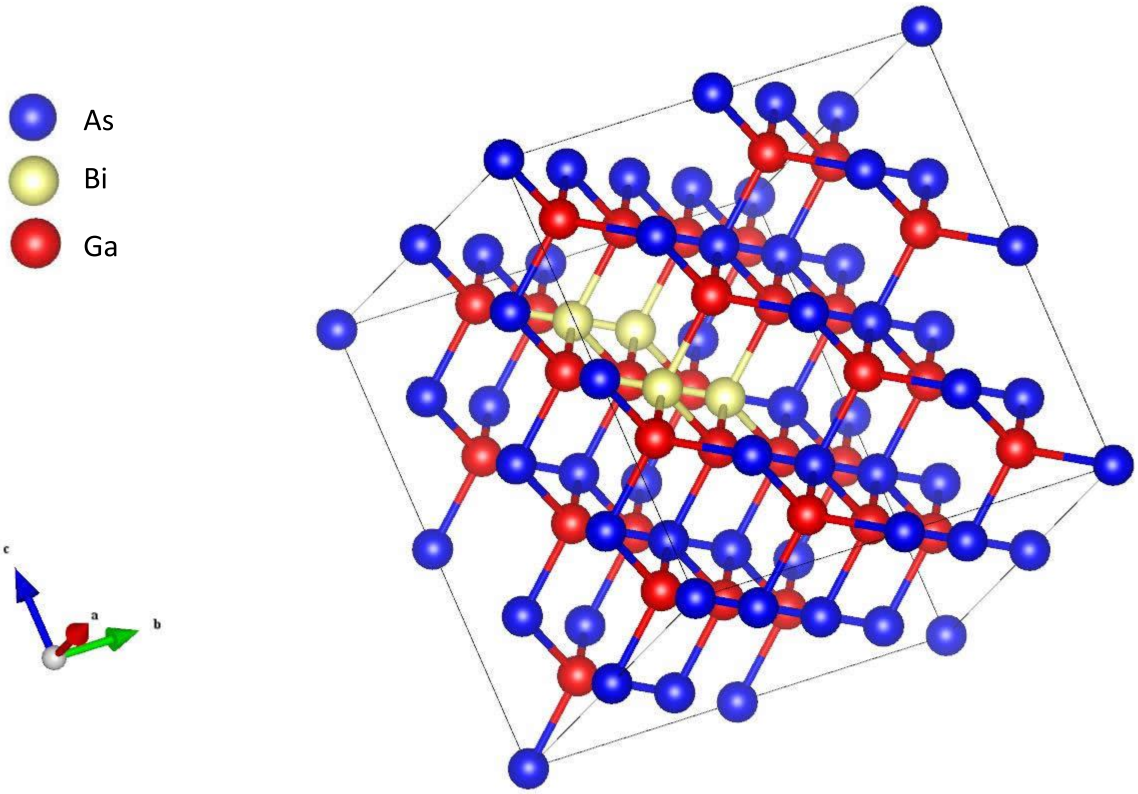

Figure 6-14: GaAsBi supercell for Bi%=12% with cluster parameter of 100%.

The band structure calculation was run for 0, 3, 6, 9 and 12% GaAsBi supercells. Some of the band structures are shown in figure 6.15 (C=100% and δ=100%). The Brillouin zones are all folded except for GaAs, which had the basic unit cell for the simulation. The L, Γ and X reciprocal points are [111], [000] and [001] real space directions respectively. L is in the direction of the ordering in the supercell.

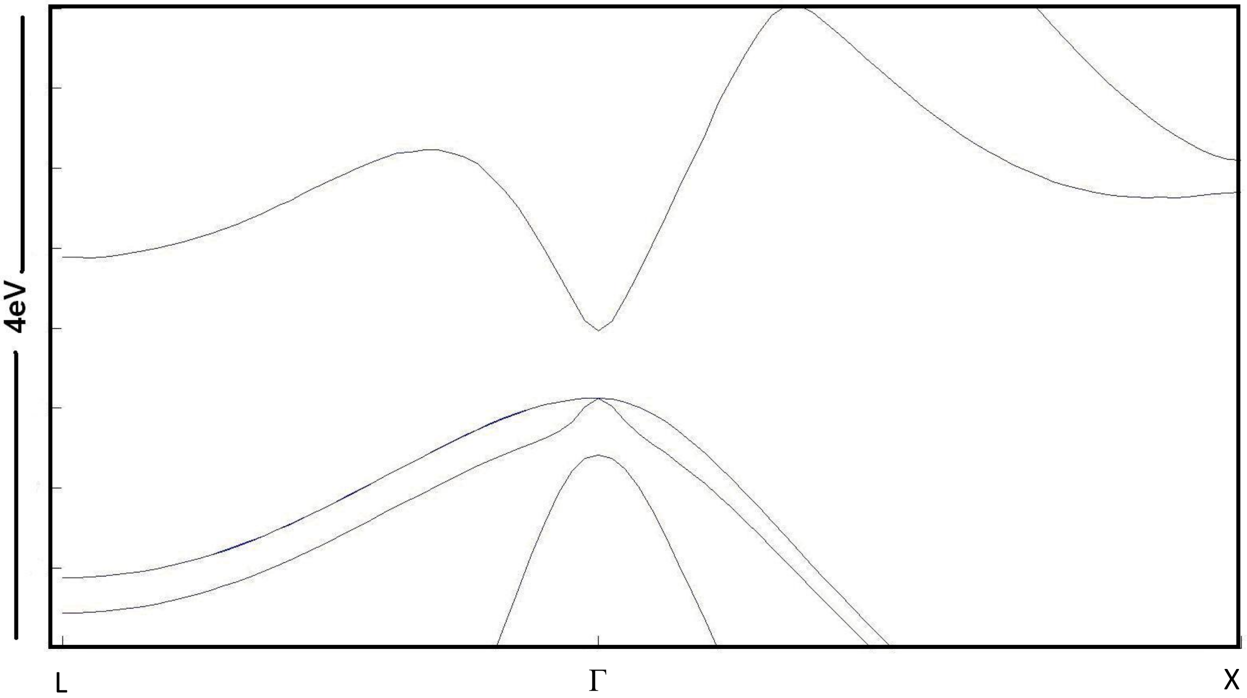

A) GaAs

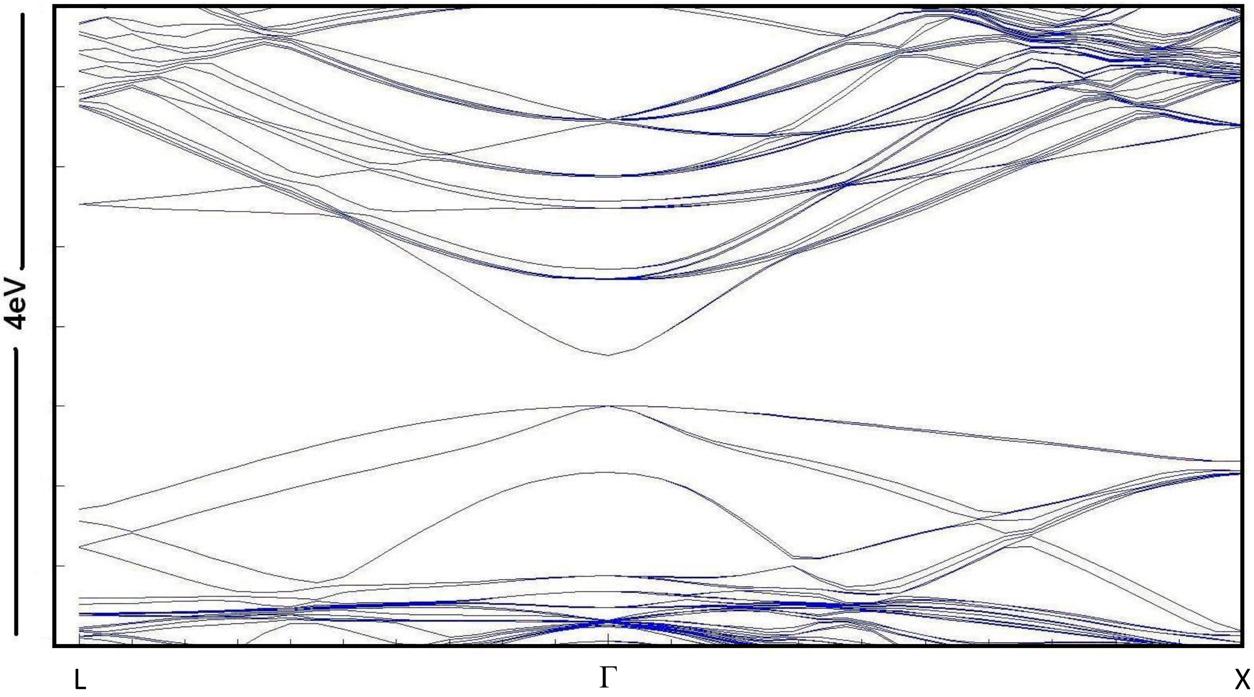

B) GaAsBi , Bi%=3%

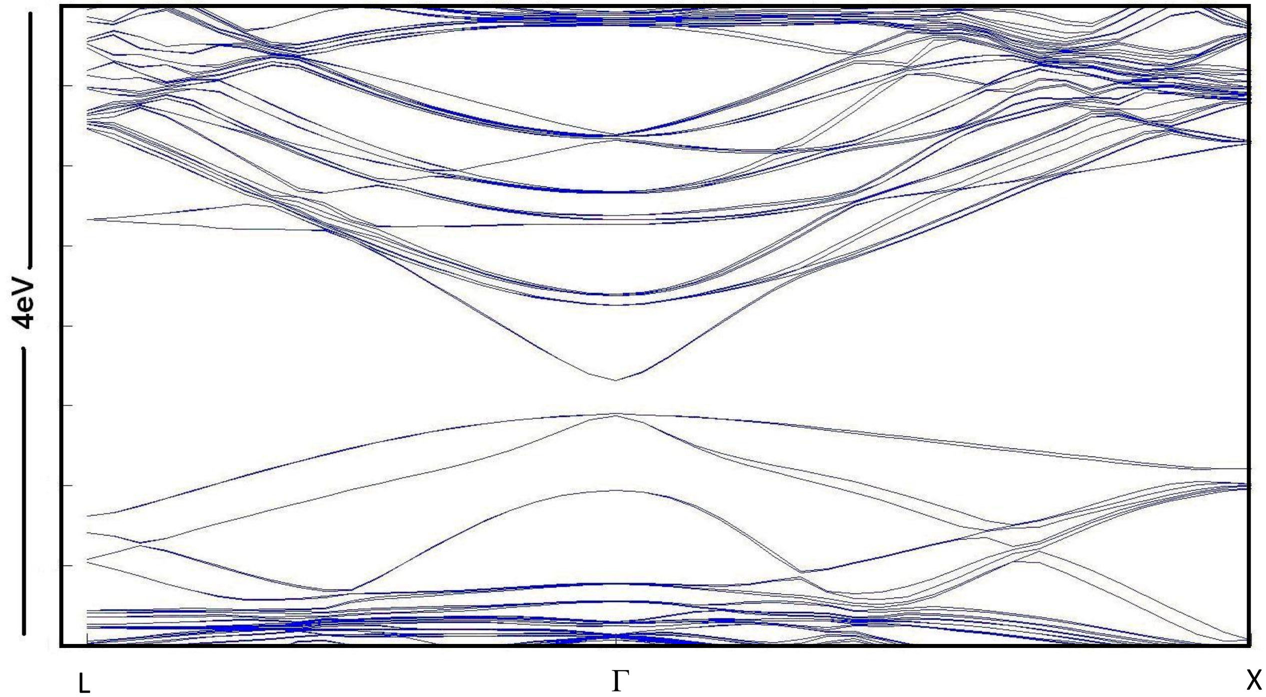

C) GaAsBi , Bi%=6%

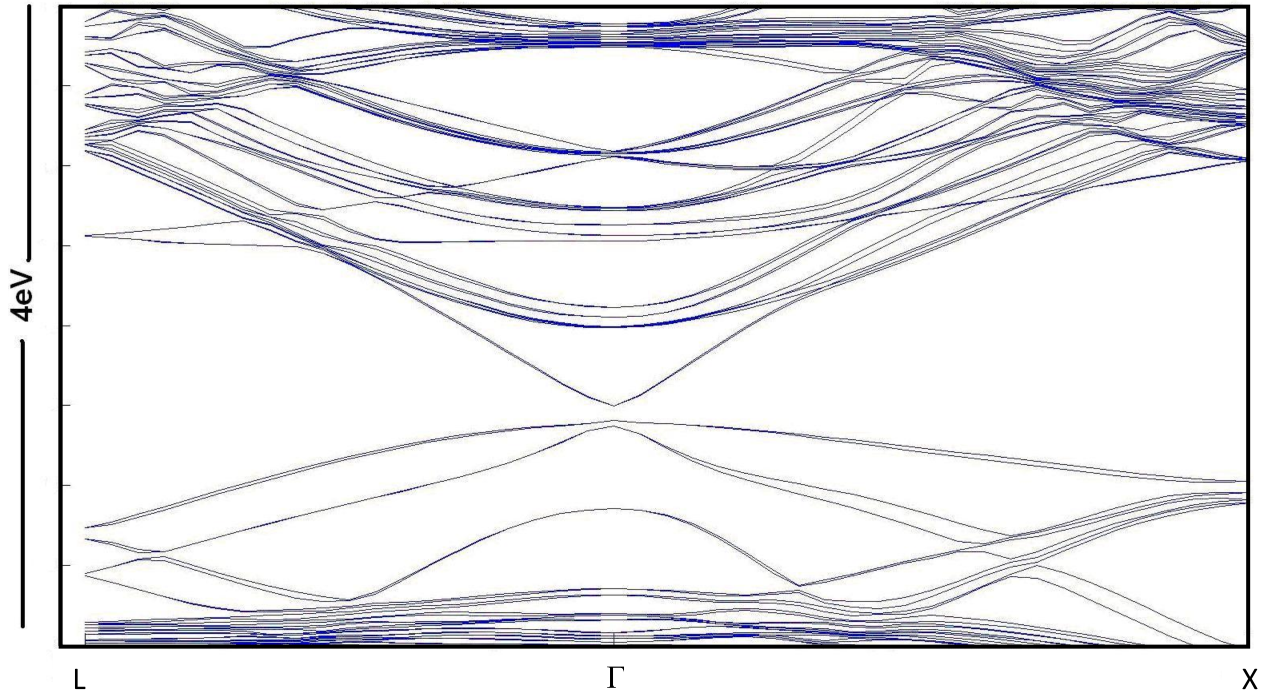

D) GaAsBi , Bi%=9%

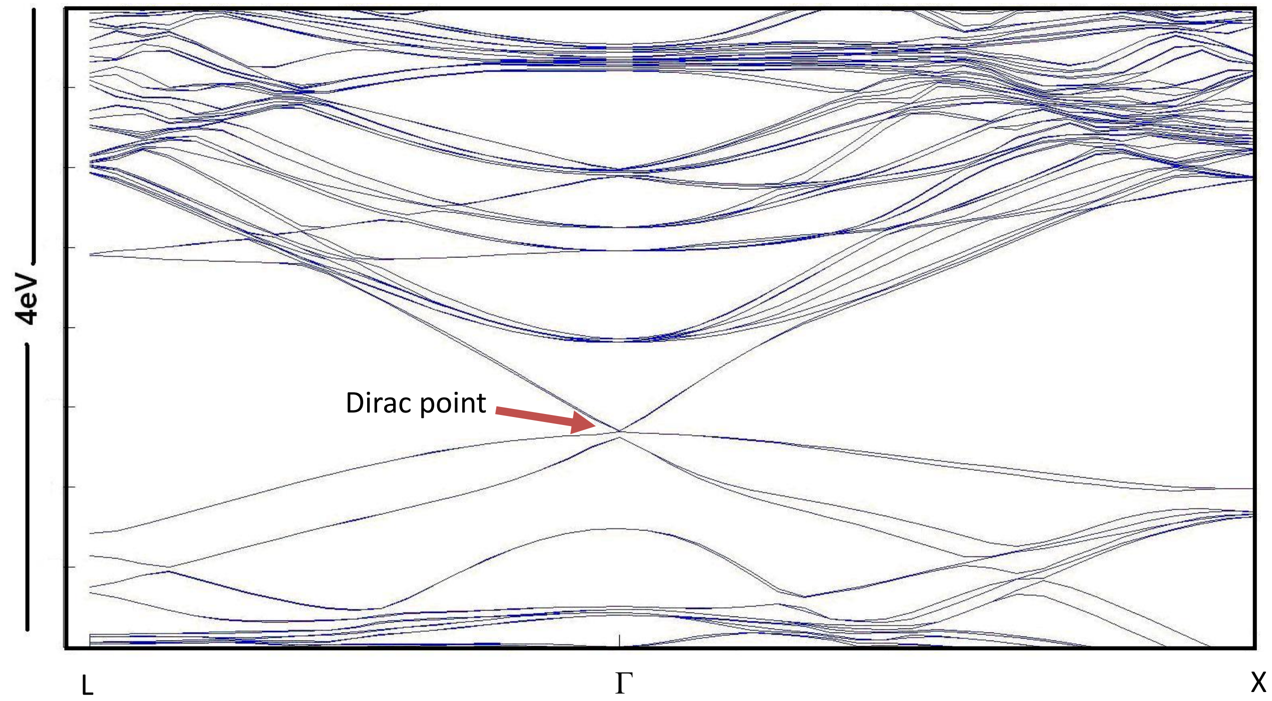

E) GaAsBi , Bi%=12%

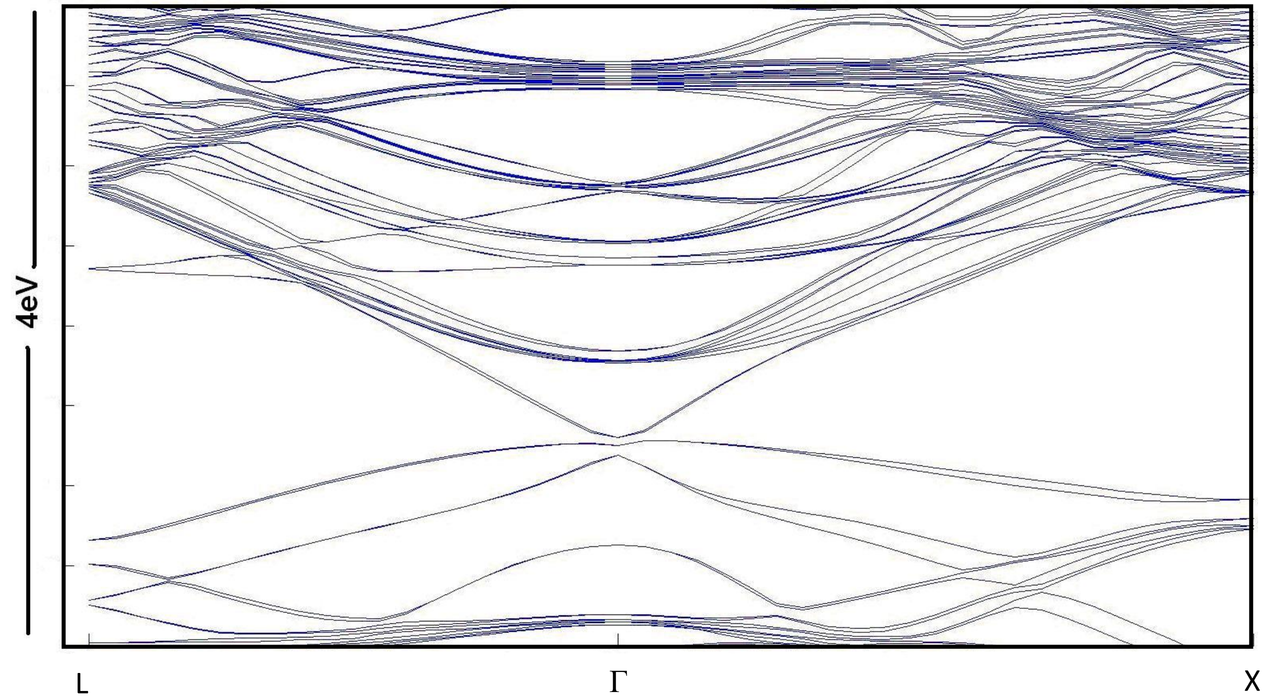

F) GaAsBi , Bi%=15%

Figure 6-15: GaAsBi band structure calculated by ABINIT program on Westgrid network.

The bandgap that is calculated by the DFT method is incorrect and in disagreement with experimental measurement as expected, but it follows the slope of the real material bandgap quite well (Figure 6.16). The calculated band structure of GaAsBi with a semiconductor bandgap changes into a metallic band structure when [Bi]=12% (figure 6.15). At 12% Bi incorporation the conduction and valence bands intercept each other at the Γ point and the bandgap becomes zero and the energy dispersion becomes linear with momentum (figure 6.15 E). The Γ point in this situation is called a Dirac point [95]. The effective mass goes to zero at the Dirac point and it is predicted to cause super high carrier mobility in GaAsBi similar to graphene. It should be noted that due to the well-known bandgap error in the DFT method, the Bi content which causes zero bandgap in DFT is offset from the experimental value. The slope of the experimentally measured bandgap extrapolates to zero bandgap at 30% Bi content [18].

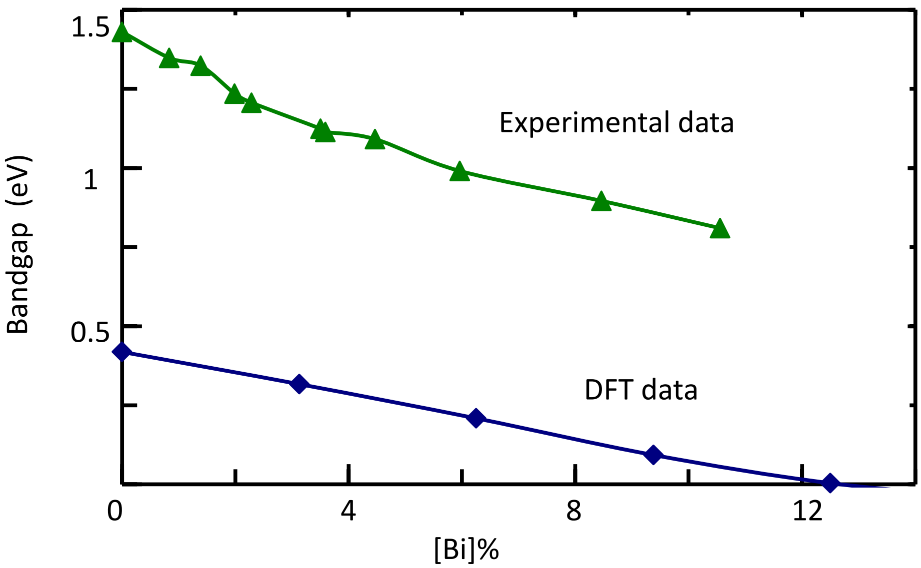

Figure 6-16: The GaAsBi bandgap calculated by DFT is not correct but it follows the slope of the experimentally measured bandgap quite well above 5% Bi incorporation [18].

The splitting between the heavy and light hole bands is the next thing which is different in the GaAsBi band structures from GaAs in figure 6.15. Our DFT calculation shows that the splitting is more significant in the GaAsBi supercells with more Bi clustering and Bi content. Figure 6-17 shows the calculated HH-LH splitting for some different Bi contents with and without clustering. The splitting increases with Bi incorporation and clustering. Adding Bi atoms to the supercell breaks the symmetries and causes the splitting. More symmetric 3% and 6% Bi content supercells have zero splitting in figure 6.17.

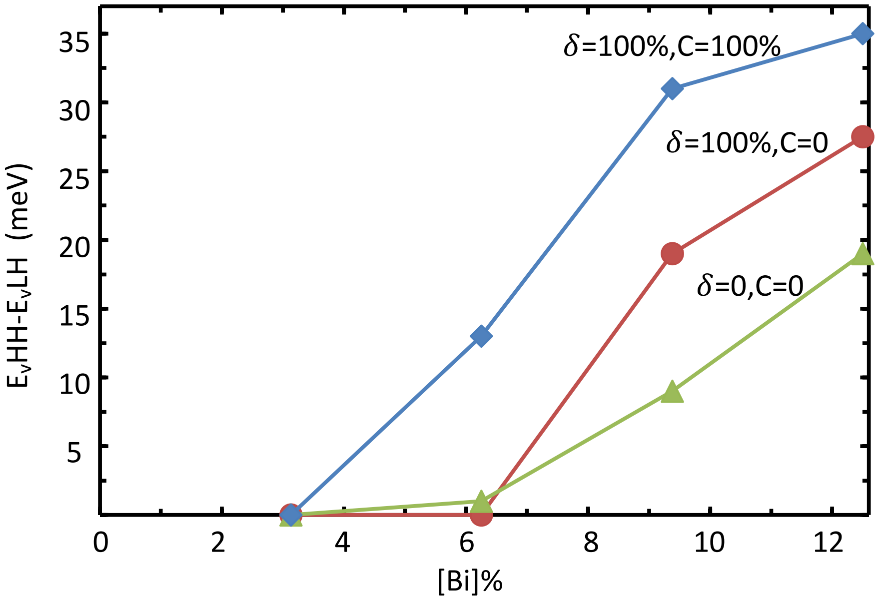

Figure 6-17: The HH-LH splitting as a function of Bi concentration for three different ordering and clustering parameters.

7. Conclusions of the thesis and future developments

The most important achievement of this thesis is the demonstration of how the growth conditions affect the optical properties and deep trap levels of GaAsBi alloys. This was the first time that such comprehensive research was done and it showed how one can grow high quality GaAsBi with much less defects and non-radiative recombination centers. Previous works on GaAsBi growth conditions were focused on the dynamics of the incorporation of Bi into GaAs.

Growth of GaAsBi alloy depends on four conditions: substrate temperature less than 400°C, small arsenic pressure close to stoichiometric surface condition (As:Ga (flux) =1), bismuth flux and growth rate (gallium flux). The first three of the four growth conditions were investigated thoroughly in chapter 4 and the results showed that PL intensity is not a strong function of arsenic pressure and bismuth flux whereas substrate temperature has a strong effect on PL intensity. When the substrate temperature during growth was reduced from 400°C to 300°C and all other growth conditions were fixed, the Bi concentration in the deposited films increased from 1% to 5% and the PL intensity decreased by more than a factor of 1000. Two samples were grown at different temperatures (330 °C and 375 °C) with approximately the same Bi concentration (~2%) at a stoichiometric As:Ga flux ratio. The temperature dependence of the PL shows that both samples' spectra have sub-bandgap emission from the defect states. The defect emission is much larger in the 330°C grown sample spectrum indicating a higher density of shallow localized states. This causes the band edge emission to be 29% less temperature dependent than the band edge emission of the 375°C grown sample. The DLTS technique was used to measure the concentrations and activation energies of the deep level states in two n+/p GaAsBi one-sided diodes, grown at 330°C and 370°C. The measurements showed that the trap concentration drops 10× with a 40ºC reduction in growth temperature.

Group V Cu-Pt ordering was investigated in GaAsBi alloys, in chapter 6. GaAsBi system shows more ordering at high growth temperature (380°C) than at low growth temperature (310°C). This indicates that GaAsBi growth is limited by chemical kinetics. From the PL, DLTS and ordering result, it is concluded that high growth temperature increases crystal ordering and decreases the density of shallow and deep level crystal defects. Therefore GaAsBi material should be grown at the growth temperature as high as possible, to achieve the best crystal quality.

A VECSEL laser structure was grown with optimized high quality GaAsBi material. Although the cross section SEM pictures of the sample showed good layer growth, our collaborators in Finland were not able to make the sample lase. They blamed surface defects for the scattering of the pump laser and the eventual failure.

One of the things which could be done in the future is to investigate the growth rate effect on GaAsBi quality. Bi flux and arsenic pressure are changed with growth rate therefore the growth rate effect has to be separated out from the other two growth conditions.

TEM (Transmission Electron Microscopy) of the VECSEL sample can help to investigate the reasons of its failure. The uniformity of the QWs' Bi content and the smoothness of the QW-barrier interfaces can be investigated from TEM images.

Growing GaAsBi solar cell structure with the high quality GaAsBi material is also a good project but it needs the DRS setup program to be modified so that it can read temperature from p+GaAs substrates and give accurate substrate temperature readouts for accurate control of the growth.

Bibliography

[1] Silicon photonics, B. Jalali, S. Fathpour, J. Lightwave Technol., 24, 4600-4615 (2006)

[2] Hall coefficient factor for polar mode scattering in n-type GaAs, G. E. Stillman, C. M. Waife, J. O. Dimmock, J. Phys. Chem. Solids, 6, 1199-1204 (1970)

[3] GaBiAs: A material for optoelectronic terahertz devices, K. Bertulis, A. Krotkus, G. Aleksejenko, V. Pacebutas, R. Adomavicius, G. Molis, S. Marcinkevicius, Appl. Phys. Lett., 88, 201112 (2006)

[4] Fiber-optic communication systems, G. P. Agrawal, Wiley (2010)

[5] Quantum well lasers, P. S. Zory, Academic Press, p. 58-150 (1993)

[6] The anomalous bandgap bowing in GaAsN, U. Tisch, E. Finkman, J. Salzman, Appl. Phys. Lett., 81, 463 (2002)

[7] Role of nitrogen in the mobility drop of electrons in modulation-doped GaAsN/AlGaAs heterostructures, R. Mouilleta, L. A. de Vaulchier, E. Deleporte, Y. Guldner, L. Travers, J. C. Harmand, Solid State Commun., 126, 333-337 (2003)

[8] Improved optical quality of GaNAsSb in the dilute Sb limit, H. B. Yuen, S. R. Bank, M. A. Wistey, J. S. Harris, M. Seong, S. Yoon, R. Kudrawiec, J. Misiewicz, J. Appl. Phys., 97, 113510 (2005)

[9] Surfactant enhanced growth of GaNAs and InGaNAs using bismuth, S. Tixier, M. Adamcyk, E.C. Young, J. H. Schmid, T. Tiedje, J. Cryst. Growth, 251, 449-454 (2003)

[10] Theoretical study of the effects of isovalent coalloying of Bi and N in GaAs, A. Janotti, S. Wei, S. B. Zhang, Phys. Rev. B, 65, 115203 (2002)

[11] Similar and dissimilar aspects of III-V semiconductors containing Bi versus N, Y. Zhang, A. Mascarenhas, L. W. Wang, Phys. Rev. B, 71, 155201 (2005)

[12] Giant spin-orbit bowing in $GaAs_{1-x}Bi_x$, B. Fluegel, S. Francoeur, A. Mascarenhas, S. Tixier, E. C. Young, T. Tiedje, Phys. Rev. Lett., 97, 067205 (2006)

[13] Carrier–phonon coupling in $GaAs_{1-x}Bi_x$/GaAs quantum wells, S. Imhof, A. Thränhardt, A Chernikov, M. Koch, N. S. Köster, K. Kolata, S. Chatterjee, S. W. Koch,

X. Lu, S. R. Johnson, D. A. Beaton, T. Tiedje, O. Rubel, Appl. Phys. Lett., 96, 131115 (2010)

[14] Localization effects and band gap of GaAsBi alloys, 12. A. R. Mohmad, F. Bastiman, C. J. Hunter, R. D. Richards, S. J. Sweeney, J. S. Ng, J. P. R. David, B. Y. Majlis, Phys. Status Solidi B, 251, 1276-1281 (2014).

[15] Bi-induced p-type conductivity in nominally undoped Ga(AsBi), G. Pettinari, A. Patanè, A. Polimeni, M. Capizzi, X. Lu, T. Tiedje, Appl. Phys. Lett., 100, 092109 (2012)

[16] Growth and properties of the dilute bismide semiconductor $GaAs_{1-x}Bi_x$ a complementary alloy to the dilute nitrides, T. Tiedje, E. C. Young, A. Mascarenhas, Int. J. Nanotechnol., 5, 963-983 (2008)

[17] The anomalous bandgap bowing in GaAsN, U. Tisch, E. Finkman, J. Salzman, Appl. Phys. Lett., 81, 463-465 (2002)

[18] Composition dependence of photoluminescence of $GaAs_{1-x}Bi_x$ alloys, X. Lu, D. A. Beaton, R. B. Lewis, T. Tiedje, Y. Zhang, Appl. Phys. Lett., 95, 041903 (2009)

[19] Bandgap and lattice-constant of GaInAsP as a function of alloy composition, R. Moon, G. Antypas, L. James, J. Electron. Mater., 3,635-644 (1974)

[20] Optical gain of strained GaAsSb/GaAs quantum-well lasers: a self-consistent approach. G. Liu, S. Chuang, S. Park, J. Appl. Phys., 88, 5554-5561 (2000)

[21] MBE growth of GaAsBi: effect of growth conditions on Bi incorporation, R. B. Lewis, M. Masnadi-Shirazi, V. Bahrami-Yekta, T. Tiedje, 3rd International workshop on bismuth-containing semiconductors (2012)

[22] Epitaxial growth dynamics in gallium arsenide, Anders Ballestad, PhD thesis, University of British Columbia (2005)

[23] Closed cycle chiller as a low cost alternative to liquid nitrogen in molecular beam epitaxy, R. B. Lewis, J. A. Mackenzie, T. Tiedje, D. A. Beaton, M. Masnadi-Shirazi, V. Bahrami-Yekta, K. P. Watkins, P. M. Mooney, J. Vac. Sci. Technol. B, 31, 03C116 (2013)

[24] Experimental determination of the incorporation factor of As_4 during molecular beam epitaxy of GaAs, V. V. Preobrazhenskii, M. A. Putyato, O. P. Pchelyakov, B. R. Semyagin, J. Cryst. Growth, 201/202, 170-173 (1999)

[25] Semiconductor substrate temperature measurement by diffuse reflectance spectroscopy in molecular beam epitaxy, S. R. Johnson, C. Lavoie, T. Tiedje, J. A. Mackenzie, J. Vac. Sci. Technol. B, 11, 1007-1010 (1993)

[26] Applied RHEED: Reflection high energy electron diffraction during crystal growth, W. Braun, Springer (1999)

[27] In Situ Real-Time Characterization of Thin Films, O. Auciello, A. R. Krauss, John Wiley (2001)

[28] Surface evolution during gallium arsenide homoepitaxy with molecular beam epitaxy, M. B. Whitwick, PhD thesis, University of British Columbia (2009)

[29] X-ray diffraction of multilayers and superlattices, W. J. Bartels, J. Hornstra, D. J. W. Lobeek, Acta Cryst., 42, 539-545 (1986)

[30] Bandgap and optical absorption edge of $GaAs_{1-x}Bi_x$ alloys with $0< x< 17.8\%$, M. Masnadi-Shirazi, R. B. Lewis, V. Bahrami-Yekta, T. Tiedje, M. Chicoine, P. Servati, J. Appl. Phys., 116, 223506 (2014)

[31] https://www.thorlabs.com

[32] Electronic states and transport in GaNAs and GaAsBi, D. A. Beaton, PhD thesis, University of British Columbia (2011)

[33] A method of measuring the resistivity and Hall coefficient on lamellae of arbitrary shape, L. T. Van der Pauw, Philips Res. Rep., 13, 220-224 (1958)

[34] Semiconductors and Semimetals, D. L. Rode, R. K. Willardson, A. C. Beer, , Academic Press, Vol. 10 (1975)

[35] Defect energy levels in GaAsBi and GaAs grown at low temperatures, P. M. Mooney, K. P. Watkins, Z. Jiang, A. F. Basile, R. B. Lewis, V. Bahrami-Yekta, M. Masnadi-Shirazi, D. A. Beaton, T. Tiedje, J. Appl. Phys., 113, 133708 (2013)

[36] Growth of high Bi concentration $GaAs_{1-x}Bi_x$ by molecular beam epitaxy, R. B. Lewis, M. Masnadi-Shirazi, T. Tiedje, Appl. Phys. Lett., 101, 082112 (2012)

[37] Kinetically limited growth of GaAsBi by molecular-beam epitaxy, A. J. Ptak, R. France, D. A. Beaton, K. Alberi, J. Simon, A. Mascarenhas, C. S. Jiang, J. Cryst. Growth, 338, 107-110 (2012)

[38] Wavelength selection in macular photocoagulation. Tissue optics, thermal effects, and laser systems, M. A. Mainster, Ophthalmology, 93, 952-958 (1986)

[39] Stimulated Emission Depletion (STED) Microscopy: from Theory to Practice, J. N. Farahani, M. J. Schibler, L. A. Bentolila, Microscopy: Science, Technology, Applications and Education, 1539-1547 (2010)

[40] Optically pumped edge-emitting GaAs-based laser with direct orange emission, L. Toikkanen, A. Härkönen, J. Lyytikäinen, T. Leinonen, A. Laakso, A. Tukiainen, J. Viheriälä, M. Bister, M. Guina, IEEE Photon. Technol. Lett., 26, 384-386 (2014)

[41] All-solid-state continuous-wave frequency-doubled Nd:YAG/LBO laser with 1.2 W output power at 561 nm, Y. Yao, Q. Zheng, D. P. Qu, K. Zhou, Y. Liu, L. Zhao, Laser Phys. Lett., 7, 112-115 (2010)

[42] 7.4W yellow GaInNAs-based semiconductor disk laser, T. Leinonen, V. M. Korpijärvi, A. Härkönen, M. Guina, Electron. Lett., 47, 1139-1140 (2011)

[43] High-power optically pumped semiconductor laser at 1040 nm, T. L. Wang, Y. Kaneda, J. M. Yarborough, J. Hader, J. V. Moloney, A. Chernikov, S. Chatterjee, S. W. Koch, B. Kunert, W. Stolz, Photon. Technol. Lett., 22, 661-663 (2010)

[44] High-power CW red VECSEL with linearly polarized TEM00 output beam, J. Hastie, S. Calvez, M. Dawson, T. Leinonen, A. Laakso, J. Lyytikäinen, M. Pessa, Opt. Express, 13, 77-81 (2005)

[45] 1180 nm VECSEL with output power beyond 20 W, S. Ranta, M. Tavast, T. Leinonen, N. Van Lieu, G. Fetzer, M. Guina, Electron. Lett., 49, 59-60 (2013)

[46] Optically pumped GaSb-based VECSEL emitting 0.6 W at 2.3 µm, N. Schulz, M. Rattunde, C. Manz, K. Koehler, C. Wild, J. Wagner, S. S. Beyertt, U. Brauch, T. Kuebler, A. Giesen, Photon. Technol. Lett., 18, 1070-1072 (2006)

[47] Optically pumped 5 microm IV-VI VECSEL with Al-heat spreader, M. Rahim, F. Felder, M. Fill, H. Zogg, Opt. Lett., 33, 3010-3012 (2008)

[48] High-efficiency 20 W yellow VECSEL, E. Kantola, T. Leinonen, S. Ranta, M. Tavast, M. Guina, Optics Express, 22, 6372-6380 (2014)

[49] Modeling quantum well lasers, P. F. Liao, P. Kelley, Elsevier Science (2012)

[50] GaNAs and GaAsBi: Structural and electronic properties of two resonant state semiconductor alloys, E. C. Young, PhD thesis, University of British Columbia (2006)

[51] Characterization of semiconductor heterostructures and nanostructures, C. Lamberti, G. Agostini, Elsevier Science, p. 76-80 (2013)

[52] Molecular beam epitaxy growth of $GaAs_{1-x}Bi_x$, S. Tixier, M. Adamcyk, T. Tiedje, S. Francoeur, A. Mascarenhas, P. Wei, F. Schiettekatte, Appl. Phys. Lett., 82, 2245-2247 (2003)

[53] MBE growth optimization for $GaAs_{1-x}Bi_x$ and dependence of photoluminescence on growth temperature, V. Bahrami-Yekta, T. Tiedje, M. Masnadi-Shirazi, Semicond. Sci. Technol., 30, 094007 (2015)

[54] The effect of Bi composition to the optical quality of $GaAs_{1-x}Bi_x$, A. R. Mohmad, F. Bastiman, C. J. Hunter, J. S. Ng, S. J. Sweeney , J. P. David, Appl. Phys. Lett., 99, 042107 (2011)

[55] Effects of spatial confinement and layer disorder in photoluminescence of $GaAs_{1-x}Bi_x$/GaAs heterostructures, Y. Mazur, V. Dorogan, M. Benamara, M. Ware, M. Schmidbauer, G. Tarasov, S. Johnson, X. Lu, S. Q.Yu, T. Tiedje , G. Salamo, J. Phys. D: Appl. Phys., 46, 065306 (2013)

[56] Optical Absorption of Gallium Arsenide between 0.6 and 2.75 eV, M. D. Sturge, Phys. Rev., 127, 768-773 (1962)

[57] The effect of Bi composition to the optical quality of $GaAs_{1-x}Bi_x$, A. R. Mohmad, F. Bastiman, C. Hunter, J. Ng, S. Sweeney , J. David, Appl. Phys. Lett., 99, 042107 (2011)

[58] Effect of Bi alloying on the hole transport in the dilute bismide alloy $GaAs_{1-x}Bi_x$, R. N. Kini, A. J. Ptak, B. Fluegel, R. France, R. C. Reedy, A. Mascarenhas, Phys. Rev. B, 83, 075307 (2011)

[59] Compositional evolution of Bi-induced acceptor states in $GaAs_{1-x}Bi_x$ alloy, G. Pettinari, H. Engelkamp, P. C. M. Christianen, J. C. Maan, A. Polimeni, M. Capizzi, X. Lu, T. Tiedje, Phys. Rev. B, 83, 201201 (2011)

[60] Spatial correlation between Bi atoms in dilute $GaAs_{1-x}Bi_x$: From random distribution to Bi pairing and clustering, G. Ciatto, E. C. Young, F. Glas, J. Chen, R. A. Mori, T. Tiedje, Phys. Rev. B, 78, 035325 (2008)

[61] Atomic ordering and phase separation in MBE $GaAs_{1-x}Bi_x$, A. Norman, R. France, A. Ptak, Vac. Sci. Technol. B, 29, 03C121 (2011)

[62] Observation of atomic ordering of triple-period-A and -B type in GaAsBi, M. Wu, E. Luna, J. Puustinen, M. Guina, A. Trampert, Appl. Phys. Lett., 105, 041602 (2014)

[63] Optical absorption edge of semi-insulating GaAs and InP at high temperatures, M. Beaudoin, A. J. G. DeVries, S. R. Johnson1, H. Laman, T. Tiedje, Appl. Phys. Lett., 70, 3540 (1997)

[64] Temperature dependence of $GaAs_{1-x}Bi_x$ bandgap studied by photoreflectance spectroscopy, J. Yoshida, T. Kita, O. Wada, K. Oe, J. Appl. Phys., 42, 371 (2003)

[65] Low temperature dependence of oscillation wavelength in $GaAs_{1-x}Bi_x$ laser by photo-pumping, Y. Tominaga, K. Oe, M. Yoshimoto, Appl. Phys. Express, 3, 062201 (2010)

[66] Bandgap of $GaAs_{1-x}Bi_x$ $0<x<3.6\%$, S. Francoeur, M. J. Seong, A. Mascarenhas, S. Tixier, M. Adamcyk, T. Tiedje, Appl. Phys. Lett., 82, 3874 (2003)

[67] Photoluminescence investigation of high quality $GaAs_{1-x}Bi_x$ on GaAs, A. Mohmad, F. Bastiman , S. Ng, S. Sweeney , J. P. David, Appl. Phys. Lett., 98, 122107 (2011)

[68] Disorder and the Urbach edge in dilute bismide GaAsBi, C. Gogineni1, N. A. Riordan1, S. R. Johnson, X. Lu, T. Tiedje, Appl. Phys. Lett., 103, 041110 (2013)

[69] Concepts in photoconductivity and allied problems, A. Rose, Huntingdon, NY: Krieger Publishing Co. (1978)

[70] Deep level transient spectroscopy measurements of GaAsBi/GaAs, Z. Jiang, MSc thesis, Simon Fraser University (2007)

[71] Deep-level transient spectroscopy: A new method to characterize traps in semiconductors, D. V. Lang, J. Appl. Phys., 45, 3023 (1974)

[72] The electrical characterization of semiconductors: majority carriers and electron states, P. Blood, J. W. Orton, Academic Press (1992)

[73] Hole traps in bulk and epitaxial GaAs crystals, A. Mitonneau, G. M. Martin, A. Mircea, Electron. Lett., 13, 666-668 (1977)

[74] Arsenic antisite-related defects in low-temperature MBE grown GaAs, K. Krambrockt, M. Lindet, J. Spaethi, D. C. Look, D. Bliss, W. Walukiewiczs, Semicond. Sci. Technol., 7, 1037-1041 (1992)

[75] The energy level of the EL2 defect in GaAs, J. C. Bourgoin, T. Neffati, Solid-State Electron., 43, 153-158 (1999)

[76] Native hole trap in bulk GaAs and its association with the double charge state of the arsenic antisite defect, J. Lagowski, D.G. Lin, T.-P. Chen, M. Skowronski, H.C. Gatos, Appl. Phys. Lett., 47, 929 (1985)

[77] Deep-hole traps in p-type $GaAs_{1-x}Bi_x$ grown by molecular beam epitaxy, T. Fuyuki, S. Kashiyama, Y. Tominaga, K. Oe, M. Yoshimoto, Jpn. J. Appl. Phys. 50, 080203 (2011)

[78] Surface dimerization induced CuPt-B versus CuPt-A ordering of GaInP alloys, S. B. Zhang, S. Froyen, A. Zunger, Appl. Phys. Lett., 67, 3141 (1995)

[79] Polarisation selectivity in ordered GalnP vertical cavity surface-emitting lasers, A. T. Meney, E. P. O’Reilly, K. J. Ebeling, Electron. Lett., 6, 461-462 (1995)

[80] Polarisation control for surface emitting lasers, M. Shimuzi, T. Mukaihara, F. Koyama, K. Iga, Electron. Lett., 27, 1067-1069 (1991)

[81] Engineered polarization control of GaAs/AlGaAs surface-emitting lasers by anisotropic stress from elliptical etched substrate hole, T. Mukaihara, F. Koyama, K. Iga, IEEE Photonics Technol., 5, 133-135 (1993)

[82] Effects of strain and GalnP superlattice ordering on laser polarization, G. Forstmannt, F. Bartht, H. Schweizert, M. Mosert, C. Gengt, F. Scholzt, E. O’Reilly, Semicond. Sci. Technol., 9, 1268-1271 (1994)

[83] Atomic ordering and phase separation in MBE $GaAs_{1-x}Bi_x$, A. Norman, R. France, A. J. Ptak, J. Vac. Sci. Technol. B, 29, 03C121 (2011)

[84] Structural characteristics of dilute nitride & bismide III/V semiconductors, K. Volz, International Workshop on Bismuth-Containing Semiconductors (2010)

[85] Compton scattering factors for spherically symmetric free atoms, D. T. Cromer, J. B. Mann, J. Chem. Phys., 47, 1892-1893 (1967)

[86] X-ray diffraction of multilayers and superlattices, W. J. Bartels, J. Hornstra, D. J. W. Lobeek, Acta Cryst. A, 42, 539-545 (1986)

[87] Bismuth incorporation and the role of ordering in GaAsBi/GaAs structures, D. F. Reyes, F. Bastiman, C. Hunter, D. Sales, A. Sanchez, J. David, D. González, Nanoscale Res. Lett., 9, 23 (2014)

[88] Elements of x-ray diffraction, B. D. Cullity, S. R. Stock, Prentice-Hall (2001)

[89] Band-gap narrowing in ordered $Ga_{0.47}1n_{0.53}As$, D. J. Arent, M. Bode, K. A. Bertness, Sarah FL Kurtz, J. M. Olson, Appl. Phys. Lett., 62, 1806-1808 (1993)

[90] TEM, TED and HREM studies of atomic ordering and associated domains in MOCVD $In_xGa_{1-x}As$ layers: Dependence on growth temperature and growth rate, T. Y. Seong, A. G. Norman, J. L. Hutchison, G. R. Booker, A. G. Cullis, S. J. Bass, L. L. Taylor, Microsc. Semicond. Mater. Conf. 117, 463-468 (1991)

[91] Interplay of strain and superlattice ordering on GaInP quantum-well valence-subband structure, E. P. O'Reilly, A. T. Meney, Phys. Rev. B, 51, 7566-7570 (1995)

[92] http://www.westgrid.ca

[93] http://departments.icmab.es/leem/siesta/

[94] http://www.abinit.org/

[95] The electronic properties of graphene, A. H. Neto, F. Guinea, N. R. Peres, K. S. Novoselov, A. K. Geim, Rev. Mod. Phys., 81, 109-162 (2009)